Experimentele statistische kanaalmodellering voor geavanceerde draadloze communicatiesystemen in indooromgevingen

Experimental Statistical Channel Modelling for Advanced Wireless Communication Systems in Indoor Environments

Emmeric Tanghe

Promotoren: prof. dr. ir. L. Martens, prof. dr. ir. W. Joseph
Proefschrift ingediend tot het behalen van de graad van
Doctor in de Ingenieurswetenschappen: Elektrotechniek

Vakgroep Informatietechnologie
Voorzitter: prof. dr. ir. D. De Zutter
Faculteit Ingenieurswetenschappen en Architectuur
Academiejaar 2010 - 2011

UNIVERSITEIT GENT

ISBN 978-90-8578-428-9
NUR 959
Wettelijk depot: D/2011/10.500/32

Voorwoord

In dit voorwoord wens ik enkele mensen te bedanken die rechtstreeks of onrechtstreeks hebben bijgedragen tot de totstandkoming van dit doctoraat. Die bijdrage ligt zowel in hun gewaardeerde medewerking in goede tijden als hun begrip en ondersteuning in minder goede tijden. Vooreerst wil ik mijn beide promotoren Luc Martens en Wout Joseph bedanken voor de kans om dit doctoraatsonderwerp aan te vatten. Ook dank ik hen voor het mogen gebruik maken van hun jarenlange ervaring in de vele wetenschappelijke discussies die onontbeerlijk zijn in elke doctoraatsonderzoek. Ik vermeld ook nog de onvermijdelijke hopen papier die ik bij elkaar schreef en die zij steeds met aandacht doornamen en corrigeerden. Daarnaast bedank ik ook de leden van de examencommissie voor hun suggesties ter verbetering van dit doctoraatsboek.

Verder wil ik ook alle collega's en ex-collega's niet vergeten voor het creëren van de aangename werksfeer in de Wireless & Cable onderzoeksgroep. Over de jaren heen heb ik collega's zien komen en gaan en ik bedank hen allen voor de interessante discussies en de mooie herinneringen: perm({Francis, Günter, Arno, Toon, Kris, Simon, Aliou, Adrián, David, Margot, Divya, Frederic, Leen, Jeffrey, Tom, Laurens, Michiel, Elisabeth, István, Luc}), waar perm() een willekeurige permutatie is van de verzameling elementen in zijn argument die zodoende elke hiërarchie in die elementen teniet doet. Uit deze lijst wil ik toch Leen Verloock speciaal vernoemen: voor vier van de vijf onderzoekshoofdstukken hielp zij met de software- en hardwarekant van de meetopstelling en verleende ze bovendien haar assistentie tijdens enkele van de meetcampagnes. Voor het maken van de metalen en PVC constructies voor de meetopstellingen dank ik Luc Haentjens van de vakgroep Informatietechnologie. Voor de hulp bij de metingen in hoofdstuk 2 en 3 vermeld ik de vroegere projectmedewerkers van het departement PIH van de Hogeschool West-Vlaanderen. Ik waardeer ook het vurig enthousiasme waarmee ex-collega Jeffrey De Bruyne zijn assistentie aanbood voor de metingen in hoofdstuk 4. Voor het aanreiken van de meetdata voor hoofdstuk 5 en voor de diepgaande discussies van de meetresultaten moet ik zeker de onderzoeksgroep TELICE van de Université Lille 1 vermelden: in het bijzonder gaat mijn dank uit naar Martine Liénard, Davy Gaillot en Paul Stefanut.

Algemeen wens ik de vakgroep Informatietechnologie, onder leiding van Paul Lagasse aan het begin van mijn doctoraat en nu onder leiding van Daniël De Zutter, te bedanken voor het aanbieden van de nodige voorzieningen voor het succesvol uitvoeren van een doctoraat. Ik denk hierbij niet alleen aan de technische voorzieningen, maar ook aan de mensen die instaan voor het vlot verlopen van alle

administratieve en financiële aangelegenheden: speciaal vermeld ik Isabelle, de secretaresse van de Wireless & Cable groep.

Ik wil ook nog enkele mensen uit mijn niet-werkgerelateerde omgeving bedanken voor hun steun en/of vriendschap. Als eerste vermeld ik uiteraard mijn ouders die mij de kans gaven om mijn studies aan te vatten en te voltooien. Daarnaast mag ik natuurlijk mijn zus niet vergeten voor mijn zus te zijn. Uiteraard vergeet ik ook mijn goede vrienden en gelijkgestemde zielen Björn, Frederik, Kenny en Sem niet. Omdat een dankwoord altijd het risico inhoudt van mensen of andere levensvormen te vergeten, bedank ik in deze laatste zin nog eens iedereen die onbewust door de mazen van mijn geheugen is geglipt. Tot slot ook nog een webcomic over conditionele probabiliteiten ter verzachting van de statistiek die de lezer in de komende hoofdstukken zal te verwerken krijgen:

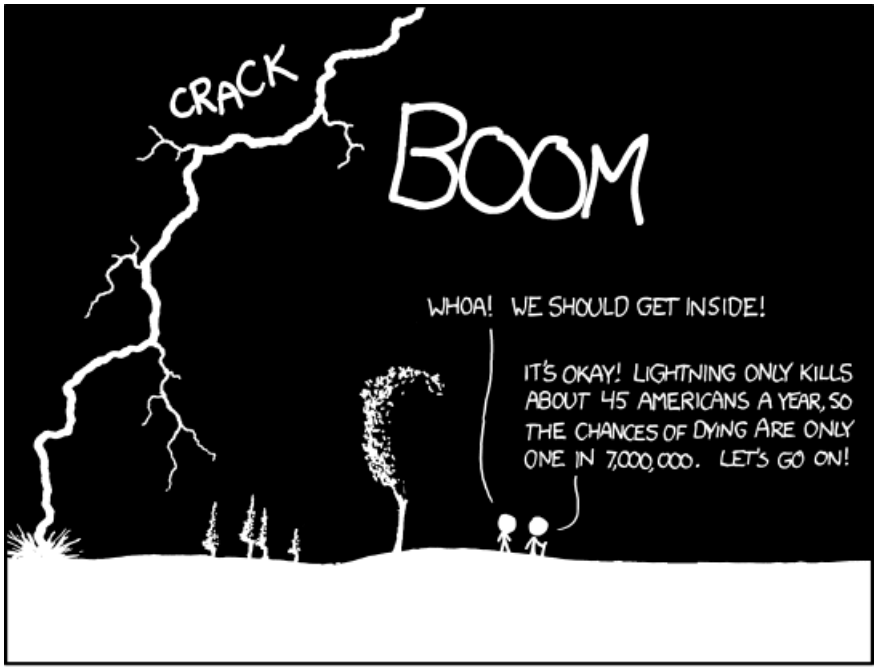

"Hey wait – I'm not American! So my risk is basically zero!" (courtesy of xkcd.com)

Gent, mei 2011
Emmeric Tanghe

Table of Contents

List of Figures

List of Tables

List of Symbols and Acronyms

Symbols

d transmitter-receiver distance [m]

d_0 reference transmitter-receiver distance [m]

D data rate [Mbps]

f frequency [MHz]

G_R gain of the receiving antenna [dBi]

G_T gain of the transmitting antenna [dBi]

h complex channel transfer function [-]

$\mathcal{H}$ complex channel transfer function [-]

$\boldsymbol{H}$ complex channel transfer function [-]

L_R loss of the receiving antenna feeder cable [dB]

L_T loss of the transmitting antenna feeder cable [dB]

K Ricean K-factor [dB]

m Nakagami-m shape parameter

M_X shadow fading margin [dB]

M_Y temporal fading margin [dB]

n path loss exponent [-]

p_{exp} exponential probability density function [-]

p_{logn} lognormal probability density function [-]

p_{nak} Nakagami-m probability density function [-]

p_{norm} normal probability density function [-]

p_{poiss} Poisson probability density function [-]

p_{rayl} Rayleigh probability density function [-]

p_{uni} uniform probability density function [-]

p_{vm} von Mises probability density function [-]

PL path loss [dB]

PL_{max} maximal path loss [dB]

P_R received power [dBm]

P_{RS} receiver sensitivity [dBm]

P_T transmitted power [dBm]

R_{emp} empirical wireless range [m]

R_{theor} theoretical wireless range [m]

X shadow fading random variable [dB]

Y temporal fading random variable [dB]

Z standard normally distributed random variable

γ ray power decay constant [ns]

Γ cluster power decay constant [ns]

κ von Mises concentration parameter

λ (chapter 4) ray arrival rate [GHz]

λ (chapter 5) mean waiting time between paths [ns]

Λ cluster arrival rate [GHz]

μ (log)normal mean parameter

σ (log)normal standard deviation parameter or Rayleigh parameter

τ time delay [ns]

T time delay [ns]

τ_{rms} root mean square delay spread

ϕ^A azimuth of arrival [rad]

Φ^A azimuth of arrival [rad]

ϕ^D azimuth of departure [rad]

Φ^D azimuth of departure [rad]

Ω Nakagami-m scale parameter

0-9

2G Second Generation

3G Third Generation

4G Fourth Generation

5D Five-Dimensional

A

AD Anderson-Darling

ANOVA ANalysis Of VAriance

AOA Azimuth Of Arrival

AOD Azimuth Of Departure

AP Access Point

APDP Averaged Power Delay Profile

AWGN Additive White Gaussian Noise

B

BER Bit Error Rate

C

CDF Cumulative Distribution Function

CLT Central Limit Theorem

CI Confidence Interval

CIR Channel Impulse Response

D

DMC Diffuse Multipath Components

DVB-T/H Digital Video Broadcasting - Terrestrial/Handheld

E

EDGE Enhanced Data rates for GSM Evolution

ESPRIT Estimation of Signal Parameters via Rotational Invariance Techniques

F

FABLE FActorization into a BLock-diagonal Expression

G

GOF Goodness Of Fit

GPRS General Packet Radio Service

GPS Global Positioning System

GSM Global System for Mobile communication

H

HSPA High Speed Packet Access

HZ Henze-Zirkler

I

IEEE Institute of Electrical and Electronics Engineers

IDFT Inverse Discrete Fourier Transform

ISI InterSymbol Interference

ISM Industrial, Scientific, and Medical

K

KS Kolmogorov-Smirnov

L

LOS Line Of Sight

LRT Likelihood Ratio Test

LS Least Squares

LSF Large-Scale Fading

LTE Advanced Long Term Evolution Advanced

M

MB Moment Based

MCD Multipath Component Distance

MIMO Multiple Input Multiple Output

MLE Maximum Likelihood Estimator

MPC MultiPath Component

N

NLOS Non Line Of Sight

O

OBS OBstructed line of Sight

OFDM Orthogonal Frequency-Division Multiplexing

P

PEC Perfectly Electrically Conducting

PER Packet Error Rate

PDF Probability Density Function

PDP Power Delay Profile

PL Path Loss

Q

QQ Quantile-Quantile

R

RMS Root Mean Square

RSS Received Signal Strength

Rx receiving antenna

S

SSF Small-Scale Fading

SV Saleh-Valenzuela

SW Shapiro-Wilk

T

TF Temporal Fading

Tx transmitting antenna

U

UCA Uniform Circular Array

ULA Uniform Linear Array

UMTS Universal Mobile Telecommunications System

URA Uniform Rectangular Array

V

VPL Vehicle Penetration Loss

W

WICA WIreless and CAble research group

WiMAX Worldwide Interoperability for Microwave Access

WLAN Wireless Local Area Network

WMAN Wireless Metropolitan Area Network

WNIC Wireless Network Interface Card

WSN Wireless Sensor Network

WWAN Wireless Wide Area Network

Nederlandstalige samenvatting

Alhoewel het niet de gewoonte is om de structuur van een samenvatting te geven, is de structuur van deze samenvatting als volgt. In de eerste drie paragrafen wordt de titel van deze thesis opgebroken in drie stukken. De betekenis van elk stuk met betrekking tot de inhoud van de thesis wordt verder uit de doeken gedaan. Tot slot worden in de vierde en laatste paragraaf meer details gegeven omtrent welke soorten kanaalmodellering er werden uitgevoerd, zonder al te technisch te zijn.

Experimentele statistische kanaalmodellering...

De bijdrage van dit werk tot propagatiemodellering voor draadloze communicatiesystemen situeert zich in het gebied van **fysische kanaalmodellen**. Fysische kanaalmodellen beschrijven draadloze propagatie aan de hand van parameters die de werkelijke (fysische) elektromagnetische golven karakteriseren. In fysische kanaalmodellering wordt het draadloos kanaal gezien als een verzameling van (vlakke) golven. Deze golven worden gekarakteriseerd door een aantal parameters, waaronder: de hoeken onder dewelke de golven vertrekken aan de zendantenne en aankomen bij de ontvangstantenne, de tijd waarin ze zich van zend- naar ontvangstzijde voortplanten, de grootte en de fase van hun elektrisch en magnetisch veld aan ontvangstzijde, enz. De opgesomde parameters zijn van toepassing op *individuele* golven, maar fysische modellen omvatten evengoed parameters die een zekere deelverzameling van golven *als geheel* beschrijven. De meest bekende parameter van dit laatste type is het padverlies. Het padverlies drukt uit wat het totaal verlies aan vermogen is dat alle golven samen ondergaan tijdens de voortplanting van zend- naar ontvangstantenne.

De fysische kanaalmodellen in deze thesis zijn bijna uitsluitend **empirische modellen**. Dit betekent dat de parameters van golven experimenteel bepaald worden door het uitvoeren en verwerken van metingen in het draadloos kanaal. Dit proces wordt doorgaans ook *"channel sounding"* genoemd.

Draadloze communicatie in een reële omgeving geeft aanleiding tot een groot aantal propagerende golven. Dit volgt uit de aanwezigheid van een groot aantal mogelijke verstrooiers van elektromagnetische energie in een reële omgeving, bv. bureaus in een kantooromgeving, gebouwen buiten, enz. De exacte positie van deze verstrooiers is over het algemeen willekeurig en moeilijk in rekening te brengen in de kanaalmodellering als er geen gedetailleerde grondplannen van de omgeving beschikbaar zijn. Op hun beurt betekenen willekeurige posities van verstrooiers ook willekeurige waarden van de parameters van propagerende golven.

Ook rekening houdend met het verwachte grote aantal propagerende golven, verantwoordt dit het **statistisch** modelleren van golf parameters in deze thesis.

...voor geavanceerde draadloze communicatiesystemen...

De kanaalmodellering in deze thesis is uitgevoerd voor draadloze communicatiesystemen die alomtegenwoordig zijn in het dagelijkse leven. Het grootste deel van deze thesis behandelt kanaalmodellering voor **Wireless Local Area Networks (WLANs)** in kantooromgevingen en industriële omgevingen. WLANs voorzien een klein gebied van draadloze dekking. Dit gebied is meestal binnenshuis, bv. een productieruimte in een fabriek of een verdieping van een kantoorgebouw. Het belangrijkste bewijs van de populariteit van WLAN technologie is de hoge adoptiegraad van IEEE 802.11 systemen door bedrijven en particulieren. Vandaag zijn de meest gebruikte WLAN standaarden de IEEE 802.11a/b/g varianten. Men verwacht echter dat de recent goedgekeurde IEEE 802.11n standaard aan terrein zal winnen. IEEE 802.11n biedt verscheidene verbeteringen op IEEE 802.11a/b/g aan die de maximale bitsnelheid te verhogen van 54 naar 600 Mb/s. De belangrijkste van deze verbeteringen is de toevoeging van Multiple Input Multiple Output (MIMO) technologie.

Daarnaast wordt in deze thesis ook aan kanaalmodellering gedaan voor **cellulaire netwerken**, **omroepnetwerken** en WLANs in een voertuig. Cellulaire netwerken en omroepnetwerken voorzien (mobiele) datacommunicatie in een groot geografisch gebied, bv. een volledige stad of een volledig land. In deze thesis wordt draadloze propagatie van buiten naar binnen een voertuig onderzocht voor de cellulaire Global System for Mobile communication (GSM) technologie, de Digital Video Broadcasting - Terrestrial/Handheld (DVB-T/H) omroeptechnologie, en de IEEE 802.11b/g WLAN technologieën.

...in indooromgevingen.

Deze thesis behandelt kanaalmodellering in indooromgevingen. Meer specifiek worden industriële omgevingen, kantoor- en voertuigomgevingen beschouwd. Het grootste deel van dit werk gaat over kanaalmodellering in **industriële omgevingen**. De industrie is meer en meer geïnteresseerd om draadloze communicatie te integreren in hun productielijnen, wat het praktisch nut van kanaalmodellering in industriële omgevingen aantoont. Om deze toenemende interesse te illustreren, merken we op dat productielijnen in hedendaagse fabrieken vaak veranderd, verbeterd of verplaatst worden om zo beter in te kunnen spelen op de noden van de markt en om competitief te blijven. Dit wil zeggen dat werkplaatsen in de tijd veel veranderingen ondergaan. Hierdoor zou bedrade communicatie tussen twee machines resulteren in het vaak heraanleggen van de communicatiekabels, wat duur is en tijd in beslag neemt. Draadloze communicatie zou daarentegen een meer flexibele oplossing bieden. Integratie van draadloze communicatie in industriële

omgevingen stelt evenwel enkele nieuwe uitdagingen. Het radiokanaal in een fabrieksomgeving gedraagt zich heel anders dan het radiokanaal in bijvoorbeeld een kantooromgeving, ten gevolge van de meer open lay-out van industriële sites en de aanwezigheid van machines en hoogreflectieve materialen zoals metaal. In deze thesis zijn metingen uitgevoerd voor een bepaald soort industriële communicatie, namelijk draadloze communicatie tussen een toegangspunt opgesteld op ongeveer 6 m hoogte en terminals op lager opgesteld op ongeveer 2 m hoogte.

Een volgend deel van deze thesis behandelt kanaalmodellering in een **kantooromgeving**. WLAN technologie is sinds enkele jaren onmisbaar geworden in de moderne kantooromgeving. De populariteit van WLANs in kantooromgevingen gaat hand in hand met het toenemend gebruik van laptops, die over de jaren heen krachtig en compact genoeg geworden zijn om onderweg comfortabel taken te kunnen uitvoeren. De meeste moderne bedrijven laten bezoekers dan ook toe om te connecteren op hun WLAN en verlenen hen zo toegang tot het internet tijdens werkvergaderingen. In deze thesis wordt een empirisch kanaalmodel ontwikkeld voor de IEEE 802.11n WLAN standaard in een kantooromgeving.

Het is vaak wenselijk om een mobiel communicatietoestel ook te kunnen gebruiken in een **voertuig**. Om bijvoorbeeld real-time updates van de verkeerssituatie op de weg te krijgen is een werkende dataverbinding in een voertuig nodig. De signaalsterkte binnen in een voertuig kan echter gevoelig lager liggen dan de signaalsterkte buiten het voertuig. Om met een bepaalde betrouwbaarheid draadloze dekking te voorzien in een voertuig, moet het verlies aan vermogen wanneer het draadloos signaal het voertuig binnengaat, gekarakteriseerd worden. Dit vermogensverlies wordt ook het penetratieverlies van het voertuig genoemd en de statistische eigenschappen ervan worden voor een aantal propagatiescenario's bepaald. Penetratieverliezen van voertuigen zijn van belang voor draadloze dienstenleveranciers om marges te berekenen voor de begroting van de hoeveelheid beschikbaar vermogen voor de draadloze verbinding.

Details van de kanaalmodellering

De eerste drie onderzoekshoofdstukken van dit doctoraatswerk behandelen propagatiemodellering in industriële omgevingen. Hoofdstuk 2 stelt een karakterisering voor van industriële "large-scale" en temporele fading op basis van metingen uitgevoerd in twee houtverwerkende en twee metaalverwerkende bedrijven. Large-scale fading is gedefinieerd als de variabiliteit van het ontvangen vermogen als functie van de afstand, gemiddeld gezien over afstandsintervallen van enkele golflengtes. Anderzijds is temporele fading gedefinieerd als de variabiliteit van het ontvangen vermogen in de tijd op een vaste positie in de omgeving. De karakterisering van large-scale en temporele fading gebeurt op basis van smalbandmetingen bij drie frequenties van 900, 2400 en 5200 MHz. Deze frequenties liggen in of dicht bij frequentiebanden die gebruikt worden door draadloze standaarden als IEEE 802.11 en ZigBee. Men verwacht dat dit ook de communicatiestandaarden zijn ook hun ingang zullen vinden in industriële communicatietoepassingen.

De meetdata wordt gecategoriseerd in een aantal industriële topografieën die als doel hebben de industriële omgeving verder onder te verdelen in sub-omgevingen voor dewelke significant verschillende large-scale of temporele fading wordt verwacht. In dit hoofdstuk wordt vastgesteld dat large-scale fading goed beschreven wordt door een enkelvoudig lineair padverlies model en dat temporele fading goed beantwoordt aan Rice verdeelde statistiek.

In hoofdstuk 3 worden de industriële large-scale fading en temporele fading modellen getoetst aan een aantal metingen op de fysieke laag van een 802.11b/g draadloos systeem. Meer bepaald wordt onderzocht of het draadloos bereik volgens de industriële fading modellen in overeenstemming is met het draadloos bereik volgens de metingen op de fysieke laag. De vergelijking tussen deze twee bereiken wordt uitgevoerd voor drie praktisch interessante 802.11b/g bitsnelheden van 2, 11 en 18 Mbps.

In hoofdstuk 4 worden metingen van "power delay profiles" in industriële omgevingen voorgesteld. Power delay profiles zijn grafieken die het vermogen van de elektromagnetische golven uitzetten tegen de voortplantingstijd van deze golven tussen zender en ontvanger. Power delay profiles laten bijgevolg toe een analyse te maken van de tijdsdispersie van het ontvangen vermogen. De power delay profiles in deze thesis worden bepaald door metingen in het frequentiedomein van 800 MHz tot 4 GHz, en door gebruik te maken van virtuele rijen van antennes aan zend- en ontvangstzijde. De power delay profiles, uitgemiddeld over een gebied waar de large-scale fading constant is, vertonen duidelijk clustering van het ontvangen vermogen als functie van de voortplantingstijd. Om deze reden werd het bekende, cluster-gebaseerde Saleh-Valenzuela model voor het gemiddelde power delay profile aan de meetdata gefit.

In hoofdstuk 5 worden parameters geassocieerd met discrete propagerende golven (ook propagatiepaden genoemd) geëxtraheerd uit metingen met behulp van het ESPRIT algoritme. De geschatte parameters van de propagatiepaden zijn de aankomsthoek, de vertrekhoek, de voortplantingstijd en het vermogen. De parameters worden gegroepeerd in clusters met het statistisch K-power-means algoritme. De statistische distributies van de parameters binnenin clusters worden bepaald en de correlaties tussen de parameters worden besproken. Vervolgens worden de locatie- en schaalparameters van deze statistische distributies gebruikt om de intra-cluster en inter-cluster eigenschappen van de propagatiepad parameters te karakteriseren. Dit gebeurt door op hun beurt de statistische distributies van de locatie- en schaalparameters te bepalen, en door hun correlaties te analyseren. Bijkomend wordt in hoofdstuk 5 een nieuwe notatie voor de MIMO kanaalmatrix gegeven genaamd FActorization into a BLock-diagonal Expression (FABLE).

In hoofdstuk 6 worden metingen en ray-tracing simulaties besproken van het penetratieverlies van een voertuig (lichte bestelwagen) bij frequenties van 600, 900, 1800 en 2400 MHz. Het gemiddeld gemeten penetratieverlies varieert van 3.2 tot 23.8 dB, naargelang de frequentie, de bestraalde kant van het voertuig en de oriëntatie van de antenne in het voertuig. De penetratieverliezen volgen lognormale distributies met standaardafwijkingen tussen 3.0 and 4.7 dB.

English summary

Although it is not common to provide an outline for a summary, this summary is outlined as follows. In the first three subsections the title of this dissertation is broken down and each part is elaborated on in relation to the contents of this work. The fourth subsection gives more details on which different kinds of channel modelling are done, without going into the technicalities of the models.

Experimental statistical channel modelling...

The contribution of this work to propagation modelling for wireless communication systems is situated in the area of **physical channel models**. Physical models describe wireless propagation in terms of parameters characterizing the actual (physical) propagating waves. In physical channel modelling, the wireless channel is seen as a collection of (plane) waves propagating in the environment. These waves are characterized by a number of parameters, including: the direction in which they depart from the transmitting antenna and at which they arrive at the receiving antenna, the time they travel from transmitting to receiving antenna, the complex magnitude of their received electric and magnetic fields, etc. The parameters listed are ones characterizing *individual* waves, but physical models also include parameters that characterize a certain subset of the waves *as a whole*. The most well-known parameter of the latter type is the path loss, which expresses the combined power loss of all waves in the channel between transmit and receive side.

Regarding physical propagation models, the models in this work are almost exclusively **empirical models**. This means that parameters of propagating waves are determined experimentally by means of probing the wireless channel with appropriate measurement equipment and usually also by performing some post-processing on measurement data. This process is also commonly referred to as *channel sounding*.

Wireless communication is expected to give rise a large number of travelling waves in real environments. This is due to a large number of possible scatterers of electromagnetic energy, e.g., desks in office environments, buildings in outdoor environments, etc. The location of these scatterers is usually random and difficult to take into account in the channel modelling if no detailed maps of the environment exist. Randomly located scatters mean random values for the parameters of propagating waves. This, together with the expected large number of waves, justi-

fies modelling the propagation parameters **statistically** in this work.

...for advanced wireless communication systems...

In this dissertation, propagation modelling is done for wireless communication systems which have achieved maturity and are commonplace in today's society. Foremost, propagation is investigated for **Wireless Local Area Networks (WLANs)** in industrial and office environments. WLANs cover a small area, most commonly indoors, such as a production hall or an office floor. The prime example of the success of WLAN technology is the high adoption of IEEE 802.11 systems among businesses and individuals. Today, the most widely used WLAN technology standards are IEEE 802.11a/b/g. It is however expected that a move towards the recently approved IEEE 802.11n standard will happen. IEEE 802.11n offers various improvements over IEEE 802.11a/b/g to increase the achievable physical bitrate from 54 to 600 Mb/s. The most important among these improvements is the addition of Multiple Input Multiple Output (MIMO) technology.

Some additional propagation characterization is also done for **cellular networks**, **broadcast networks**, and WLANs in a vehicular environment. Cellular and broadcast networks provide (mobile) data communication in a large geographical area, spanning a whole city or country. Outside to inside propagation in a vehicular environment is investigated for the Global System for Mobile communication (GSM) cellular technology, Digital Video Broadcasting - Terrestrial/Handheld (DVB-T/H) broadcast technology, and IEEE 802.11b/g WLANs.

...in indoor environments.

In this work, propagation modelling is done for indoor environments. Specifically, industrial, office, and vehicular environments are considered. The largest part of this work is centered around propagation in **industrial environments**. Industrial manufacturing centers are increasingly interested to incorporate wireless communication in their production processes, which shows the practicality of propagation research in factory environments. To illustrate the motive behind industrial wireless communication, it is noted that production lines in contemporary factories are often changed, improved, or moved to quickly adapt to the market's needs and to stay competitive. This implies highly dynamic changes of the workplace layout over time. As a result, wired communication between two pieces of machinery would require frequent rerouting of cables, which is costly and time consuming. A more flexible solution would be to use wireless communication between machinery. Integration of wireless communication in the industrial environment however poses new challenges. The radio channel in factories will behave much differently with respect to the radio channel of e.g., office buildings, due to the more open building layout, the presence of machinery, and the presence of highly reflective materials such as metal. This stresses the need for developing and improving wave propagation models specifically for factory environments. In this

work, measurements are performed to reflect a specific kind of industrial communication, namely communication between an access point located at a considerable height of about 6 m and wireless terminals situated at smaller heights of about 2 m.

Another part of this work focusses on propagation modelling in an **office environment**. Over the last decade, WLAN technology has become indispensable in a modern day office environment. The popularity of office WLANs goes hand in hand with the increased use of portable notebooks, which over the years have attained a sufficient level of power and compactness to comfortably do office tasks while being mobile. The majority of modern companies allow visitors to connect to a WLAN, so they can access the internet during work meetings. In this work, an empirical propagation model is developed for the IEEE 802.11n WLAN standard in an office environment.

The possibility to use mobile communication devices in a **vehicular environment** is often desirable. For example, to receive real-time updates on highway traffic conditions through mobile data communication networks, a working in-vehicle connection is required. In comparison with outdoor use, the received in-vehicle signal power level can be substantially smaller. For reliable coverage planning with in-vehicle reception, it is necessary to determine how much power loss a signal undergoes when propagating from outside to inside the vehicle. This power loss is also called vehicle penetration loss and its statistics are determined for a couple of propagation scenarios in this doctoral thesis. Vehicle penetration loss statistics are important for service providers to calculate margins for power link budgets.

Channel modelling details

The first three research chapters of this dissertation concern propagation modelling in industrial environments. Chapter 2 presents a characterization of industrial large-scale and temporal fading based on measurements in two wood processing and two metal processing factories. Large-scale fading is defined as the variability of received power with distance, seen on average over distance intervals of a few wavelengths. On the other hand, temporal fading is defined as the variability of received power over time at a fixed location in the propagation environment. Large-scale and temporal fading are determined by performing small-band measurements at three frequencies of 900, 2400, and 5200 MHz. These frequencies lie within or near frequency bands recently targeted for application of industrial wireless communication using wireless standards such as IEEE 802.11 and ZigBee. An effort is made to categorize measurement data into different industrial topographies. These topographies are defined to further subdivide the industrial environment into different surroundings for which significantly different large-scale and temporal fading behavior is expected. Large-scale fading is found to be excellently described by a one-slope path loss model and to agree well with lognormal fading statistics. Temporal fading is found to correspond well to Ricean statistical distributions.

In Chapter 3, a validation of the industrial large-scale fading and temporal fading models by a number of site survey measurements is presented for an IEEE 802.11b/g wireless system. More specifically, it is investigated if the wireless range according to the industrial propagation models matches the range extracted from site survey measurements. The comparison between propagation models and site survey is made for three practically important 802.11b/g data rates of 2, 11, and 18 Mbps. Generally good statistical agreement is established between the theoretical range according to the propagation models and the empirical range according to the site survey measurements.

In Chapter 4, measurements of the industrial power delay profile are presented. Power delay profiles are graphs representing the power of propagating waves versus their corresponding propagation delay between transmitter and receiver. By this definition, power delay profiles allow to assess the time dispersion of received power. Measurements of the power delay profile are performed through frequency-domain channel sounding from 800 MHz to 4 GHz and by using the virtual antenna array method. The power delay profiles, averaged over a small-scale fading area, were found to clearly exhibit clustering of received power as function of time delay. Because of this, the well-known Saleh-Valenzuela model for the averaged power delay profile is fitted to the measurement data.

In Chapter 5, parameters associated with discrete propagating waves (propagation paths) in an office environment are extracted using the ESPRIT algorithm. The estimated path parameters include azimuth of arrival, azimuth of departure, delay, and power. In agreement with the geometry-based stochastic type of channel models, the path parameters are grouped into clusters using the statistical K-power-means algorithm. Statistical distributions of the propagation parameters within individual clusters are determined, and the correlations between these parameters are assessed. The distributional location and scale parameters are subsequently used to characterize the intra-cluster and inter-cluster dynamics of the propagation path parameters. This is done by in turn determining the statistical distributions of these location and scale parameters, and by considering their correlations. Additionally in Chapter 5, a new notation for the MIMO channel matrix is given which more visibly shows the clustered nature of propagation paths, i.e., FActorization into a BLock-diagonal Expression (FABLE).

In Chapter 6, measurements and ray-tracing simulations of the vehicle penetration loss are presented for a mini-van at 600, 900, 1800, and 2400 MHz. The mean measured vehicle penetration loss varies from 3.2 to 23.8 dB, depending on frequency, illuminated vehicle side, and in-vehicle antenna orientation. Overall good agreement between measured and simulated vehicle penetration loss is found. Vehicle penetration losses follow a lognormal distribution closely, with measured standard deviations ranging between 3.0 and 4.7 dB.

1 Introduction

1.1 Context and motivation

Over the last few decades, wireless communication networks have become omnipresent in our everyday lives. The wireless revolution truly started in the early nineties of the last century with the advent of Second Generation (2G) (digital) cellular technologies such as Global System for Mobile communication (GSM), General Packet Radio Service (GPRS), and Enhanced Data rates for GSM Evolution (EDGE). These wireless communication technologies eventually led to the conception of Third Generation (3G) cellular networks at the start of this century. 3G focuses on improved data rates over 2G systems: peak data rates of at least 200 kbit/s must be achieved for a technology to be called 3G. The most well-known 3G technologies comprise Universal Mobile Telecommunications System (UMTS), High Speed Packet Access (HSPA), and Worldwide Interoperability for Microwave Access (WiMAX). Inevitably, the ever-increasing push towards higher data rates has recently led to Fourth Generation (4G) cellular systems, which are required to deliver peak data rates of at least 100 Mbit/s. Although 4G is still in the development stage, possible 4G candidate technologies are Long Term Evolution Advanced (LTE Advanced) and Mobile WiMAX Release 2.

The wireless communication systems in the previous paragraph can be categorized under the broader family of Wireless Metropolitan Area Networks (WMANs) and Wireless Wide Area Networks (WWANs). These networks provide (mobile) data communication in a large geographical area, spanning a whole city or country. In parallel, innovation in wireless technology also happened in the last few years of

the last century in the area of Wireless Local Area Networks (WLANs). WLANs cover a much smaller area, most commonly indoors, such as an office floor or the rooms of a house. The prime example of the success of WLAN technology is the high adoption of Institute of Electrical and Electronics Engineers (IEEE) 802.11 systems among businesses and individuals.

In the near future, there seems no end to the research effort that is being put towards faster and more robust wireless technologies. Research is continuing in topics such as Multiple Input Multiple Output (MIMO), which exploits the spatial structure of the wireless channel to increase capacity and/or signal-to-noise ratio. In wireless research, it is important to note that the real-life performance of wireless technology in terms of signal-to-noise ratio, achieved data rate, and bit error rate will only be as good as the wireless channel lets it be. There is very little opportunity to "engineer" the channel, the channel is there for the researcher to characterize and to possibly find "exploits" which result in better system performance. To gauge what limitations the environment imposes on real-life system performance, propagation models have to be developed. **The development of propagation models for the aforementioned cellular and WLAN technologies is the general topic of this dissertation**. The provided models are measurement-based and specifically target indoor environments.

1.2 Propagation modelling

1.2.1 Multipath propagation

In propagation modelling, the wirelessly transmitted signal is assumed to arrive at the receiving antenna under the form of a collection of plane waves, also called propagation paths or MultiPath Components (MPCs). Each MPC travels from transmitting antenna to receiving antenna while interacting with physical objects in the environment. These interactions happen because the wave impedance of these objects is different from the wave impedance of the surrounding air (often denoted as "free space"), thus giving rise to electromagnetic phenomena such as reflections, diffractions, transmissions, and scattering [1]. Between two consecutive interactions, waves are assumed to travel in a straight line (hence "plane" waves). For interactions at the air-object interface, electromagnetic theory has come up with relations between the incident, reflected, and refracted angles of the plane waves (e.g., Snell's law for refraction). Simply put, an MPC can be seen as a straight line travelling from the transmitter, changing direction whenever it interacts with an object while obeying the aforementioned relations between angles, before finally arriving at the receiver's side. In a realistic environment, due to a multitude of possible interacting objects, it is easy to comprehend that a multitude of possible MPCs will arise. This phenomenon is called *multipath propagation* [1].

Multipath propagation is schematically shown in Fig. 1.1.

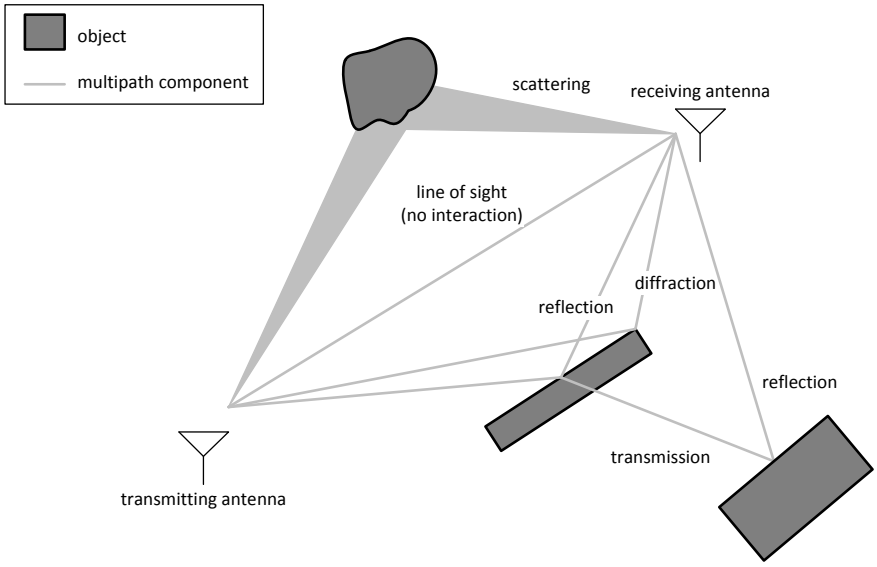

Figure 1.1: Multipath propagation

As mentioned in the previous paragraph, it is assumed that MPCs travel as plane waves in free space. This is a very common assumption, although in some areas of propagation modelling this assumption has not to be fulfilled strictly. Plane-wave propagation can reasonably be assumed if the physical objects closest to the transmitting and receiving antenna are in the so-called far field of both antennas. At a far enough distance from an antenna, electromagnetic wavefronts can be considered spherical. As the distance from the antenna is increased, the radius of the spherical wavefronts increases (or their curvature decreases) and the wavefronts can, with certain error bounds, *locally* assumed to be plane. The distance beyond which this happens is called the far-field region of the antenna [2].

1.2.2 Physical versus analytical models

There exist two major types of models for describing wireless propagation between a transmitter and a receiver: physical and analytical models [3]. These two types of models are discussed in the following.

1.2.2.1 Physical models

Physical channel models describe wireless propagation in terms of parameters of MPCs. Various parameters can be associated with MPCs, including [3, 4]:

- *Directional parameters* which describe the spatial properties of the MPCs. These parameters are the two angles (with respect to some preset reference direction) at which an MPC leaves the transmitting antenna and arrives at the receiving antenna. Each of these two angles is fully specified by its azimuth and elevation angle in a spherical coordinate system.

- A *delay parameter* which quantifies the amount of time it takes for an MPC to travel from the transmitting to the receiving antenna. The delay parameter is equal to the MPC's travelled distance divided by the speed of light in free space.

- A *complex amplitude parameter* which expresses the magnitude and phase of the MPC's electric or magnetic field as seen at the receiving antenna. The magnitude is usually normalized to the magnitude of the field at the transmitting antenna and the phase is defined with respect to the field's phase at the transmitting antenna. The squared magnitude of the received field is proportional to the power of the MPC.

The *orientation (polarization)* of the received electric or magnetic field is missing from the above list of MPC parameters. MPC polarization properties are usually handled by splitting the complex amplitude parameter in three separate complex amplitudes. Each of these amplitudes then corresponds to the complex amplitude of the orthogonal projection of the field onto one of three orthogonal directions in space. The different MPC parameters can also be seen as multiple dimensions in MPC parameter space; physical channel modelling is therefore also sometimes referred to as *multidimensional channel modelling*.

It is also important to remark that it is possible for an MPC parameter value to change over time. These changes are caused by the time-variance of the wireless channel, i.e., changes in the physical layout of the channel by movement of people or objects, and/or receiver movement. This dynamic behavior is represented by the channel's Doppler spectrum. Furthermore, this Doppler spectrum is only valid within a frame of time in which the channel's statistical behavior remains essentially the same, or in technical terms "(wide-sense) stationary". Physical channel modelling therefore also requires to specify the time frame during which stationarity can be assumed [3].

Physical channel models do not necessarily describe the behavior of the MPC parameters of individual MPCs. Some physical channel models group MPCs into clusters, and from there on provide mathematical descriptions of average and spread values of MPC parameters seen over all MPCs in a cluster. This leads to some newly defined parameters, derived from the MPC parameters listed above, but are associated with two or more MPCs in the channel. For example, the parameter "path loss" is defined as the total loss in power of all MPCs in the channel

combined. The parameter "delay spread" is defined as the square root of the power-weighted second central moment of the MPC delay parameters of all MPCs in the channel. These derived parameters are also considered to be part of the concept of physical channel modelling.

1.2.2.2 Analytical models

Analytical channel models are a different breed than physical channel models. Where physical channel models essentially aim at reconstructing the collection of MPCs present in the channel, analytical channels models do not attempt to describe the channel in terms of its propagation paths. Analytical channel models instead directly provide mathematical (statistical) models for the (complex) channel transfer function between transmitting antenna(s) and receiving antenna(s) [1, 3]. This channel transfer function is a function of one or more independent variables. The channel transfer function can for example be dependent on the frequency variable or, in case of MIMO systems, on two spatial variables representing the position of two antennas in the transmitting and receiving antenna array, respectively. In addition to a mathematical model for the channel transfer function, analytical models also provide some information about the second-order statistics of the channel transfer function. These second-order statistics consist of the correlations between the channel transfer function at two different values of the frequency and/or spatial variables.

An example of an analytical model for MIMO systems is the "narrowband i.i.d. Rayleigh fading" model, where i.i.d. stands for "independent and identically distributed" [5]. "Narrowband" in this case means that the channel transfer function is not dependent on the frequency variable. "Identically distributed Rayleigh fading" means that the channel transfer function is a zero-mean circularly symmetric complex Gaussian random variable with equal variance for each possible value of the spatial variables. Finally, "independent" implies that the correlation (the second-order statistics) of the channel transfer function at different values of one or two of the spatial variables, is zero.

1.2.2.3 Comparison and choice in this thesis

Physical and analytical channel models serve different purposes. Physical channel models are attractive in the sense that they only model what is present in the channel (i.e., the MPCs) and are independent of the radiation patterns of the antennas or antenna arrays at transmit and receive side. This is not the case for analytical models. Analytical channel models include the antenna radiation patterns in their description, which means that a change in antenna configuration requires that a different analytical model is used. For example, the analytical narrowband i.i.d. Rayleigh fading model of the previous section is strictly speaking only applica-

ble in the case of isotropic antennas. However, analytical models do have a benefit over physical channel models in the fact that they provide an easy, closed-form (analytical) expression of the channel transfer function. This makes them particularly useful in the design of channel coding algorithms, e.g., forward error correction schemes, space-time codes, etc. The closed-form channel transfer function allows to analytically calculate performance metrics of these channel coding algorithms. It is also possible to quickly assess the impact on performance if a certain parameter of the analytical model would have another value. For example for MIMO systems, analytical channels models can quickly answer questions like: „if the signals on each these antennas in this antenna array would be more correlated, what would happen to the overall performance of our space-time coding scheme?".

Because this dissertation does not focus on the design of channel coding algorithms and their performance, analytical models are not considered in this work. **Instead, the goal of this doctoral research is the development of physical channel models.** Physical channel models deal with the reality of the channel by modelling the propagating waves, while analytical models make abstraction of this reality. Physical channel models are therefore more suitable for understanding and learning about the mechanics of propagation, which is one of the goals set for this work[1]. **It is also important to mention that the MPC parameters of the physical channel models will be characterized statistically.** In a realistic propagation channel, there is an inherent arbitrariness to the location of scatterers and therefore to the characteristics of MPCs. This justifies a statistical approach to modelling MPC parameters.

1.2.3 Deterministic versus empirical models

Within the group of **physical channel models**, a distinction is made between deterministic and empirical models [3, 6].

1.2.3.1 Deterministic models

Deterministic channel models calculate the propagating MPCs in the wireless channel through ray-tracing simulations. For these kind of simulations, an accurate three-dimensional (3-D) model of the propagation environment is required [3, 6]. Ray-tracing simulations most commonly work by shooting rays (plane waves) off a transmitting point in all directions within a 4π steradian solid angle. These rays then interact with the geometrical shapes of the 3-D model of the environment. Eventually, some of the rays that bounce off these shapes will arrive at the receiv-

[1] It should be noted that physical channel models can equally be used for performance testing of channel coding schemes. This is self-evident as both physical and analytical models describe the same phenomenon, i.e., the wireless channel. However for the sole purpose of system design, analytical models are much easier to handle, while using physical models would often mean making a needlessly complex detour to achieve this purpose.

ing point and count as actual MPCs. In addition to the geometrical shapes, the 3-D model must also contain electrical parameters of the shapes' materials. These are necessary for the calculation of the materials' reflection, transmission, and diffraction coefficients which determine the MPCs' complex electric and magnetic fields at the receiving point.

1.2.3.2 Empirical models

Empirical channel models determine parameters of MPCs through field measurements in the actual environment under consideration. A signal generator and a transmitting antenna are used to excite the wireless channel. The wirelessly transmitted signal is picked up by a receiving antenna, and analyzed and stored by receiver equipment such as a spectrum analyzer or a network analyzer. This type of measurement procedure for the probing of wireless channels is commonly referred to as 'channel sounding' [6]. Measurement data gathered in a channel sounding campaign often requires some sort of post-processing. Post-processing is necessary to remove the so-called "non-channel responses", i.e., unwanted influences of the measurement equipment on the measured data set. These influences comprise among other things, noise induced by the receiver equipment, limited dynamic range of the receiver equipment, antenna and amplifier gains, cable losses, etc. Additional post-processing is required in cases where the measurement setup does not allow to measure MPC parameters directly. Sampling of the wireless channel in the spatial and frequency domains can for example be used to determine the MPC directional and delay parameters, respectively, after applying post-processing on the sampled data under the form of harmonic retrieval algorithms.

1.2.3.3 Comparison and choice in this thesis

The largest part of this work focuses on the development of physical empirical models. Empirical models are chosen over deterministic models mainly because of the type of environment is indoor. Indoor environments present some difficulties for deterministic ray-tracing simulations with respect to the required accuracy of the 3-D model. A floor plan of the indoor environment with walls, floors and ceilings is easily imported in ray-tracing software. However, indoor environments usually also contain a significant amount of clutter, e.g., desks, personal computers and filing cabinets in offices. This clutter is expected to heavily affect wireless propagation, as it usually occupies a large part of the free space in these environments. Indoor clutter is difficult and very time-consuming to include in the 3-D model. In contrast, clutter in outdoor environments, i.e., all objects not including buildings, such as vehicles, lampposts, and traffic lights, have a much smaller effect on wireless propagation because in comparison they only occupy a small part of the total space in these environments.

In addition to an accurate 3-D model, ray-tracing also requires accurate models of wave propagation. While implementing specular reflection and transmission in a ray-tracing tool is straightforward due to exact mathematical formulations of these phenomena, other interaction mechanisms such as diffraction and scattering pose greater concern. The mechanics behind diffraction and scattering in realistic environments are often too complex to be computationally tractable. It is for this reason often necessary to use a simplified numerical method for these kind of calculations, e.g., uniform theory of diffraction and Kirchhoff's solution for scattering from rough surfaces. These numerical methods commonly make assumptions (simplifications) about the air-object interface which cannot always be checked and could give rise to errors of unknown magnitude. There is however ongoing research regarding the integration of increasingly complex but computationally feasible models for diffraction and scattering in ray-tracing software, e.g., for scattering in [7].

Because of these difficulties and uncertainties related to deterministic ray-tracing in indoor environments, I opted for the development of empirical models. As mentioned above, empirical models also contain uncertainties under the form of non-channel responses and limited accuracy of harmonic retrieval algorithms. During the course of my doctoral research, these were however found to be well documented in literature and I could also build on the already present know-how in the WIreless and CAble research group (WICA) when it comes to the correct usage of measurement equipment.

To end this section on a lighter note, I quote the following wisdom in propagation science [8]: *„the difference between measurements and simulations is that nobody believes in simulations, except the one who did them, but everybody believes in measurements, except the one who did them"*. But that should not stop us from researching at least one of them.

1.3 Indoor environments

This section provides a short motivation of the choice of indoor environments considered in this work.

1.3.1 Industrial environment

Industrial manufacturing centers are increasingly interested to incorporate wireless communication in their production processes. Production lines in contemporary factories are often changed, improved, or moved. This implies highly dynamic changes of the workplace layout over time. As a result, wired communication between two pieces of machinery would require frequent rerouting of cables, which is costly and time consuming. A more flexible solution would be to use wireless

communication between machinery. Integration of wireless communication in the industrial environment however poses new challenges. The radio channel in factories will behave much differently with respect to the radio channel of e.g., office buildings, due to the more open building layout, the presence of machinery, and the presence of highly reflective materials such as metal. This stresses the need for developing and improving wave propagation models specifically for factory environments. However, few attempts have been made in literature to characterize the industrial environment concerning electromagnetic wave propagation.

In this work, measurements are performed to reflect a specific kind of industrial communication, namely communication between an access point located at a considerable height of about 6 m and wireless terminals situated at smaller heights of about 2 m. These heights are commonly used for the installation of wireless access points and wireless terminals in industrial environments. In factories, cables are often arranged in cable racks as part of a wired network. Generally, these cable racks are mounted on the metal trusses close to the ceiling at approximately 6 m height. As a consequence, wireless access points are often installed on those cable racks to easily connect them to the wired network. Furthermore, a terminal height of 2 m is chosen as it is approximately the same height as for wireless terminals mounted on machinery or fork-lift trucks. This kind of communication has various important applications, such as access points which communicate with a large number of wireless sensor nodes in a production line to monitor and adjust parameters of the industrial processes, and access points which provide terminals on fork-lift trucks with information about the current stock in the warehouse.

1.3.2 Office environment

Over the last decade, WLAN technology has become indispensable in a modern day office environment. The popularity of office WLANs goes hand in hand with the increased use of portable notebooks, which over the years have attained a sufficient level of power and compactness to comfortably do office tasks while being mobile. The majority of modern companies allow visitors to connect to a WLAN, so they can access the internet during work meetings. Today, the most widely used WLAN technology standard is IEEE 802.11a/b/g. It is however expected that a move towards the recently approved IEEE 802.11n standard will happen. IEEE 802.11n offers various improvements over IEEE 802.11a/b/g to increase the achievable physical bitrate from 54 to 600 Mb/s. The most important among these improvements is the addition of MIMO technology.

In this work, an empirical propagation model is developed for IEEE 802.11n in an office environment. Because of the spatial character of MIMO (i.e., multiple antennas spread in space), the angular parameter of MPCs is vitally important for assessing the performance of this technology. Measurements of the angular

parameter will therefore be presented.

1.3.3 Vehicular environment

In wireless cellular networks, the possibility to use mobile communication devices inside transportation vehicles is often desirable. For example, to receive real-time updates on highway traffic conditions through 3G, a working in-vehicle connection is required. In comparison with outdoor use, the received in-vehicle signal power level can be substantially smaller. For reliable coverage planning with in-vehicle reception, it is necessary to determine how much power loss a signal undergoes when propagating from outside to inside the vehicle. This power loss is also called Vehicle Penetration Loss (VPL) and its statistics have been determined for a couple of propagation scenarios in this doctoral thesis. VPL statistics are important for service providers to calculate margins for power link budgets, which will give the expected reduction in wireless cell size when in-vehicle reception is required.

1.4 Outline

The general topic of this dissertation is empirical propagation modelling in indoor environments. This section sums up the different chapters in this thesis, along with the kind of propagation variables and the kind of indoor environments that are under consideration in each chapter. The research of each chapter led to an peer-reviewed publication in an international journal, which are referenced in the following and can be found in the publication list in the next section.

- Chapter 2 investigates location and time variability of path loss (the so-called large-scale and temporal fading) in industrial environments [ET1].
- Chapter 3 validates the industrial large-scale and temporal fading models developed in Chapter 2 against the real-life performance of an off-the-shelf IEEE 802.11b/g wireless system. The comparison between both is done in terms of achievable wireless range for a set of fixed values of physical bitrate [ET2].
- Chapter 4 discusses the distribution of the delay parameter of MPCs in an industrial environment. This comprises the analysis of measured Power Delay Profiles (PDPs), i.e., the power of received MPCs versus their corresponding delay parameter [ET3].
- Chapter 5 analyzes the angular and delay characteristics of MPCs in an office environment. The focus is on the clustering of these parameters. The analysis comprises the statistical treatment of the angular and delay parameters within individual clusters (intra-cluster statistics) and the change in

these parameters from one cluster to another (inter-cluster statistics). Building on the concept of multipath clusters, this chapter also presents a new notation of the MIMO channel matrix, named FActorization into a BLock-diagonal Expression (FABLE), which more visibly shows the clustered nature of MPCs [ET4].

- Chapter 6 presents a statistic analysis of VPL measurements carried out with a mini-van. Additionally, the VPL measurements are validated by 3-D ray-tracing simulations [ET5].

The most important contribution of this work is that it fills a few gaps in current propagation research when it comes to the type of indoor environments that are commonly considered. Particularly, propagation models for industrial indoor channels are scarce in literature. For this reason, very special focus is given to factory environments in this work, which encompasses three of the five research chapters. The work of chapters 2 to 4 was carried out with the financial support of the Institute for the Promotion of Innovation by Science and Technology in Flanders within the TETRA project “problematiek betreffende de integratie van moderne communicatiesystemen in een industriële automatiseringsomgeving”. The work of chapter 5 was done in close collaboration with research group TELICE of the University of Lille (France) and was supported by the Interdisciplinary institute for BroadBand Technology (IBBT) project DEUS. The work of chapter 6 was supported by the IBBT project MADUF.

1.5 Publications

1.5.1 A1

(publications in journals listed in the ISI Web of Science)

1.5.1.1 As first author

[ET1] **E. Tanghe**, W. Joseph, L. Verloock, L. Martens, H. Capoen, K. Van Herwegen, and W. Vantomme, ”The Industrial Indoor Channel: Large-Scale and Temporal Fading at 900, 2400, and 5200 MHz,” *IEEE Transactions on Wireless Communications*, vol. 7, no. 7, pp. 2740-2751, July 2008.

[ET2] **E. Tanghe**, W. Joseph, L. Verloock, L. Martens, H. Capoen, K. Van Herwegen, and T. Buysschaert, ”Statistical Validation of WLAN Range Calculated with Propagation Models for Industrial Environments by Chipset-level RSS Measurements,” *IET Science, Measurement and Technology*, vol. 3, no. 3, pp. 244-255, May 2009.

[ET3] **E. Tanghe**, W. Joseph, J. De Bruyne, L. Verloock, and L. Martens, "The Industrial Indoor Channel: Statistical Analysis of the Power Delay Profile," *International Journal of Electronics and Communications*, vol. 64, no. 9, pp. 806-812, September 2010, doi:10.1016/j.aeue.2009.06.003.

[ET4] **E. Tanghe**, W. Joseph, M. Liénard, A. Nasr, P. Stefanut, L. Martens, and P. Degauque, "Statistical Analysis of Multipath Clustering in an Indoor Office Environment," *EURASIP Journal on Wireless Communications and Networking*, 2011, Article ID 263134, 16 pages, doi:10.1155/2011/263134.

[ET5] **E. Tanghe**, W. Joseph, L. Verloock, and L. Martens, "Evaluation of Vehicle Penetration Loss at Wireless Communication Frequencies," *IEEE Transactions on Vehicular Technology*, vol. 57, no. 3, pp. 2036-2041, July 2008.

1.5.1.2 As co-author

[ET6] D. Plets, W. Joseph, L. Verloock, **E. Tanghe**, L. Martens, E. Deventer, and H. Gauderis, "Influence of Reception Condition, MPE-FEC Rate and Modulation Scheme on Performance of DVB-H," *IEEE Transactions on Broadcasting*, vol. 54, no. 3, pp. 590-598, September 2008.

[ET7] W. Joseph, D. Plets, L. Verloock, **E. Tanghe**, L. Martens, E. Deventer, and H. Gauderis, "Procedure to Optimize Coverage and Throughput for a DVB-H System Based on Field Trials," *IEEE Transactions on Broadcasting*, vol. 54, no. 3, pp. 347-355, September 2008.

[ET8] D. Plets, W. Joseph, L. Verloock, **E. Tanghe**, L. Martens, H. Gauderis, and E. Deventer, "New Method to Determine the Range of DVB-H Networks and the Influence of MPE-FEC Rate and Modulation Scheme," *EURASIP Journal on Wireless Communications and Networking*, 2009, Article ID 524163, 10 pages, doi:10.1155/2009/524163.

[ET9] J. De Bruyne, W. Joseph, D. Plets, L. Verloock, **E. Tanghe**, and L. Martens, "Comparison of the Link Budget with Experimental Performance of a WiMAX System," *EURASIP Journal on Wireless Communications and Networking*, 2009, Article ID 247436, 8 pages, doi:10.1155/2009/247436.

[ET10] J. Van Ooteghem, B. Lannoo, K. Casier, S. Verbrugge, **E. Tanghe**, W. Joseph, L. Martens, D. Colle, M. Pickavet, I. Moerman, and P. Demeester, "Municipalities as a Driver for Wireless Broadband Access," *Wireless Personal Communications Journal*, vol. 49, no. 3, pp. 391-414, April 2009.

[ET11] W. Joseph, L. Verloock, **E. Tanghe**, and L. Martens, "In-Situ Measurement Procedures for Temporal RF Electromagnetic Field Exposure of the General Public," *Health Physics*, vol. 96, no. 5, pp. 529-542, May 2009.

[ET12] W. Joseph, L. Verloock, D. Plets, **E. Tanghe**, and L. Martens, "Characterization of Coverage and Indoor Penetration Loss of DVB-H Signal of Indoor Gap Filler in UHF Band," *IEEE Transactions on Broadcasting*, vol. 55, no. 3, pp. 589-597, September 2009.

[ET13] E. Reusens, W. Joseph, B. Latré, B. Braem, G. Vermeeren, **E. Tanghe**, L. Martens, C. Blondia, and I. Moerman, "Characterization of On-Body Communication Channel and Energy Efficient Topology Design for Wireless Body Area Networks," *IEEE Transactions on Information Technology in Biomedicine*, vol. 13, no. 6, pp. 933-945, November 2009.

[ET14] K. De Moor, W. Joseph, I. Ketyko, **E. Tanghe**, T. Deryckere, L. Martens, and L. De Marez, "Linking Users' Subjective QoE Evaluation to Signal Strength in an IEEE 802.11b/g Wireless LAN Environment," *EURASIP Journal on Wireless Communications and Networking*, 2010, Article ID 541568, 12 pages, doi:10.1155/2010/541568.

[ET15] M. Deruyck, **E. Tanghe**, W. Joseph, W. Vereecken, M. Pickavet, L. Martens, and B. Dhoedt, "Model for Power Consumption of Wireless Access Networks", *IET Science, Measurement and Technology*, 2011, accepted.

[ET16] M. Deruyck, **E. Tanghe**, W. Joseph, and L. Martens, "Modelling and Optimization of Power Consumption in Wireless Access Networks," *Elsevier Computer Communications - special issue: European Wireless 2010*, 2011, accepted.

1.5.2 B2

(chapters in books)

1.5.2.1 As co-author

[ET17] W. Joseph and **E. Tanghe**, chapter "Modeling Diffuse Multipaths", in *"COST2100 book"*, edited by R. Verdone, to be published 2011.

1.5.3 P1

(publications in conference proceedings listed in the ISI Web of Science)

1.5.3.1 As first author

[ET18] **E. Tanghe**, W. Joseph, L. Verloock, L. Martens, H. Capoen, K. Van Herwegen, and W. Vantomme, "Large-Scale Fading in Industrial Environments at Wireless Communication Frequencies," in *IEEE Antennas and Propagation International Symposium*, Honolulu, HI, US, June 2007, pp. 3001-3004.

[ET19] **E. Tanghe**, W. Joseph, L. Verloock, L. Martens, H. Capoen, K. Van Herwegen, and T. Buysschaert, "Range of an IEEE 802.11b/g System in Industrial Environments based on Site Survey Measurements and Propagation Models," in *IEEE Antennas and Propagation International Symposium*, San Diego, CA, US, July 2008, pp. 372-375.

[ET20] **E. Tanghe**, W. Joseph, L. Verloock, L. Martens, H. Capoen, K. Van Herwegen, and W. Vantomme, "Characterization of Temporal Fading for a Traffic Monitoring System," in *IEEE Antennas and Propagation International Symposium*, San Diego, CA, US, July 2008, pp. 484-487.

[ET21] **E. Tanghe**, W. Joseph, J. De Bruyne, L. Verloock, and L. Martens, "Statistical Modelling of Power Delay Profiles and Small-scale Fading in Industrial Environments," in *IEEE Antennas and Propagation International Symposium*, Charleston, SC, US, June 2009.

[ET22] **E. Tanghe**, W. Joseph, M. Liénard, A. Nasr, P. Stefanut, L. Martens, and P. Degauque, "Statistics of Multipath Component Clustering in an Office Environment," in *4th European Conference on Antennas and Propagation*, Barcelona, ES, April 2010.

1.5.3.2 As co-author

[ET23] W. Joseph, **E. Tanghe**, D. Pareit, and L. Martens, "Building Penetration Measurements for Indoor Coverage Prediction of DVB-H Systems," in *IEEE Antennas and Propagation International Symposium*, Honolulu, HI, US, June 2007, pp. 3005-3008.

[ET24] D. Plets, W. Joseph, **E. Tanghe**, L. Verloock, and L. Martens, "Analysis of Propagation of Actual DVB-H Signal in a Suburban Environment," in *IEEE Antennas and Propagation International Symposium*, Honolulu, HI, US, June 2007, pp. 1997-2000.

[ET25] D. Plets, **E. Tanghe**, W. Joseph, L. Verloock, L. Martens, E. Deventer, and H. Gauderis, "Influence of Building Type on Penetration Loss in

UHF Band for 100 Buildings in Flanders," in *IEEE Antennas and Propagation International Symposium*, San Diego, CA, US, July 2008, pp. 464-467.

[ET26] D. Plets, W. Joseph, L. Verloock, **E. Tanghe**, L. Martens, E. Deventer, and H. Gauderis, "Influence of Modulation Scheme on the Range for Good Reception in DVB-H Networks," in *European Wireless Technology Conference*, Amsterdam, NL, October 2008, pp. 57-60.

[ET27] D. Plets, W. Joseph, L. Verloock, **E. Tanghe**, L. Martens, E. Deventer, and H. Gauderis, "Optimal Selection DVB-H System Settings for Indoor Reception," in *IEEE International Symposium on Broadband Multimedia Systems and Broadcasting*, Bilbao, ES, May 2009, pp. 700-704.

[ET28] D. Plets, W. Joseph, **E. Tanghe**, and L. Martens, "Evaluation of Temporal Fading Characteristics of a DVB-H Signal for Different Reception Categories," in *IEEE Antennas and Propagation International Symposium*, Charleston, SC, USA, June 2009.

[ET29] D. Plets, W. Joseph, L. Verloock, **E. Tanghe**, and L. Martens, "Evaluation of Indoor Penetration Loss and Floor Loss for a DVB-H Signal at 514 MHz," in *IEEE International Symposium on Broadband Multimedia Systems and Broadcasting*, Shanghai, CN, March 2010.

[ET30] M. Deruyck, **E. Tanghe**, W. Joseph, D. Pareit, I. Moerman and L. Martens, "Performance Analysis of WiMAX for Mobile Applications," in *IEEE Wireless Communications and Networking Conference*, Sydney, AU, April 2010.

[ET31] D. Pareit, V. Petrov, B. Lannoo, **E. Tanghe**, W. Joseph, I. Moerman, P. Demeester, and L. Martens, "A Throughput Analysis at the MAC Layer of Mobile WiMAX," in *IEEE Wireless Communications and Networking Conference*, Sydney, AU, April 2010.

[ET32] M. Deruyck, W. Vereecken, **E. Tanghe**, W. Joseph, M. Pickavet, L. Martens, and P. Demeester, "Power Consumption in Wireless Access Networks," in *European Wireless Conference*, Lucca, IT, April 2010, pp. 924-931.

[ET33] M. Deruyck, W. Vereecken, **E. Tanghe**, W. Joseph, M. Pickavet, L. Martens, and P. Demeester, "Comparison of Power Consumption of Mobile WiMAX, HSPA and LTE Access Networks," in *9th Conference on Telecommunications Internet and Media Techno Economics*, Ghent, BE, June 2010.

[ET34] L. Verstrepen, W. Joseph, **E. Tanghe**, J. Van Ooteghem, B. Lannoo, M. Pickavet, L. Martens, and P. Demeester, "Making a Well-founded Choice of the Wireless Technology for Train-to-wayside Data Services," in *9th Conference on Telecommunications Internet and Media Techno Economics*, Ghent, BE, June 2010.

[ET35] D. Plets, W. Joseph, K. Vanhecke, **E. Tanghe**, L. Martens, S. Bouckaert, I. Moerman, and P. Demeester, "Validation of Path Loss by Heuristic Prediction Tool with Path Loss and RSSI Measurements," in *IEEE Antennas and Propagation International Symposium*, Toronto, CA, July 2010.

[ET36] M. Deruyck, **E. Tanghe**, W. Joseph, W. Vereecken, M. Pickavet, B. Dhoedt, and L. Martens, "Towards a Deployment Tool for Wireless Access Networks with Minimal Power Consumption," in *IEEE 21st International Symposium on Personal, Indoor and Mobile Radio Communications*, Istanbul, TR, September 2010, pp. 295-300.

[ET37] D. Gaillot, **E. Tanghe**, P. Stefanut, W. Joseph, M. Liénard, P. Degauque, and L. Martens, "Accuracy of Specular Path Estimates with ESPRIT and RiMAX in the Presence of Measurement-based Diffuse Multipath Components," in *5th European Conference on Antennas and Propagation*, Rome, IT, April 2011, accepted.

[ET38] F. Heereman, W. Joseph, **E. Tanghe**, D. Plets, and L. Martens, "Prediction of Range, Power Consumption and Throughput for IEEE 802.11n in Large Conference Rooms," in *5th European Conference on Antennas and Propagation*, Rome, IT, April 2011, accepted.

[ET39] A. Bamba, J. B. Andersen, W. Joseph, D. Plets, **E. Tanghe**, G. Vermeeren, J. Ø. Nielsen, and L. Martens, "Experimental Specific Energy Absorption Rate Assessment from Absorption Cross Section Measurement for Far-field Exposure at 2-3 GHz," in *33rd Annual Meeting of the Bioelectromagnetics Society*, Halifax, CA, June 2011, accepted.

[ET40] F. Heereman, W. Joseph, **E. Tanghe**, D. Plets, and L. Martens, "Development of Path Loss Model for 802.11n in Large Conference Rooms," in *IEEE Antennas and Propagation International Symposium*, Spokane, WA, US, July 2011, accepted.

[ET41] A. Bamba, W. Joseph, D. Plets, **E. Tanghe**, G. Vermeeren, L. Martens, J. B. Andersen, and J. Ø. Nielsen, "Assessment of Reverberation Time by Two Measurement Systems for Room Electromagnetics Analysis," in *IEEE Antennas and Propagation International Symposium*, Spokane, WA, US, July 2011, accepted.

1.5.4 C1

(publications in other conference proceedings)

1.5.4.1 As first author

[ET42] **E. Tanghe**, W. Joseph, and L. Martens, "Characterizing the Industrial Wireless Channel at Practical Frequencies," in *7e UGent - FirW Doctoraatssymposium*, Ghent, BE, November 2006.

[ET43] **E. Tanghe**, W. Joseph, J. De Bruyne, L. Verloock, and L. Martens, "The Industrial Indoor Channel: Statistical Analysis of the Power Delay Profile," in *15th Annual Symposium of the IEEE/CVT Benelux Chapter*, Antwerp, BE, November 2008.

[ET44] **E. Tanghe**, W. Joseph, M. Liénard, A. Nasr, P. Stefanut, D. Gaillot, P. Degauque, and L. Martens, "Clustering of Channel Parameters by Block Diagonal Matrix Decomposition," in *COST 2100 7th Management Committee Meeting*, Braunschweig, DE, February 2009, ref.: TD(09) 712.

[ET45] **E. Tanghe**, W. Joseph, M. Liénard, A. Nasr, P. Stefanut, L. Martens, and P. Degauque, "Statistics of Multipath Component Clustering in an Office Environment," in *COST 2100 10th Management Committee Meeting*, Athens, GR, February 2010, ref.: TD(10) 10019.

1.5.4.2 As co-author

[ET46] D. Plets, L. Verloock, **E. Tanghe**, W. Joseph, L. Martens, E. Deventer, and H. Gauderis, "Evaluation of Performance Characteristics of a DVB-H Network for Different Reception Conditions," in *57th Annual IEEE Broadcast Technology Society Symposium*, Washington DC, US, October 2007.

[ET47] D. Plets, W. Joseph, L. Verloock, **E. Tanghe**, L. Martens, H. Gauderis, and E. Deventer, "Influence of Building Type on Penetration Loss in UHF Band for 100 Buildings in Flanders," in *58th Annual IEEE Broadcast Technology Society Symposium*, Alexandria, VA, US, October 2008.

[ET48] B. Lannoo, J. De Bruyne, W. Joseph, J. Van Ooteghem, **E. Tanghe**, D. Colle, L. Martens, M. Pickavet, and P. Demeester, "Influence of Technical Improvements on the Business Case for a Mobile WiMAX Network," in *4th International Conference on Access Networks*, Hong Kong, CN, November 2009.

[ET49] D. Gaillot, **E. Tanghe**, P. Stefanut, W. Joseph, M. Linard, P. Degauque, and L. Martens, "Accuracy of Specular Path Estimates with ESPRIT and

RiMAX in the Presence of Diffuse Multipath," in *COST 2100 12th Management Committee Meeting*, Bologna, IT, November 2010, ref.: TD(10) 12022.

References

[1] S. R. Saunders. *Antennas and Propagation for Wireless Communication Systems*. Wiley and Sons, 1999.

[2] C. Capps. *Near field or far field?* EDN Magazine, (18):95–102, 2001.

[3] C. Oestges and B. Clerckx. *MIMO Wireless Communications: From Real-World Propagation to Space-Time Code Design*. Academic Press, first edition, 2007.

[4] M. Steinbauer, A. F. Molisch, and E. Bonek. *The Double-Directional Radio Channel*. IEEE Antennas and Propagation Magazine, 43(4):51–63, August 2001.

[5] J. D. Parsons. *The Mobile Radio Propagation Channel*. Wiley, second edition, 2000.

[6] T. S. Rappaport. *Wireless Communications, Principles and Practice*. Prentice Hall PTR, second edition, 2002.

[7] F. Mani, F. Quitin, and C. Oestges. *Evaluation of Diffuse Scattering Contribution in Office Scenario*. In COST 2100 10th Management Committee Meeting, Athens, GR, February 2010. ref.: TD(10) 10001.

[8] N. Czink. *The Random-Cluster Model - A Stochastic MIMO Channel Model for Broadband Wireless Communication Systems of the 3rd Generation and Beyond*. PhD thesis, Technische Universität Wien, Forschungszentrum Telekommunikation Wien, Wien, AT, 2007.

2

Large-scale and temporal fading in industrial environments

2.1 Introduction and related work

The indoor radio channel has been an active area of research in recent years. Various measurement campaigns have been executed to determine propagation characteristics of electromagnetic waves in houses and in office buildings. These measurements resulted in propagation models which support the coverage prediction of wireless networks operating in these environments. The motivation behind this extensive research is the increasing use of indoor wireless communications. Wireless communication standards, such as IEEE 802.11 [1], are already known to perform well in office environments.

The last few years, industrial manufacturing centers are interested to incorporate wireless communication in their production processes. Production lines in contemporary factories are often changed, improved, or moved. This implies highly dynamic changes of the workplace layout over time. As a result, wired communication between two pieces of machinery requires frequent rerouting of cables, which is costly and time consuming. A more flexible solution would be to use wireless communication between machinery. Wireless Local Area Network (WLAN) technology (e.g., IEEE 802.11 [1]) but also Wireless Sensor Network (WSN) technology (e.g., ZigBee [2]) may be integrated in industrial environments in the near future. Integration of wireless communication in the industrial environment however poses new challenges.

The radio channel in factories will behave much differently with respect to the radio channel of e.g., office buildings, due to the more open building layout, the presence of machinery, and the presence of highly reflective materials such as metal. This stresses the need for developing and improving wave propagation models specifically for factory environments. However, few attempts have been made to characterize the industrial environment concerning electromagnetic wave propagation [3, 4]. In [3], narrowband measurements were executed at 1300 MHz to characterize large-scale, small-scale, and temporal fading in food processing, engine manufacturing, and aluminium metalwork facilities. Measurements were executed for transmitter and receiver separations ranging from 10 m up to 80 m. In [4], narrowband measurements at 2450 MHz were performed in a chemical pulp factory, a cable factory, and a nuclear power plant to determine large-scale and small-scale fading. Distances up to 95 m from the transmitter were selected for the measurements.

This research chapter presents narrow-band measurements performed in two wood processing and two metal processing factories at three frequencies, namely 900 MHz, 2400 MHz, and 5200 MHz. These frequencies lie within or near frequency bands recently targeted for application of indoor industrial wireless communication standards [1, 2]: 869.3 to 869.4 MHz, 2400 to 2483.5 MHz, and 5150 to 5825 MHz. Both large-scale and temporal fading are investigated for distances between transmitter and receiver from 15 m up to 140 m. Common characteristics of the industrial environment affecting both types of fading are identified, allowing the classification of the physical surroundings in general topographies for both large-scale fading and temporal fading. Large-scale fading topographies are largely based on the classification made in [3], whereas temporal fading topographies have not previously been described in literature.

In [3] and [4], measurements were done with both transmitting and receiving antennas installed at approximately 2 m above ground level. Our measurements were conducted with transmitting and receiving antenna heights equal to respectively 6 m and 2 m above ground level. These heights are commonly used for the installation of wireless access points and wireless terminals in industrial environments. In factories, cables are often arranged in cable racks as part of a wired network. Generally, these cable racks are mounted on the metal trusses close to the ceiling at approximately 6 m height. As a consequence, wireless access points are often installed on those cable racks to easily connect them to the wired network. Furthermore, a height of 2 m for the receiving antenna was chosen as it is approximately the same height as for wireless terminals mounted on machinery or fork-lift trucks. Therefore, the proposed industrial propagation model could be used to design a wireless system for communication between e.g., an access point and a terminal mounted either on a piece of machinery or a fork-lift truck.

The outline of this chapter is as follows. In Section 2.2, the measurement

setup and the measured factories are described. In Section 2.3, parameters used to characterize large-scale and temporal fading are presented, and definitions of the various large-scale and temporal fading topographies are given. The results of the measured large-scale fading and temporal fading parameters are discussed in Sections 2.4 and 2.5, respectively. Finally, a few conclusions are drawn in Section 2.6.

2.2 Measurement configuration

2.2.1 Measurement apparatus

Propagation experiments in industrial environments were carried out with measurement apparatus including a transmitter and a receiver part, as shown in Fig. 2.1. The transmitter part (see Fig. 2.1(a)) consists of a transmitting antenna (Tx) and a signal generator. As the Tx, omnidirectional vertically polarized antennas of type Kathrein K738449 (900 MHz, 2 dBi), Jaybeam MA431Z00 (2400 MHz, 4.2 dBi), and European Antennas EVD2-5300/1285 (5200 MHz, 2 dBi) were used. The Tx is mounted on a telescopic mast at a height h_{Tx} of about 6 m above ground level. The Tx is positioned at approximately the same height as the trusses supporting the ceiling, a common location for placement of industrial wireless access points. A Rohde & Schwarz SMP22 signal generator was used to inject a continuous wave signal with constant power of about 25 dBm into the Tx. The transmitter is placed at a fixed location in the measurement environment.

The receiver part (see Fig. 2.1(b)) consists of a receiving antenna (Rx) mounted on a plastic mast at a height h_{Rx} of about 2 m above ground level. As the Rx, omnidirectional antennas of the same type as the Tx were used. The Rx height is comparable to the height of a wireless terminal mounted on a piece of machinery. The Rx is connected to a Hewlett-Packard 8561B spectrum analyzer which samples the received power level at the transmitting frequency. Sampled power values are stored on a laptop through a General Purpose Interface Bus (GPIB) connection. The spectrum analyzer's frequency span was set to 300 kHz. The resolution and video bandwidth were both set to 3 kHz. Along with a reference level of 0 dBm, these settings effectuated a noise floor of about -87 dBm. In [5], it is shown that the video bandwidth setting has a negligible effect on the measured power of a continuous wave signal: the measured power of a 900 MHz continuous wave signal varied only 0.07 dBm when changing the video bandwidth setting from 5 kHz to 5 MHz, while leaving the resolution bandwidth and span settings unaltered. This paper also mentions that the resolution bandwidth setting has the largest effect on measured power. However, as the transmitted signal for our measurements is a continuous wave signal with a very small bandwidth, the use of a small resolution bandwidth of 3 kHz is justified. The receiver configuration is constructed on a

movable cart in order to obtain measurement data for a great number of separations between the Tx and the Rx. A tachometer is used to measure the travelled distance. Batteries connected to a DC-to-AC converter provide power to the mobile receiver apparatus.

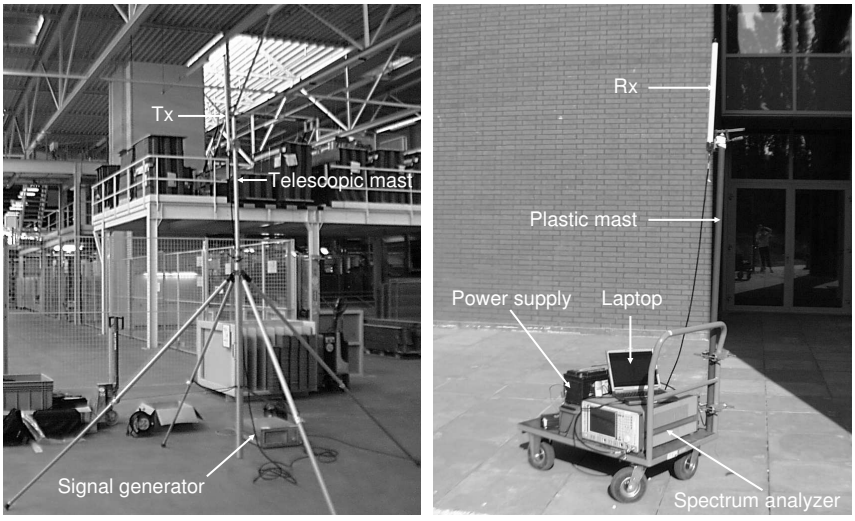

(a) Transmitter part (b) Receiver part

Figure 2.1: Measurement setup

2.2.2 Description of the factory buildings

Propagation measurements were conducted in four modern factories located in Flanders, Belgium. Measured factories include two wood processing facilities and two metal processing facilities. Measured factory buildings exhibited similar physical properties. Buildings have concrete floors and metal ceilings supported by steel truss work. At all factories, building walls are made of thick, precast concrete. Additionally, industrial inventory in all facilities consists for the largest part of similar metal machinery. The height of each building was approximately 7 to 8 m. The proposed propagation model would therefore be applicable to industrial environments sharing these physical characteristics. The models presented in this chapter are not suitable for less common industrial environments, such as for example a nuclear power plant or a large metal foundry.

The wood processing factories produce and store wooden flooring products. Raw wooden materials are processed in workplaces by semi-automated machinery used for sawing, breaking, impregnating, and painting the wood. Fig. 2.2 shows a

Figure 2.2: Wood processing production line

production line for the impregnation of wood. Raw materials and finished products are stacked or stored in metal racks in warehouses.

The metal processing factories include a facility used for the production of metal camp beds. Fig. 2.3 shows a picture of a production line in this facility. Production lines are mostly manual. Finished camp beds are stacked in metal racks in a warehouse. The other metalwork facility is used to roll metal into sheets in a completely automated production line. Heavy metal rolls are stacked in a warehouse using cranes.

Industrial buildings are generally one-storied, because machinery and other industrial inventory can only easily be put on the ground floor due to their size and weight. This eliminates the need for staircases in the majority of workplaces. Closed stairwells were only found in the factory's office buildings and the refectory, and were not considered to be part of the industrial environment. Hence, no propagation experiments were performed in stairwells.

2.3 Method

Prior to the actual measurement campaign, measurements of the background radiation were carried out to ensure there was no interference to our narrowband measurements by e.g., industrial impulsive noise generated by automated welding

Figure 2.3: Metal processing production line

machinery.

2.3.1 Characterization of large-scale fading

2.3.1.1 Definition of large-scale and small-scale fading

Large-scale fading is defined as the variability of received power with distance, seen on average over distance intervals of a few wavelengths [6–8]. Large-scale fading is caused by the so-called shadowing effect: physical objects (machinery, storage racks, etc.) in the propagation channel which either block MultiPath Components (MPCs) or help generate new MPCs through reflections off their surfaces. For this reason, large-scale fading is often also referred to as shadow fading. Large-scale fading can thus be seen as the type of power fading that occurs when there is a significant change in the collection of MPCs that make up the channel (i.e., the multipath profile), more specifically when MPCs disappear because they become blocked or MPCs appear because new physical objects start to participate in the propagation.

The term large-scale fading implies there also exists a type of fading called small-scale fading. Small-scale fading is the variability of received power, seen within small distance intervals no longer than a few wavelengths [6–8]. Contrary to large-scale fading, small-scale fading takes place in a situation where the multipath

profile remains the same. Small-scale fading is the result of two or more MPCs in the profile adding up differently because of changes in their relative phases, caused by a slight alteration of Tx-Rx distance.

Fig. 2.4 gives a visual representation of the two types of fading [8]. Fig. 2.4 shows a graph of measured received power (on a logarithmic scale) versus Tx-Rx distance (on a logarithmic scale). Over the full measured range of distances, it is expected that received power will decrease with distance. This *global* decay of received power is represented by the straight line in Fig. 2.4. Next, the curved line corresponds to a moving average of the power versus distance profile taken with a window of a few wavelengths. This moving average represents the *local* variation of received power and its deviation from the global power decay line is commonly defined as the large-scale or shadow fading. The original, non-averaged power versus distance profile still shows sharp variation around the local and global power fluctuations, in distance intervals smaller than a few wavelengths. This variation is referred to as the small-scale fading.

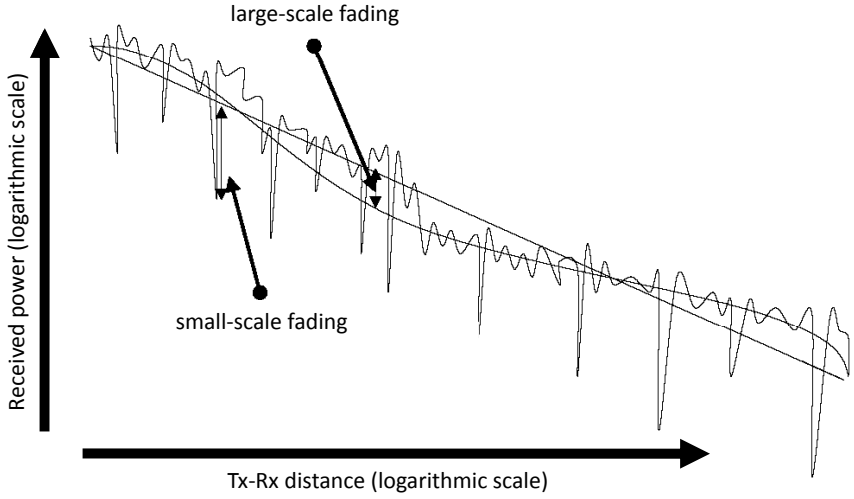

Figure 2.4: Large-scale and small-scale fading

2.3.1.2 Measurement methodology

To determine large-scale fading properties of the industrial environment, the measurement cart was pushed forward at low speed (on average 0.56 m/s at 900 MHz, 0.28 m/s at 2400 MHz, and 0.20 m/s at 5200 MHz) to gather samples of the received power. The movement of the measurement cart can cause Doppler shifts of the MPCs of maximally a few hertz (calculated as the speed of the cart divided

by the wavelength). These Doppler shifts are small compared to the resolution bandwidth of 3 kHz. Because of this, frequency-shifted MPCs are also included in the power measured by the spectrum analyzer. The spectrum analyzer in the receiver part of our measurement configuration allowed us to take approximately 8 samples of the received power per second. The different speeds result in a sampling distance of 7 cm at 900 MHz, 3.5 cm at 2400 MHz and 2.4 cm at 5200 MHz. Therefore, approximately 4.8 samples per wavelength at 900 MHz, 3.6 samples per wavelength at 2400 MHz, and 2.4 samples per wavelength at 5200 MHz were recorded. In [9], it is mentioned that measurements have shown that power samples are uncorrelated for spatial separations greater than half a wavelength in Line Of Sight (LOS) circumstances, while samples are practically uncorrelated at all spatial separations in obstructed LOS circumstances. Consequently, for our measurements, there might be a slight correlation between samples in LOS paths at 900 and 2400 MHz.

To estimate the local mean power, we divided each measurement track into subintervals of 10 wavelengths long. Power levels measured in each subinterval were linearly averaged, and the resulting average was associated with the centre of the subinterval. The choice of a 10 wavelength long subinterval was made according to [10], where it is stated that a 10 wavelength window provides the best compromise between removing small-scale fades without distorting shadow fade patterns. Confidence intervals for estimating the local mean power were calculated theoretically using part of the method described in [11]. This method is based on the assumption that small-scale fading is Rayleigh distributed, which fits some of the industrial small-scale fading data recorded in [3]. For 10 wavelength long subintervals, each time approximately 48 power samples were averaged at 900 MHz, 36 samples at 2400 MHz, and 24 samples at 5200 MHz. Using these values, we calculated 90% confidence intervals as in [11]. It was found that 90% of the calculated local mean power values are within ± 1.0 dB, ± 1.2 dB, and ± 1.4 dB of the true mean power at 900, 2400, and 5200 MHz respectively.

2.3.1.3 Path loss

Large-scale fading characteristics of the industrial radio channel are determined by measurements of the Path Loss (PL). Path loss is defined as the loss of power a wirelessly transmitted signal undergoes when travelling from transmit to receive side [6, 7]. Path loss only accounts for losses MPCs undergo through interaction with objects in the wireless channel, and as such does not include non-channel influences, e.g., antenna gains and antenna feeder losses. Path loss values in dB are computed using the following link budget that assumes omnidirectional antennas:

$$PL = P_T + G_T + G_R - L_T - L_R - P_R \tag{2.1}$$

In (2.1), P_T is the transmitter power in dBm, G_T and G_R are the Tx and Rx antenna gain in dBi, L_T and L_R are the antenna cable losses in dB, and P_R is the local mean received power in dBm. Calculated experimental path loss samples can be used to construct a path loss model. A distance-dependent path loss model proven to perform well in indoor environments[1] is the one-slope model [6, 7]. According to the one-slope model, path loss $PL(d)$ in dB increases with distance d in m between the Tx and the Rx as:

$$PL\,(d) = PL\,(d_0) + 10n \cdot \log\,(d/d_0) \tag{2.2}$$

In (2.2), $PL(d_0)$ is the path loss in dB at an arbitrarily chosen reference distance d_0 in m, and n is the dimensionless path loss exponent. Our measurement setup exhibits a difference in height of 4 m between the Tx and the Rx. A minimum distance of 15 m is kept between both antennas to ensure that the direct ray between the Tx and the Rx is within the main lobes of both antennas in LOS situations. Path loss samples were gathered up to a distance of 140 m between the Tx and the Rx. The reference distance d_0 of the one-slope model is chosen equal to the minimum measured distance of 15 m. The parameters $PL(d_0)$ en n are obtained by fitting the one-slope model to the measured path loss samples in a Least Squares (LS) sense. Following [13], the intercept $PL(d_0)$ can be determined in two ways:

- *non-fixed intercept:* the intercept $PL(d_0)$ is considered as a separate outcome of the LS fit.
- *fixed intercept:* the intercept $PL(d_0)$ is chosen fixed and equal to the free-space path loss at reference distance d_0, i.e. $PL(d_0) = 20\log\,(4\pi d_0/\lambda)$, where λ is the wavelength in m.

The one-slope model's parameters in Section 2.4 are determined for both non-fixed and fixed intercept $PL(d_0)$. A comparison between non-fixed and fixed intercept path loss models is made to examine which approach provides a better fit to experimental data.

2.3.1.4 Shadowing

To examine shadowing characteristics of the industrial environment, deviations X_i in dB between the one-slope model with estimated parameters and the measured PL samples are determined as:

[1] Another popular indoor path loss model is the Motley-Keenan model [12]. This model takes into account additive loss terms for each penetrated wall in for example an office environment. For industrial environments however, an adjusted Motley-Keenan model where walls are replaced by machinery and storage racks does not perform well. The reason is that industrial inventory does not partition the environment in the same way that office walls do: a signal can also propagate around the industrial inventory instead of only through it. It is therefore often not realistic to assign a specific loss for propagation through industrial inventory in a path loss model.

$$X_i = PL(d_i) - PL_i \tag{2.3}$$

In (2.3), PL_i is the i-th measured path loss sample in dB taken at a distance d_i and $PL(d_i)$ is the path loss according to the one-slope model at distance d_i. It is shown that shadow fading samples X_i closely follow a lognormal distribution with median equal to 0 dB [3, 6, 7]. Shadow fading samples will be used to investigate spatial correlation properties of large-scale fading. For each measurement track separately, the normalized autocorrelation function of shadow fading samples is calculated. For a particular track, shadow fading samples X_i were calculated with respect to the one-slope model fitted to the path loss samples collected along that track. If N shadow fading samples X_1 through X_N are obtained from a measurement track, the normalized autocorrelation function $R_{XX}(m)$ associated with that track is calculated as:

$$R_{XX}(m) = \frac{\sum_{k=1}^{N-m} X_{k+m} X_k}{\sum_{l=1}^{N} X_l^2} \qquad (m = 0, \ldots, N-1) \tag{2.4}$$

As path loss samples PL_i follow from averaging received power over a 10 wavelength long window, the same also applies to shadow fading samples X_i in formula (2.3). As a consequence, $R_{XX}(m)$ in (2.4) corresponds to the normalized autocorrelation at distance m times 10 wavelengths. Per track, a decorrelation distance is calculated, which we define as the distance to which the normalized autocorrelation drops to e^{-1}. This value is commonly used, as autocorrelation can often be modeled as exponentially decaying with distance, e.g., in [14]. Large-scale fading is said to be weakly correlated at spatial separations greater than the decorrelation distance.

2.3.2 Characterization of temporal fading

2.3.2.1 Definition of temporal fading

Temporal fading is defined as the variability of received power over time at a fixed location in the propagation environment. For large-scale and small-scale fading in Section 2.3.1.1, the variability of received power is the result of the Rx seeing a different channel due to a change in the location of the Tx and/or the Rx. For temporal fading, the Rx sees a different channel even though the Tx and Rx remain fixed. The variability of received power in this case originates from movement of persons or physical objects in the environment, which alter the multipath profile.

2.3.2.2 Measurement methodology

To determine temporal fading properties of the industrial environment, the measurement cart was placed at a fixed location. To especially investigate unfavorable temporal fading situations, the measurement cart was parked in areas containing a lot of movement, such as for example at locations close to machinery and in places often frequented by fork-lift trucks. These areas exhibit worst-case temporal fading and will limit the performance of an industrial wireless communication system the most. It is therefore particularly important to determine temporal fading characteristics at these locations. At each fixed location, received power levels were recorded in a time span of 5 minutes, at a rate of approximately 8 samples per second. Consequently, a total of about 2400 samples of received power were recorded per temporal fading measurement run.

2.3.2.3 Temporal fading statistics

Per measurement run, received power levels $P_{r,i}$ ($i = 1, 2, \ldots$) in dBm were gathered at a fixed location during a time span of five minutes. The median value $P_{r,med}$ in dBm of the $P_{r,i}$ samples is subtracted, resulting in samples Y_i in dB of the received power envelope about the median:

$$Y_i = P_{r,i} - P_{r,med} \tag{2.5}$$

It is shown that the received signal envelope over time at a fixed location in the industrial environment exhibits Ricean fading properties [3]. This is validated by comparing our measured temporal fading samples Y_i to theoretical Rice distributions. In literature, Ricean fading is usually characterized by the Ricean K-factor in dB, defined as:

$$K = 10 \log \left(\frac{A^2}{2b^2} \right) \tag{2.6}$$

In (2.6), the A^2 and $2b^2$ parameters can be defined from a physical point of view [15]. The Ricean K-factor can be interpreted as the ratio of the linear power A^2 of the field established by the time-invariant part of the multipath profile to the linear power $2b^2$ of a random field component representing the other part of the multipath profile that is altered by motion. From this interpretation it follows that high K-factors point to a relatively low amount of motion in the environment, while low K-factors indicate that a rather large amount of motion disturbs the multipath profile over time. For each temporal fading measurement, the Ricean K-factor was estimated from the Y_i samples. Two distinct analytical methods were used to estimate the K-factor. These methods are:

- *Least Squares (LS) estimator:* To estimate the K-factor, the empirical Cumulative Distribution Function (CDF), i.e. Prob[$Y_i <$ abscissa]), is constructed and compared to a Rice distribution with zero median in dB using a LS fit. The theoretical Rice CDF is given by the probability Prob[$R_i < R$] that a randomly chosen sample $R_i = 10^{Y_i/20}$ is smaller than a given value R:

$$\text{Prob}\left[R_i < R\right] = \frac{1}{b^2}\int_0^R t \exp\left[\frac{-\left(t^2+A^2\right)}{2b^2}\right] \cdot I_0\left(\frac{At}{b^2}\right) \mathrm{d}t \tag{2.7}$$

  In (2.7), A and b are parameters of the Rice distribution and $I_0(.)$ is the modified Bessel function of the first kind and zeroth order. The LS fit of the empirical CDF to (2.7) results in estimates of the A and b parameters, which can subsequently be used to calculate the Ricean K-factor using (2.6). The LS method returns the Rice distribution which follows the empirical CDF the most closely. A plot of the empirical and fitted Rice CDF therefore allows one to inspect if temporal fading is Ricean.

- *Moment Based (MB) estimator:* In addition to the LS method, the Ricean K-factor was also estimated using the analytical procedure proposed in [16]. Herein, the K-factor is directly estimated from the measured Y_i samples without the need for a curve fitting operation. Let S_i correspond to the Y_i samples converted to a linear power scale, i.e., $S_i = 10^{Y_i/10}$. It is then shown that [16]:

$$A^2 = \left[\left(E\left[S_i\right]\right)^2 - Var\left[S_i\right]\right]^{1/2} \tag{2.8}$$

$$2b^2 = E\left[S_i\right] - \left[\left(E\left[S_i\right]\right)^2 - Var\left[S_i\right]\right]^{1/2} \tag{2.9}$$

  In (2.8) and (2.9), $E\left[S_i\right]$ and $Var\left[S_i\right]$ are the mean value and the variance of the S_i samples, respectively. Expressions (2.8) and (2.9) can be used to calculate the A^2 and $2b^2$ parameters in the general expression of the Ricean K-factor (formula (2.6)).

The LS and the MB estimators of the Ricean K-factor will be compared to determine how well temporal fading exhibits Ricean characteristics. This approach to confirm Ricean fading is preferred over statistical Goodness Of Fit (GOF) tests. This is because all estimations of the Ricean K-factor have to be done after converting the Y_i samples to linear values. These conversions worsen the reliability of Ricean parameter estimation [8]. This causes statistical GOF tests described in literature to fail most of the time.

2.3.3 Large-scale and temporal fading topographies

The industrial environment is categorized into different topographies to characterize large-scale and temporal fading. These topographies are defined on the basis of physical properties of the indoor industrial environment. Different topographies for large-scale and temporal fading are proposed.

2.3.3.1 Large-scale fading topographies

Large-Scale Fading (LSF) topographies are divided by whether or not LOS between the Tx and the Rx exists, and by the height of nearby industrial infrastructure relative to the height of the Tx and the Rx. LSF topography categories are specified as follows, where each category is assigned a number for further reference:

1. *LSF topography 1, Line Of Sight (LOS) path:* Paths are found along aisles surrounded by industrial machinery or warehouse storage racks. Line of sight between transmitting and receiving antenna exists at every point along the path.

2. *LSF topography 2, OBstructed line of Sight (OBS) path with light surrounding clutter:* Paths are found along aisles other than the aisle where the Tx is located. Line of sight between the Tx and the Rx is blocked by industrial inventory at the same height as or slightly higher than the Rx, but well below the Tx.

3. *LSF topography 3, OBstructed line of Sight (OBS) path with heavy surrounding clutter:* Paths are found along aisles where LOS between the Tx and the Rx is blocked by industrial inventory at about the same height as or higher than the Tx and well above the Rx.

The above definitions of the various LSF topographies are largely based on the classification made in [3]. The height of the industrial inventory relative to the Tx and the Rx is not considered in LOS circumstances in our definitions. As can be derived from the results reported in [3], inventory height has little effect on the large-scale fading in LOS situations. Fig. 2.5 shows two industrial surroundings that can be categorized under LSF topographies 2 and 3: Fig. 2.5(a) shows an environment with light clutter comparable in height to that of the Rx, while Fig. 2.5(b) shows a warehouse with heavy surrounding clutter almost reaching the ceiling.

2.3.3.2 Temporal fading topographies

Temporal Fading (TF) topographies are defined differently compared to LSF topographies. It is clear that temporal fading behavior is not determined by stationary physical characteristics of the environment such as LOS/OBS or inventory height.

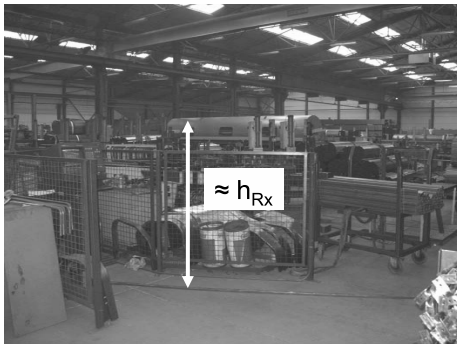

(a) LSF topography 2, light surrounding clutter

(b) LSF topography 3, heavy surrounding clutter

Figure 2.5: LSF topographies 2 and 3

Temporal variations are rather caused by movement of persons and machinery perturbing the multipath signal at the receiver location. Thus, temporal fading will be dictated by the degree of movement in the industrial environment, which is linked to the sort of industrial activity that takes place. In this respect, four TF topography categories are defined as follows:

1. *TF topography 1, automated production line:* Human interaction with the production process is very limited. The environment is nearly static except for movement induced by machinery.

2. *TF topography 2, partially automated production line:* Human interaction is more present in this environment. Workers move in the production space to operate and keep supervision of the partially automated machines. Fork-lift trucks frequent the production space to transport raw materials and finished products. The machines themselves also contribute to the total amount of movement found in this topography.

3. *TF topography 3, manual production line:* The quantity of automated machinery is far less than in TF topographies 1 and 2. Movement is primarily caused by workers who perform tasks at individual workbenches using small, manually served machines. Compared to TF topographies 1 and 2, the occupation of workplaces with industrial machinery is clearly more dense and the workplace is thus less open in TF topography 3. Due to the manual nature of the assembly process, workplaces in TF topography 3 contain the largest number of workers of all TF topographies.

4. *TF topography 4, warehouse:* The type of movement in warehouses consists almost exclusively of fork-lift truck traffic. Warehouses are spacious with storage racks placed far enough in between to allow easy passing of the trucks.

Fig. 2.6 shows pictures of industrial surroundings categorized under TF topographies 1 through 4.

(a) TF topography 1 (b) TF topography 2

(c) TF topography 3 (d) TF topography 4

Figure 2.6: TF topographies 1 through 4

2.4 Large-scale fading results

In the following, results of the path loss measurements are discussed. A total of 956 path loss samples at 900 MHz, 2328 samples at 2400 MHz, and 3096 samples at 5200 MHz were used in the calculation of the parameters of the one-slope model. For each frequency, measurements were performed at distances between transmitter and receiver from 15 m to 140 m. Maximum measured path losses of 98 dB, 105 dB, and 96 dB were found at the center frequencies of 900 MHz, 2400 MHz, and 5200 MHz, respectively. Maximum path losses were found farthest from the Tx, in heavy surrounding clutter situations (i.e., in LSF topography 3).

Section 2.4 is organized as follows. For each center frequency separately, the one-slope model's parameters are determined per LSF topography and per factory building in Sections 2.4.1 and 2.4.2, respectively. The dependence of the one-slope model's parameters on LSF topography and measured factory building is discussed. In Section 2.4.3, the autocorrelation properties per measurement track of shadow fading samples are determined.

2.4.1 Path loss per LSF topography

Path loss samples calculated with the link budget in formula (2.1) are subdivided according to transmitted frequency and LSF topography (see Section 2.3.3). The parameters of the one-slope model in formula (2.2) are determined separately for each frequency and LSF topography. Table 2.1 shows the path loss $PL(d_0)$ at reference distance d_0 = 15 m and the path loss exponent n of the one-slope model, as well as the standard deviation σ in dB of the X_i samples calculated with formula (2.3). Path loss models at the different investigated frequencies are provided for each LSF topography separately and for all path loss data regardless of LSF topography in bold font. Distinction has been made between one-slope models with non-fixed and fixed intercept $PL(d_0)$.

2.4.1.1 Comparison between non-fixed and fixed intercept models

Our analysis indicates that the use of a path loss model with non-fixed intercept is preferred to using a fixed-intercept model. The following discussion argues as to why our preference goes out to a non-fixed intercept one-slope model.

Firstly, it is noteworthy that the difference in $PL(d_0)$ between the non-fixed intercept and the fixed intercept models in Table 2.1 can occasionally be as high as 17 dB. Therefore, free-space propagation at reference distance d_0 (assumed for fixed intercept models) can hardly be assumed for our measurements. This could be attributed to the height difference between the Tx and the Rx in our

Frequency [MHz]	LSF topography	Non-fixed intercept			Fixed intercept		
		$PL(d_0)$ [dB]	n [-]	σ [dB]	$PL(d_0)$ [dB]	n [-]	σ [dB]
900	1	57.67	2.25	5.65	55.05	2.68	5.74
	2	64.42	1.94	4.97	55.05	3.24	5.62
	3	69.73	2.16	5.16	55.05	4.47	6.86
	All	**61.65**	**2.49**	**7.35**	**55.05**	**3.51**	**7.70**
2400	1	67.43	1.72	4.73	63.57	2.40	4.97
	2	72.71	1.52	4.61	63.57	2.77	5.42
	3	80.48	1.69	6.62	63.57	4.29	8.42
	All	**71.84**	**2.16**	**8.13**	**63.57**	**3.44**	**8.63**
5200	1	77.57	1.25	4.32	70.28	2.47	5.19
	2	81.06	0.68	3.87	70.28	2.18	4.93
	3	83.33	1.35	3.16	70.28	3.70	5.15
	All	**81.01**	**0.91**	**4.79**	**70.28**	**2.59**	**6.09**

Table 2.1: Parameters of non-fixed and fixed intercept one-slope models (d_0 = 15 m) for each LSF topography and frequency

measurement configuration. free-space propagation can usually only be assumed in spacious areas free of immediate obstructions, in contrast to our measurement configuration where the Tx is raised practically to rooftop level.

Secondly, it is generally accepted in literature that shadow fading samples X_i are lognormally distributed. To ascertain lognormality, a Kolmogorov-Smirnov (KS) GOF test was performed on the shadow fading samples of the one-slope models provided in Table 2.1. For the KS test, the empirical CDF of shadow fading samples was compared to a lognormal CDF with zero median in dB and standard deviation σ of the corresponding model. For three frequencies and three LSF topographies in Table 2.1, the non-fixed intercept one-slope models passed the KS test at $\alpha = 0.05$ level of significance, whereas only two out of nine fixed intercept models passed the same test. This indicates that median path loss is most accurately specified by a path loss model with non-fixed intercept. Moreover, standard deviations σ in Table 2.1 are somewhat smaller for non-fixed intercept in comparison with fixed intercept, showing that a non-fixed intercept one-slope model provides a better fit to experimental path loss data.

2.4.1.2 Discussion of non-fixed intercept models

Fig. 2.7(a) shows the measured path loss samples and the fitted one-slope model with non-fixed intercept for each LSF topography at 900 MHz (black: LSF topography 1, blue: LSF topography 2, red: LSF topography 3). Also shown is the free-space path loss at 900 MHz (gray). As can be seen in Fig. 2.7(a), the median path loss as predicted by the one-slope model with non-fixed intercept is higher

than the free-space path loss for all LSF topographies. Moreover, median path loss is higher in LSF topographies with a higher serial number. These remarks are also valid for the measurements performed at 2400 and 5200 MHz (Figs. 2.7(b) and 2.7(c)).

In the following, a comparison across the different frequencies and LSF topographies regarding the value of the parameters $PL(d_0)$, n, and σ is made for the non-fixed intercept path loss models in Table 2.1.

The intercept $PL(d_0)$

Frequency dependence: For a given LSF topography, the value of $PL(d_0)$ in Table 2.1 increases with increasing frequency. As can be expected, path loss is generally larger at higher frequencies.

LSF topography dependence: For a given frequency, $PL(d_0)$ increases with the assigned number of the LSF topography. This tendency satisfies our expectations: for the various LSF topographies of Section 2.3.3, the paths between the Tx and Rx become more obstructed by the industrial infrastructure in LSF topographies with a higher serial number. Obviously, higher path loss is expected for more obstructed paths.

The path loss exponent n

Frequency dependence: For each LSF topography considered separately, one notices a decrease in n with increasing frequency. At 2400 and 5200 MHz, the path loss exponent n is lower than 2, the path loss exponent in free space. Path loss exponents lower than 2 have also been found in [3], showing that heavy multipath propagation is certainly present in industrial environments. The dependence of the path loss exponent on frequency can be clarified by considering the physical construction of industrial workplaces and warehouses. The industrial machinery and storage racks are not randomly placed throughout the workplace. Instead, industrial infrastructure is clustered around aisles, which are frequented by workers and fork-lift trucks. Electromagnetic energy is channelled along these aisles by reflections off the surrounding machinery. Furthermore, multipath propagation is facilitated by the abundance of highly reflective metal inventory present in industrial environments.

Path loss exponents lower than 2 have also been found for measurements conducted in office buildings [17, 18]. Office environments are distinctly partitioned, where the channeling of electromagnetic energy occurs along walkways delimited by office walls. No clear relationship between path loss exponent and frequency

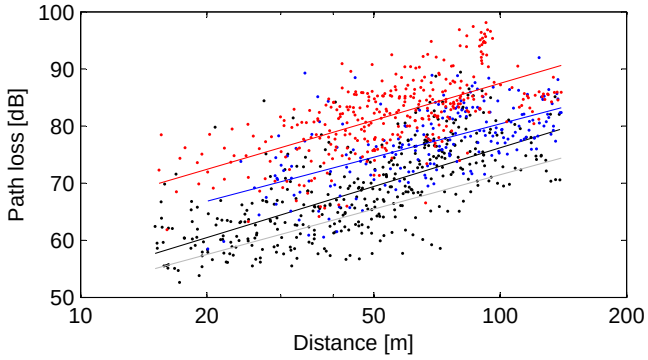

(a) 900 MHz

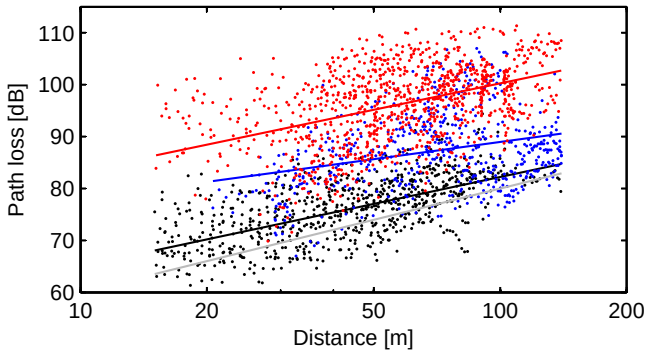

(b) 2400 MHz

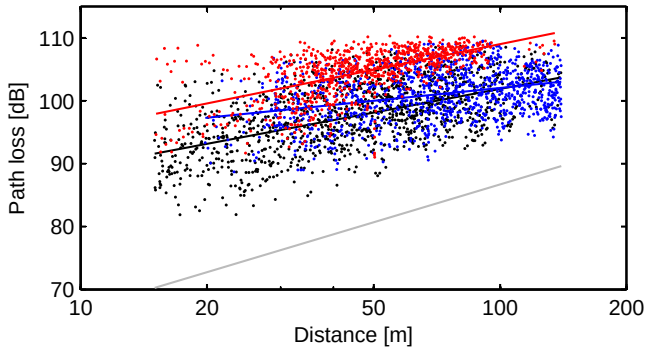

(c) 5200 MHz

Figure 2.7: Path loss for the different frequencies (black: LSF topography 1, blue: LSF topography 2, red: LSF topography 3, gray: free space)

has however been established for these environments. In contrast to office buildings, structures flanking walkways are far less smooth in industrial environments. In industrial environments, these structures consist mostly of irregularly shaped machine parts instead of flat walls. At higher frequencies, as the wavelength shortens, more of the smaller machine parts can act as good reflectors of electromagnetic energy. This increases the number of reflections in the multipath profile, causing the increase of path loss with distance to be less steep. This is a possible explanation for the decrease of the path loss exponent n with frequency found in Table 2.1 for the non-fixed intercept path loss models.

LSF topography dependence: For each frequency considered separately, a similar path loss exponent n is found for LSF topography 1 (LOS) and LSF topography 3 (OBS, heavy clutter) in Table 2.1. The absolute difference in the value of n between these two LSF topographies is maximally 0.1. Furthermore, the path loss exponent n is clearly lower in LSF topography 2 (OBS, light clutter) in comparison with the other topographies. In the following, an explanation for these observations starting from the layout of the industrial aisles in the different LSF topographies is proposed.

In the event that the Rx is located in an aisle situated in LSF topography 3, at least one side of the aisle with industrial inventory obstructs LOS between the Tx and the Rx, as shown in Fig. 2.8(a). Transmission of electromagnetic energy through this side of the aisle is assumed to be negligible, as industrial inventory consists mostly of highly reflective metal machine parts. In addition, contributions to the received power of waves diffracting over the top of the industrial inventory are negligible, because the height h of the industrial infrastructure in LSF topography 3 is greater than the height of both the Tx and the Rx, and approximately reaches ceiling height. The transmitted energy can only be caught into the LSF topography 3 aisle through several reflections at the industrial inventory and diffractions at the vertical edge of the aisle's flank (shown in Fig. 2.8(a)). This process involves a certain amount of reflection and diffraction loss, resulting in a higher value of the $PL(d_0)$ parameter in LSF topography 3 in comparison with LSF topography 1. Once a part of the transmitted energy is caught into the aisle in LSF topography 3, further wave propagation is expected to be similar to propagation in LSF topography 1, i.e., by reflections at the floor, the ceiling and the aisle's flanks. This implies that the increase in path loss with distance will be comparable in these two LSF topographies, resulting in nearly equal values of the path loss exponent n.

Propagation in LSF topography 2 is assumed to occur partly in a similar way as in LSF topography 3, i.e., by capturing part of the transmitted energy at the start of an aisle, from where it is further channelled along the aisle (see Fig. 2.8(b)). However, because the height h of the industrial inventory is lower than the height

of the Tx and comparable to the height of the Rx in LSF topography 2, contributions to the received power by diffraction over the top of the aisle's sides cannot be neglected, in contrast to the situation in LSF topography 3. Fig. 2.8(b) shows a ray path undergoing one diffraction over a top horizontal edge of the industrial inventory. This ray path will contribute considerably to the received power as it is the shortest possible ray path between the Tx and the Rx. The ray path is less diffracted when the Rx moves further away from the Tx in the LSF topography 2 aisle, which means that a smaller diffraction loss in addition to the free-space loss is associated with the path as distance increases. As a consequence, path loss does not increase as fast with distance as in LSF topographies 1 and 3, resulting in a lower value of the path loss exponent n in Table 2.1.

The standard deviation σ

Frequency dependence: For the non-fixed intercept one-slope models in Table 2.1, the standard deviation σ associated with shadow fading shows no clear dependence of the frequency.

LSF topography dependence: The standard deviation does not seem to be consistently higher or lower for a certain LSF topography.

2.4.1.3 Comparison with existing models

In both [3] and [4], industrial path loss data has been fitted to a one-slope model with fixed intercept $PL(d_0)$. To compare our path loss results with these existing models in a correct manner, discussion will be limited to the fixed intercept one-slope models shown in Table 2.1.

In [3], large-scale fading measurements at 1300 MHz revealed path loss exponents n of 1.79, 2.38, and 2.81 for LSF topographies 1 through 3, and $n = 2.18$ for all path loss data regardless of LSF topography. From Table 2.1, consistently higher path loss exponents ranging between 2.18 and 4.47 for all center frequencies are obtained. The increase in path loss exponent for our measurements can be explained from the height difference of 4 m between the Tx and the Rx, whereas [3] reports the Tx and the Rx both installed at 2 m above ground level. Because of the height difference, propagation from the Tx to the Rx occurs downwards, meaning overall higher path losses are to be expected for our measurement configuration. Additionally, the Tx at 6 m height will generally be further away from industrial inventory compared to [3], where the Tx is placed in aisles flanked by machinery. This limits the number of possible multipath reflections in our case and increases the path loss exponent. The same analysis can be repeated for measurements at

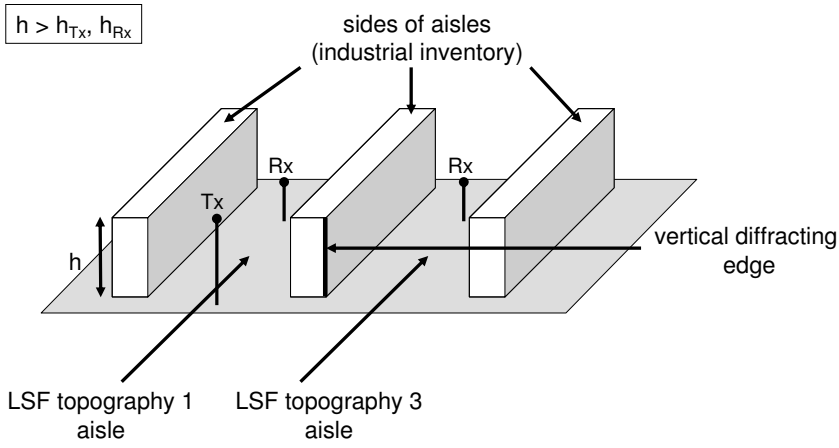

(a) LSF topographies 1 and 3

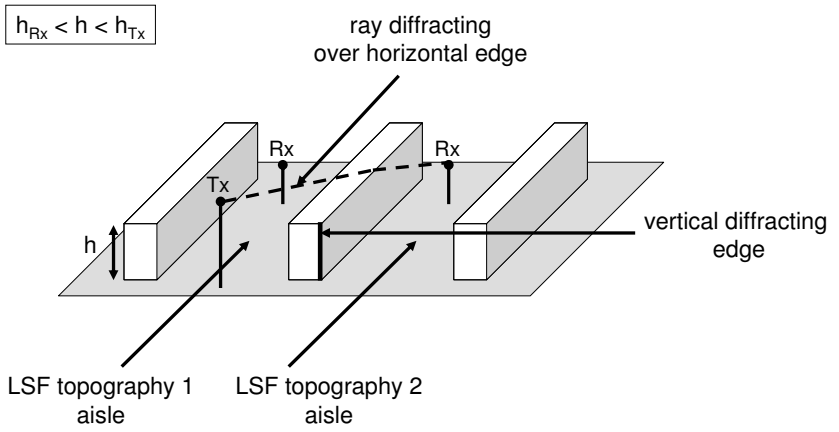

(b) LSF topographies 1 and 2

Figure 2.8: Different industrial aisle layouts

2450 MHz in [4], where antennas close to ground level yielded low path loss exponents between 1.10 and 1.86 in LOS circumstances. Measurements in office corridors gave low path loss exponents for fixed intercept one-slope models between 0.44 and 2.60, for LOS and OBS topographies at several center frequencies between 450 MHz and 24 GHz [17, 18]. In contrast to industrial aisles where our measurements took place, office corridors are more clearly delimited by objects such as walls, floors and ceilings. Office corridors are therefore expected to channel electromagnetic energy more efficiently, resulting in lower path loss exponents

in comparison with our measurements.

In [3], standard deviations σ of 4.42, 4.67, and 8.09 dB are found for LSF topographies 1 through 3, and $\sigma = 7.92$ dB for all LSF topographies considered together. These standard deviations are similar to those in Table 2.1 between 4.93 and 8.63 dB, which implies the same degree of shadow fading as in [3] is found in our measurements.

2.4.2 Path loss per building

The building-to-building path loss variations are shown in Table 2.2. The one-slope model's parameters are given for each measured facility separately, for both non-fixed and fixed intercept models. Additionally in Table 2.2, we discriminated between frequencies but not between specific LSF topographies. The buildings for which the path loss models are determined, are specified by an acronym. As mentioned in Section 2.2.2, measurements were carried out in two wood processing facilities, which have been noted as WP I and WP II in Table 2.2, and two metal processing facilities, which have been noted as MP I and MP II. Furthermore, we provided the one-slope model's parameters for all the data of the two wood processing facilities together (WP in bold font in Table 2.2) and also for the two metal processing facilities together (MP in bold font in Table 2.2).

As can be seen in Table 2.2, the intercept $PL(d_0)$ is consistently larger for the non-fixed intercept model in comparison with the fixed intercept model. Also, smaller path loss exponents n are obtained with the non-fixed intercept model in comparison with the fixed intercept model. Standard deviations σ for non-fixed intercept and fixed intercept match well, although they are consistently somewhat larger for the fixed intercept models. Another tendency present in Table 2.2 is the decrease in path loss exponent with increasing frequency, for both non-fixed and fixed intercept. This tendency was previously detected in Table 2.1 for non-fixed intercept models, and a physical explanation for this was already given in Section 2.4.1.2.

For each frequency considered separately, Table 2.2 shows that the non-fixed intercept $PL(d_0)$ differs maximally about 2 dB between the WP and MP facilities. Path loss exponents n are found to be consistently somewhat higher for the MP facilities in comparison with the WP facilities, probably because the industrial infrastructure was more dense in the MP facilities. Overall, building-to-building variation is limited, mainly because construction details of all measured facilities are similar (concrete floors and walls, metal ceilings). Additionally, industrial inventory in all facilities consists for the largest part of similar metal machinery. Measurements in [3] at 1300 MHz in five different industrial facilities also showed fairly limited building-to-building variation. The path loss exponents n for fixed intercept one-slope models varied only from 1.89 to 2.43 between different facto-

Frequency [MHz]	Facility	Non-fixed intercept			Fixed intercept		
		$PL(d_0)$ [dB]	n [-]	σ [dB]	$PL(d_0)$ [dB]	n [-]	σ [dB]
900	WP I	61.89	2.40	7.04	55.05	3.50	7.45
	WP II	64.52	1.57	8.38	55.05	3.13	9.16
	WP	**62.65**	**2.18**	**7.51**	**55.05**	**3.41**	**8.01**
	MP I	53.54	4.74	7.90	55.05	4.49	7.91
	MP II	60.06	2.40	4.71	55.05	3.07	5.00
	MP	**60.51**	**2.79**	**7.57**	**55.05**	**3.58**	**7.79**
2400	WP I	70.10	1.53	5.10	63.57	2.56	5.61
	WP II	67.14	1.63	4.28	63.57	2.52	4.52
	WP	**69.66**	**1.58**	**5.09**	**63.57**	**2.56**	**5.56**
	MP I	65.70	3.90	8.09	63.57	4.24	8.11
	MP II	64.72	2.48	5.36	63.57	2.63	5.38
	MP	**68.75**	**2.51**	**8.30**	**63.57**	**3.26**	**8.46**
5200	WP I	74.98	0.87	3.58	70.28	1.68	4.05
	WP II	79.76	0.79	4.75	70.28	2.34	6.14
	WP	**77.02**	**0.86**	**4.70**	**70.28**	**1.99**	**5.44**
	MP I	77.49	1.65	4.03	70.28	2.96	4.60
	MP II	75.17	1.21	4.09	70.28	1.88	4.42
	MP	**77.62**	**1.04**	**4.59**	**70.28**	**2.12**	**5.24**

Table 2.2: Parameters of non-fixed and fixed intercept one-slope models (d_0 = 15 m) for each facility and frequency

ries.

2.4.3 Shadowing

Spatial correlation characteristics of shadow fading are investigated by means of calculating the normalized autocorrelation function. To this end, one-slope models were fitted to the path loss data of each measurement track separately. A non-fixed intercept $PL(d_0)$ was used in the determination of the one-slope models' parameters. As stated in Section 2.4.1.1, the model with non-fixed intercept provides a more accurate representation of median path loss. Shadow fading samples X_i of formula (2.3) were calculated relative to the one-slope model associated with each measurement track. Following, the normalized autocorrelation function $R_{XX}\,(m)$ was calculated using formula (2.4).

An example of the normalized autocorrelation versus distance for a measurement track at 900 MHz is shown in Fig. 2.9. In Fig. 2.9, one notices a rapid decrease in autocorrelation with distance. This reinforces the popular assertion that shadow fading autocorrelation decays exponentially with distance, as reported in e.g., [14]. Decorrelation distances, as defined in Section 2.3.1.4, were calculated

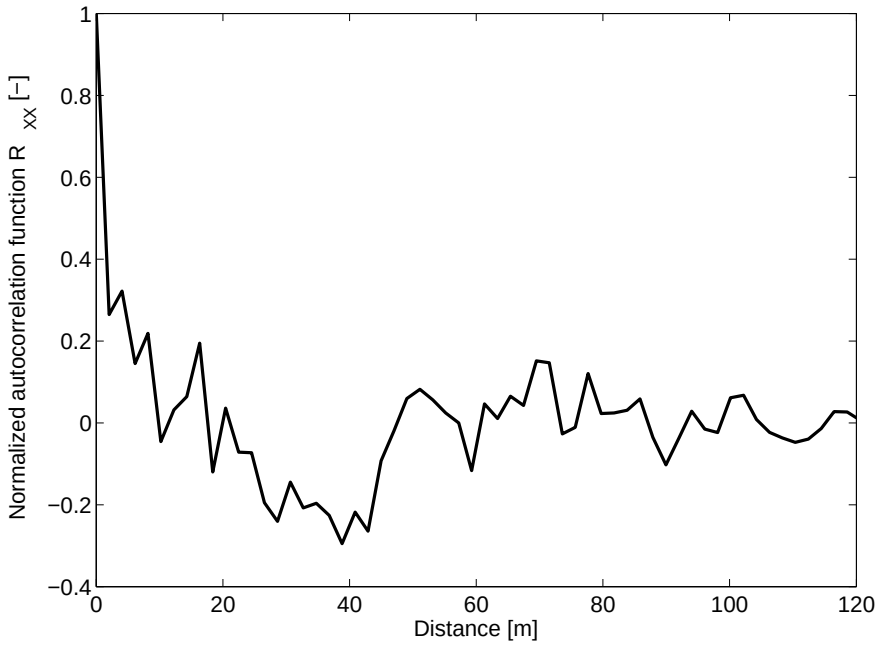

Figure 2.9: Normalized autocorrelation R_{XX} of shadow fading samples versus distance for a measurement track at 900 MHz

for each measurement track individually. Decorrelation distances varied between 0.2 and 5.3 m for all frequencies and LSF topographies. These are comparable with decorrelation distances in the order of 1 to 2 m reported in [14] for indoor measurements at 1800 and 5200 MHz. It can be stated that shadow fading is weakly correlated, even over small distances.

2.5 Temporal fading results

In this section, results of temporal fading measurements are discussed. For each TF topography and each analyzed frequency, 2 to 6 temporal fading measurements of 5 minutes were recorded during the measurement campaign in the 4 factories. Fig. 2.10 shows a typical temporal fading measurement of received power in dBm over time in s, executed in TF topography 1 (automated production line) at 900 MHz.

Section 2.5.1 discusses the statistics of the measured Ricean K-factors and validates that industrial temporal fading is Ricean. Section 2.5.2 compares values of the K-factors across the different TF topographies and explains them from the

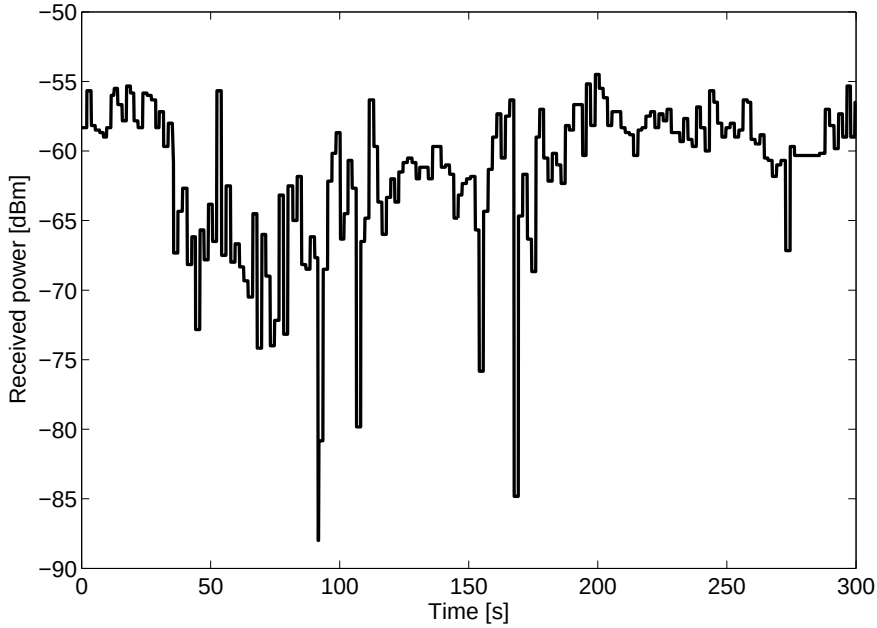

Figure 2.10: Temporal fading measurement in TF topography 1 at 900 MHz

physical construction of the TF topographies.

2.5.1 Statistics of K-factors and validation

Table 2.3 shows the mean value of all K-factors collected in a particular TF topography for the three center frequencies of 900, 2400, and 5200 MHz. Also shown in bold font are the mean K-factors for each center frequency without making any discrimination between TF topographies. For each temporal fading measurement, the Ricean K-factor was calculated both as a Least Squares (LS) and Moment Based (MB) estimation (see Section 2.3.2.3). Table 2.3 distinguishes between mean values based on LS and MB estimators of the Ricean K-factors. Very good agreement between the LS and MB estimators of the Ricean K-factors was established. For all temporal fading measurements, both estimators deviated on average only 1 dB.

For each TF topography considered separately, mean K-factors do not exhibit a strong dependence on frequency. Therefore, K-factors averaged over all frequencies are also shown in Table 2.3. In the design and simulation of an industrial wireless communication system, it is also important to have an idea about the worst-case K-factor which could manifest itself. Therefore, also the 10th percentiles of both types of K-factor estimators are brought in Table 2.3 for all of the

TF topography	Estimator	Mean K [dB] 900 MHz	2400 MHz	5200 MHz	All frequencies	10th perc. of K [dB] All frequencies
1	LS	17.8	18.6	16.2	17.5	15.5
	MB	18.4	17.6	15.7	17.0	15.2
2	LS	13.3	12.4	14.9	13.5	7.8
	MB	12.9	12.9	14.7	13.5	8.3
3	LS	3.5	5.3	6.5	5.1	2.4
	MB	3.5	5.7	6.1	5.1	2.8
4	LS	16.3	12.0	16.6	15.4	6.9
	MB	13.5	11.1	16.0	13.5	6.7
All	**LS**	**12.4**	**11.7**	**14.1**	**12.8**	**5.0**
	MB	**11.5**	**11.6**	**13.7**	**12.3**	**5.1**

Table 2.3: Statistics of the estimators of the Ricean K-factors per TF topography and frequency

TF topographies.

Fig. 2.11 shows the empirical CDF of the Y_i samples (formula (2.5)) of three temporal fading measurement sets taken in production TF topographies 1 to 3 at 900 MHz. Also shown are the Rice CDFs fitted using the LS procedure described in Section 2.3.2.3. The resulting LS estimators of the Ricean K-factors for the three fading measurements are shown. Fig. 2.11 shows that temporal fading statistics are excellently described by a Rice distribution. From the good agreement between both types of estimators of the Ricean K-factor together with the good correspondence between empirical and fitted Rice CDFs in Fig. 2.11, we can conclude that industrial temporal fading is Ricean.

Fig. 2.12 shows a CDF of all Ricean K-factors, regardless of TF topography or measurement frequency. The CDF was constructed on the basis of the MB estimators of the Ricean K-factor and comprises a total of 49 temporal fading measurement runs. The 10th percentile of K-factors in Fig. 2.12 is 5.1 dB. The mean value and standard deviation of the K-factors in Fig. 2.12 are 12.3 dB and 5.4 dB, respectively. A KS GOF test showed that the null hypothesis that the K-factors in Fig. 2.12 are lognormally distributed with mean 12.3 dB and standard deviation 5.4 dB, could not be rejected at significance level $\alpha = 0.05$. This lognormal CDF is also shown in Fig. 2.12. An overall mean K-factor of approximately 12 dB is in good agreement with temporal fading measurements performed in [3], where Ricean fading was established having a K-factor of 10 dB.

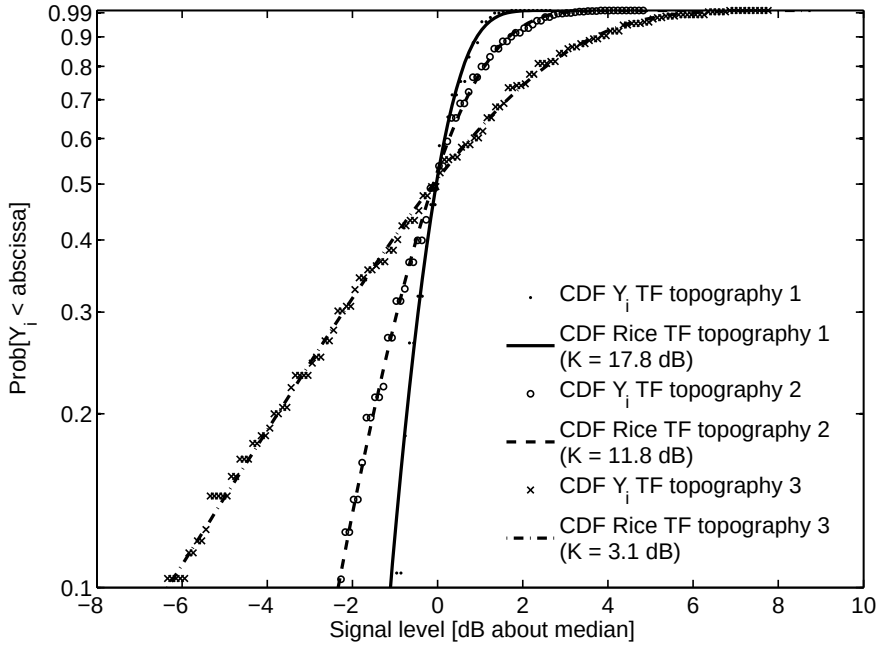

Figure 2.11: CDF deviations Y_i [dB] and fitted Rice CDF for three measurement sets in TF topography 1 to 3 at 900 MHz

2.5.2 Comparison of K-factors and physical interpretation

The mean K-factors in Table 2.3 are relatively high and vary from 4 dB to 19 dB. In office environments, substantially lower K-factors from -12 dB to -6 dB are reported in [15]. The high K-factors in industrial environments compared to office environments can be explained as follows. The open nature of industrial building layouts along with the presence of highly reflective materials such as metal generally give rise to a great number of rays in the multipath profile associated with the Rx. It is therefore expected that only a relatively small part of the multipath profile will be perturbed by motion, leaving the majority of transmitted rays to be invariant with time. In contrast, office buildings are partitioned into several floors and a number of rooms per floor. This partitioning greatly limits the number of rays in the multipath profile between the Tx and the Rx. Perturbation by motion of this small number of ray paths will therefore more likely deliver considerable fluctuations of received power over time. This not only signifies a lower dynamic range of received power over time in industrial environments compared to office environments, as noted in [3], but also means higher K-factors are to be expected in industrial environments.

The values of the K-factors in Table 2.3 are primarily determined by the type

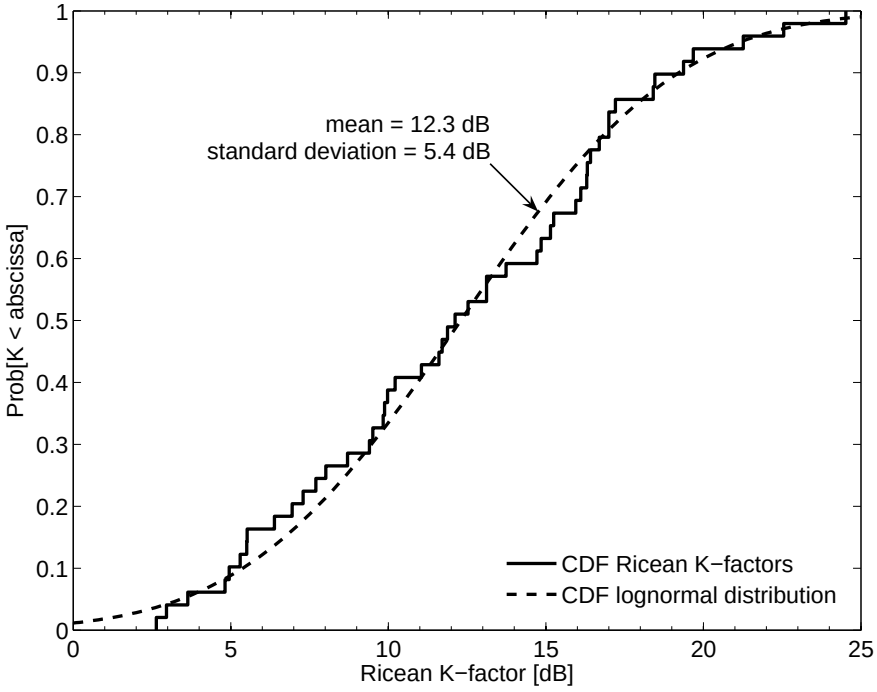

Figure 2.12: CDF Ricean K-factors for all TF topographies and all frequencies (MB estimators)

of TF topography. Automated production lines (TF topography 1) exhibit the overall highest K-factors, due to the lowest presence of motion in these environments. The lowest K-factors are found in manual production lines (TF topography 3). As production processes are found to be less automated, workplaces tend to become more densely filled with smaller industrial machinery. Aisles are also more narrow in manual production lines in comparison with more automated production lines, causing electromagnetic waves propagating along these aisles to be more easily disturbed by passing traffic. Furthermore, manual production lines are often more populated with workers, rising the amount of motion in the surroundings. This analysis explains the decrease in K-factor in Table 2.3 as production lines become less automated. High K-factors are also found in warehouses (TF topography 4). Aisles in warehouses are fairly wide to allow easy passing of fork-lift trucks. Moreover, fork-lift truck traffic was found to be rather low in the warehouses: more than two fork-lift trucks being simultaneously present in the vicinity of the Tx and Rx occurred only rarely.

2.6 Conclusions

In this chapter, measurements of large-scale fading and temporal fading in industrial environments have been presented. Measurements were performed at 900, 2400, and 5200 MHz. These are frequencies recently targeted by a number of wireless communication standards for industrial communication. Transmitting and receiving antenna heights were chosen equal to 6 m respectively 2 m, to imitate practical placement of industrial wireless access points and terminals. Large-scale and temporal fading characteristics were determined for a number of newly proposed industrial topographies.

Large-scale fading was found to be excellently described by a one-slope path loss model and to agree well with lognormal fading statistics. It was found that median path loss is most accurately expressed by a one-slope model with non-fixed intercept path loss, which was attributed to the choice of a transmitting antenna installed approximately at rooftop level. A physical model explaining the dependency on topography and frequency of the one-slope model's parameters was presented. Herein, a key finding was that the path loss exponent appears to decrease with increasing frequency. Path loss variations between measured factory buildings were found to be limited, mainly because of their similar constructional details. Overall, path loss was somewhat larger compared to industrial measurements reported in literature, which has been explained by the height difference between the Tx and the Rx in our measurements.

Temporal fading was found to correspond excellently to Ricean distributions. A physical model explaining the values of the Ricean K-factors across different temporal fading topographies was given. Temporal fading was found to be most significant in manual production lines and to be overall less important than in office environments. Temporal fading was found to be only weakly dependent on frequency. Measured Ricean K-factors are found to follow a lognormal distribution with mean 12.3 dB and standard deviation 5.4 dB.

References

[1] IEEE Standards Association. *Wireless LAN Medium Access Control (MAC) and Physical Layer (PHY) Specifications*. ANSI/IEEE Std 802.11, 1999.

[2] ZigBee Alliance. *ZigBee Specification v1.0*. ZigBee Document 053 473r00, 2005.

[3] T. S. Rappaport and C. D. McGillem. *UHF Fading in Factories*. IEEE Journal on Selected Areas in Communications, 7(1):40–48, January 1989.

[4] S. Kjesbu and T. Brunsvik. *Radiowave Propagation in Industrial Environments*. 26th Annual Conference of the IEEE Industrial Electronics Society, 4:2425–2430, October 2000.

[5] W. Joseph, C. Olivier, and L. Martens. *A Robust, Fast and Accurate Deconvolution Algorithm for EM-field Measurements Around GSM and UMTS Base Stations With a Spectrum Analyser*. IEEE Transactions on Instrumentation and Measurement, 51(6):1163–1169, December 2002.

[6] S. R. Saunders. *Antennas and Propagation for Wireless Communication Systems*. Wiley and Sons, 1999.

[7] T. S. Rappaport. *Wireless Communications, Principles and Practice*. Prentice Hall PTR, second edition, 2002.

[8] K. Pahlavan and A. H. Levesque. *Wireless Information Networks*. Wiley and Sons, second edition, 2005.

[9] H. Hashemi. *The Indoor Radio Propagation Channel*. Proceedings of the IEEE, 81(7):943–968, July 1993.

[10] R. A. Valenzuela, O. Landron, and D. L. Jacobs. *Estimating Local Mean Signal Strength of Indoor Multipath Propagation*. IEEE Transactions on Vehicular Technology, 46(1):203–212, February 1997.

[11] W. C. Y. Lee. *Estimate of Local Average Power of a Mobile Radio Signal*. IEEE Transactions on Vehicular Technology, 34(1):22–27, February 1985.

[12] J. M. Keenan and A. J. Motley. *Radio Coverage in Buildings*. British Telecom Technology Journal, 8(1):19–24, January 1990.

[13] V. Erceg, L. J. Greenstein, S. Y. Tjandra, S. R. Parkoff, A. Gupta, B. Kulic, A. A. Julius, and R. Bianchi. *An Empirically Based Path Loss Model for Wireless Channels in Suburban Environments*. IEEE Journal on Selected Areas in Communications, 17(7):1205–1211, July 1999.

[14] N. Jaldén, P. Zetterberg, B. Ottersten, A. Hong, and R. Thomä. *Correlation properties of large scale fading based on indoor measurements*. IEEE Wireless Communications and Networking Conference, pages 1894–1899, March 2007.

[15] R. J. C. Bultitude. *Measurement, Characterisation and Modeling of Indoor 800/900 MHz Radio Channels for Digital Communications*. IEEE Communications Magazine, 25(6):5–12, June 1987.

[16] L. J. Greenstein, D. G. Michelson, and V. Erceg. *Moment-Method Estimation of the Ricean K-factor*. IEEE Communications Letters, 3(6):175–176, June 1999.

[17] A. Chandra, A. Kumar, and P. Chandra. *Comparative Study of Path Losses from Propagation Measurements at 450 MHz, 900 MHz, 1.35 GHz and 1.89 GHz in the Corridors of a Multifloor Labaratory-cum-Office Building*. IEEE Vehicular Technology Conference, 4:2272–2276, September 1999.

[18] D. Lu and D. Rutledge. *Investigation of Indoor Radio Channels from 2.4 GHz to 24 GHz*. IEEE Antennas and Propagation Society International Symposium, 2:134–137, June 2003.

3

Validation of fading models in industrial environments

3.1 Introduction

In this chapter, it is investigated whether an industrial propagation model can predict the performance of an off-the-shelf wireless communication system implementing the IEEE 802.11b/g specification [1]. To this end, extensive site survey measurements of an 802.11b/g system were carried out in various factory environments. To our knowledge, no work has been done to compare the results of a site survey to an industrial propagation model. For office environments however, limited literature exists that discusses site survey measurements of data throughput and throughput prediction based on path loss models for these environments [2, 3]. A comparison between a propagation model and a site survey is valuable as it increases the overall usefulness of the propagation model. If the agreement is adequate, the propagation model can be rightfully used for indoor site planning, thus reducing further need for time-consuming site surveys in each factory environment where a wireless network is to be deployed. Additionally, this comparison can help to identify situations wherein the propagation model does not provide a good estimate of the true wireless range. For these specific situations, the deviation between propagation model and site survey can then be explained from the physical structure of the environment.

For this research, the empirical range of a wireless Access Point (AP) is extracted from the site survey measurement data. Then, the empirical range is com-

pared to a theoretical range based on the propagation model and the configurational parameters of the site survey equipment. This theoretical range is determined through the calculation of a link budget, which is based on the industrial propagation models in chapter 2. Judicious choices for the parameters constituting this link budget will be made. Furthermore, differences in empirical and theoretical ranges are discussed and explained from the physical layout of the measured industrial rooms. This will result in some rules of thumb for choosing an optimal location for industrial APs, i.e., to cover a given area with as few APs as possible. Practically, the industrial propagation model could then be integrated in software tools for coverage planning, which also take into consideration and correct for circumstances wherein the agreement between model and site survey measurements is less satisfactory.

The outline of this chapter is as follows. In Section 3.2, the measurement configuration for the site surveys is explained. In Section 3.3, a link budget is calculated to theoretically determine the wireless range of the site survey measurement configuration for different industrial environments and data rates. A framework for extraction of the range from the site survey data is presented in Section 3.4. Then, in Section 3.5, the wireless range according to the theoretical link budget is validated by the empirical site surveys. Finally, conclusions are drawn in Section 3.6.

3.2 Measurement configuration

3.2.1 Measurement locations

Site survey measurements were conducted in two industrial facilities (one wood processing and one metal processing factory) located in Flanders, Belgium. For the two facilities together, site survey measurements were conducted in three production rooms (labeled for further reference as 'production I', 'production II', and 'production III') and one warehouse (labeled as 'warehouse'). In each of these four rooms, a site survey was executed for two different locations of the AP. The measured factory buildings exhibit similar physical properties: buildings have concrete floors and metal ceilings supported by steel truss work. At the two factories, building walls are made of thick, precast concrete. The height of each building is approximately 7 to 8 m. Industrial inventory in the facilities is for the largest part made of metal. In the warehouse at the wood processing factory, wood is the predominant material. Fig. 3.1 shows pictures of the four measured industrial rooms.

(a) Production I (b) Production II

(c) Production III (d) Warehouse

Figure 3.1: Measurement locations

3.2.2 Measurement apparatus for the site survey

Site survey measurements in industrial environments were carried out with measurement apparatus including a transmitter and a receiver part, as shown in Fig. 3.2.

The transmitter part (see Fig. 3.2, left) consists of a wireless router (D-Link DI-624+) with an external transmitting antenna (Tx), mounted on a telescopic mast at a height h_{Tx} of about 6 m above ground level. Consequently, the Tx is positioned at approximately the same height as the trusses supporting the ceiling. The trusses are a common location for the placement of industrial APs, because in most factories cable wiring in ducts already exists along these trusses (see Section 2.1). Therefore, industrial APs mounted in the proximity of cable ducts can easily be connected to an existing wired network without the need for additional wiring. The Tx is an omnidirectional, vertically polarized dipole antenna with a gain of 2 dBi. The wireless router supports the IEEE 802.11b and IEEE 802.11g Wireless Local Area Network (WLAN) standards, and was configured to make use of channel 6 (2426 - 2448 MHz) in the 2.4 GHz Industrial, Scientific, and Medical (ISM) band. The wireless router's output power was 14 dBm. The output power was

determined experimentally using a power meter with thermal power sensor. The router was not connected to a wired network for the site survey measurements.

The receiver part (see Fig. 3.2, right) consists of laptop equipped with a Wireless Network Interface Card (WNIC). The WNIC is of type NetGear WAG551 and has a built-in receiving antenna (Rx) with a gain of -2 dBi. The Rx was installed at different heights h_{Rx} of 0.5, 1.5 and 2 m during the site survey. These Rx heights are comparable to the typical height of a wireless terminal mounted on a piece of industrial machinery. The receiver configuration is positioned on a movable cart, and a tachometer (RM1501) is used to measure the travelled distance. During measurements, the cart was pushed forward along straight tracks at a nearly constant speed of 0.25 m/s.

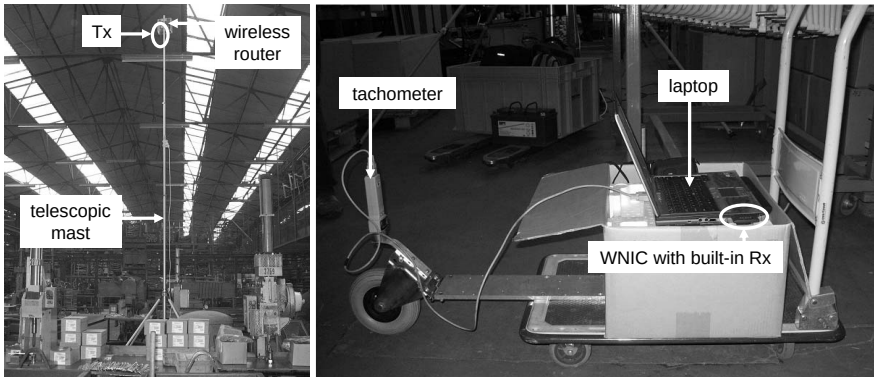

Figure 3.2: Site survey measurement setup: transmitter part (left) and receiver part (right)

3.2.3 Measurement procedure for the site survey

The laptop was equipped with the AirMagnet Laptop Analyzer® software package for the analysis of the 802.11b/g signal transmitted by the AP. Even without a connection to a wired network, the AP regularly transmits wireless packets. The bulk of these packets consists of beacon frames, a type of management frame transmitted by the AP to report its presence and configuration to nearby wireless clients [1].

The parameter of interest logged by the Laptop Analyzer is the Received Signal Strength (RSS) of the transmitted packets in dBm. Through the use of the RSS parameter, it is possible to determine up to which distance from the AP a certain 802.11b/g data rate can be achieved. In each measured factory building and for a fixed location of the AP, the RSS was recorded along several straight tracks at a rate of one sample per second. Consequently, one sample of the RSS was taken about every 0.25 m of travelled distance.

3.3 Link budget calculation

In this section, a link budget is calculated in order to determine the theoretical range R_{theor} in meter of a wireless system. For this link budget, the industrial propagation models developed in chapter 2 are used. The wireless range is calculated specifically for the site survey measurement setup of Section 3.2.2. A flow graph for the determination of the theoretical range R_{theor} is provided in Fig. 3.3, in the block entitled 'theoretical range'.

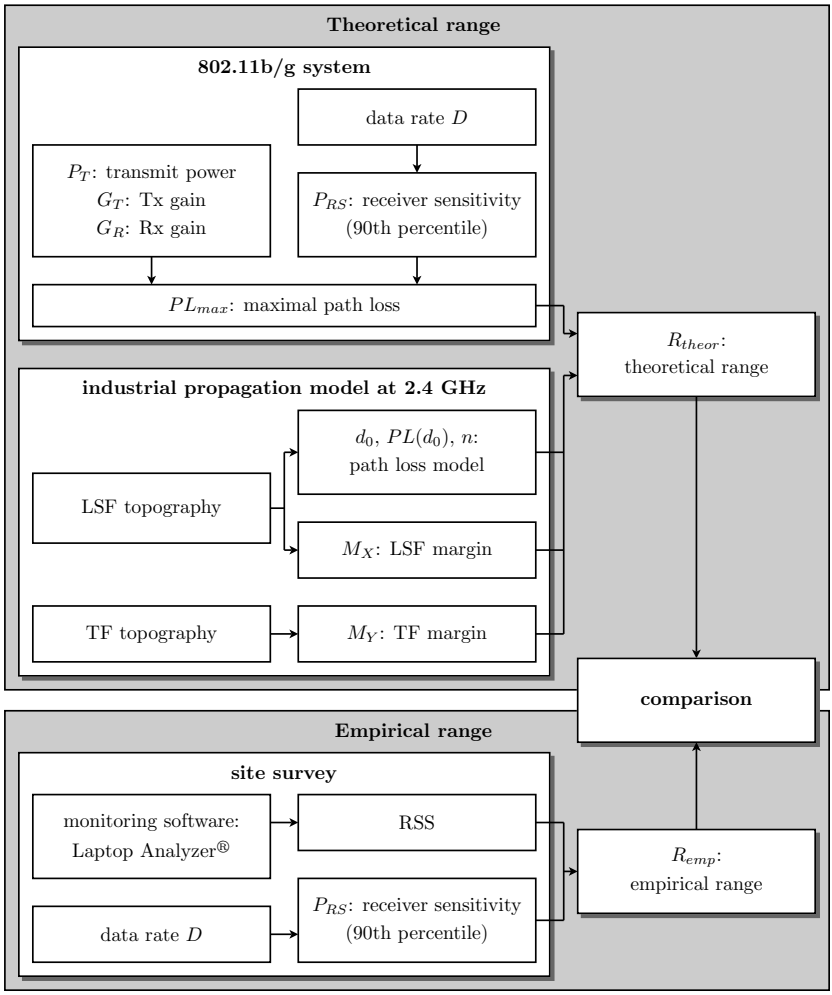

Figure 3.3: Flow graph for comparison of ranges based on theoretical link budget and on site survey

3.3.1 Maximal path loss PL_{max}

Firstly, we calculate the maximal path loss PL_{max} (Fig. 3.3) to which a transmitted signal can be subjected while still being detectable at the receiver. The parameter PL_{max} in dB is calculated as follows:

$$PL_{max} = P_T + G_T + G_R - P_{RS} \tag{3.1}$$

In (3.1), P_T is the wireless transmit power in dBm, G_T and G_R are the Tx and Rx antenna gains in dBi, and P_{RS} is the receiver sensitivity in dBm. For the wireless measurement system in Section 3.2.2, P_T equals 14 dBm, and G_T and G_R are 2 dBi and -2 dBi, respectively. The receiver sensitivity P_{RS} depends on the data rate of the wireless communication link (for a predefined error rate), as well as on the characteristics of the wireless channel the antenna is used in. Usually, values of P_{RS} for the different 802.11b/g data rates are supplied by the WNIC manufacturer. These values are often optimistic: it is our experience that generally a higher power than the receiver sensitivity provided by the WNIC manufacturer is needed to achieve a certain data rate. This is due to the fact that receiver sensitivities are usually measured by the manufacturer in an anechoic chamber. In this environment, multipath propagation of the transmitted signal is greatly reduced by absorbers. Alternatively, receiver sensitivities are measured with equipment which emulates an Additive White Gaussian Noise (AWGN) channel. Similar to propagation in an anechoic chamber, the AWGN channel does not account for fading induced by multipath propagation. An industrial environment on the other hand is heavily subjected to multipath propagation. Multiple reflections cause InterSymbol Interference (ISI) and therefore degrade the *quality* of the transmitted signal. Because of the lack of multipath propagation in an anechoic chamber or an AWGN channel, the quality of the received 802.11b/g signal will be higher. Therefore, it is expected that a certain data rate (for a fixed error rate) can be maintained at lower signal strengths in an anechoic chamber or AWGN channel compared to a true industrial environment due to the higher signal quality in the former.

To calculate PL_{max}, we therefore did not use the receiver sensitivities according to the WNIC's technical specifications. Instead, receiver sensitivities P_{RS} were extracted from the site survey measurement data gathered in the industrial facilities (Fig. 3.3). During measurements, the site survey software logged the points in time at which the 802.11b/g system switched to a new data rate D in Mbps, as well as the received signal strength RSS_D at the time of change. The receiver sensitivity P_{RS} for a data rate D was then calculated as the 90th percentile of RSS_D: when the measured RSS increases to this percentile, the wireless system will already have switched to a data rate of D in 90 % of the cases. These 90th percentiles therefore provide worst-case values for the receiver sensitivities. This procedure is visualised in Fig. 3.4 which shows the histogram of RSS_D for D =

18 Mbps. The 90th percentile of RSS_D, i.e. P_{RS}, is equal to -73 dBm for this data rate. Receiver sensitivities P_{RS} calculated with this method are shown in Table 3.1 for the different 802.11b/g data rates D. Also shown are the maximal path losses PL_{max}, calculated for the site survey measurement system of Section 3.2.2.

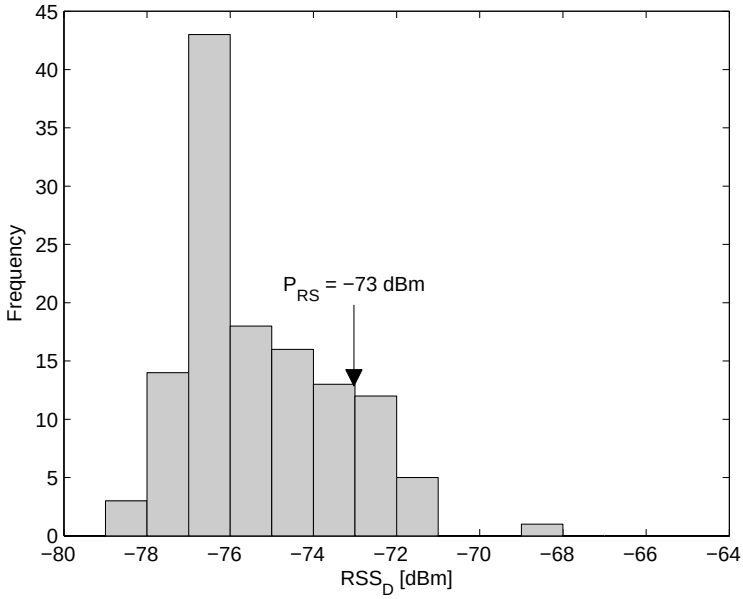

Figure 3.4: Histogram of RSS_D for a data rate of 18 Mbps and corresponding P_{RS}

D [Mbps]	P_{RS} [dBm]	PL_{max} [dB]
1	-86	100
2	-80	94
5.5	-79	93
11	-77	91
12	-76	90
18	-73	87
24	-68	82
36	-64	78
48	-58	72
54	-54	68

Table 3.1: Receiver sensitivities P_{RS} and maximal path losses PL_{max} for the different 802.11b/g data rates D

3.3.2 Path loss model

To determine the range of the wireless 802.11b/g communication system, the maximal path loss PL_{max} in (3.1) has to be compared to a distance dependent path loss model for industrial environments (Fig. 3.3). In the following, the one-slope path loss model (2.2) is used. For the purposes of this chapter, the one-slope path loss model (2.2) is rewritten to include two extra terms X and Y: X accounts for the random shadowing effect (as per Section 2.3.1.4 and equation (2.3)), while Y accounts for the random temporal fading effect (as per Section 2.3.2.3 and equation (2.5)).

$$\begin{aligned} PL\left(d\right) &= PL\left(d_0\right) + 10n \cdot \log\left(d/d_0\right) + X + Y \\ &= PL_{med}\left(d\right) + X + Y \end{aligned} \tag{3.2}$$

In (3.2), X is a lognormally distributed random variable with zero median in dB and standard deviation σ [dB], and Y is a random variable with zero median in dB that follows a Rice distribution characterized by a Ricean K-factor [dB]. As such, the one-slope model (3.2) without the X and Y terms expresses the median path loss $PL_{med}\left(d\right)$ at distance d.

Numerical values of the one-slope model's parameters at a center frequency of 2.4 GHz were previously determined in Table 2.1 for three Large-Scale Fading (LSF) topographies and for a general topography which combined all measurement data of the three LSF topographies ("All" in Table 2.1). In this chapter, the latter general topography will be referred to as LSF topography 4. The one-slope model's parameters at 2.4 GHz in Table 2.1 are retaken in Table 3.2. Next, regarding industrial temporal fading, the industrial environment in production I, II, and III can for the largest part be categorized under Temporal Fading (TF) topography 2. The measured warehouse environment on the other hand is part of TF topography 4. In Table 2.3, an average K-factor of about 12 dB was found at 2.4 GHz for both TF topographies 2 and 4. The same K-factor of 12 dB will therefore be used for link budget calculations for all four LSF topographies (see Table 3.2).

LSF topography	$PL(d_0)$ [dB]	n [-]	σ [dB]	K [dB]	M_X [dB]	M_Y [dB]
1	67.43	1.72	4.73	12	6.05	4
2	72.71	1.52	4.61	12	5.90	4
3	80.48	1.69	6.62	12	8.47	4
4	71.84	2.16	8.13	12	10.41	4

Table 3.2: Parameters of the industrial propagation model (d_0 = 15 m) at 2.4 GHz and link budget margins for the different industrial topographies

3.3.3 Margins for shadow fading and temporal fading

The following discusses the margins included in the link budget to account for the effects of shadow fading and temporal fading in the industrial environment (Fig. 3.3).

3.3.3.1 Shadow fading margin M_X

In the one-slope path loss model (3.2), the random variable X accounts for local shadowing of the Rx antenna. For the calculation of the link budget, the shadowing phenomenon is taken into account through the inclusion of a shadow fading margin M_X [4]. The shadow fading margin is determined such that p = 90% of the locations on the edge of the cell are covered by the wireless system. This corresponds to a coverage percentage of about 95% of all locations within the cell. Recalling that the shadow fading random variabele X is lognormally distributed with zero median in dB and standard deviation σ in dB, M_X is calculated as:

$$M_X = \sqrt{2}\sigma \cdot \mathrm{erfc}^{-1}\left[2\left(1-p\right)\right] \tag{3.3}$$

In (3.3), erfc^{-1} is the inverse complementary error function. Numerical values of the shadow fading margin M_X are shown in Table 3.2 for each LSF topography.

3.3.3.2 Temporal fading margin M_Y

The average K-factor of 12 dB in Table 3.2 is used to calculate a temporal fading margin M_Y. The temporal fading margin is determined to provide wireless coverage with an acceptable average Packet Error Rate (PER) of 10%, which lasts 100% of the time. Assuming the occurences of bit errors are identically and independently Bernoulli distributed, the corresponding average Bit Error Rate (BER) can be calculated as [5]:

$$BER = 1 - \left(1 - PER\right)^{1/PS} \tag{3.4}$$

In (3.4), PS is the packet size in bits. As packet size, the default value of 1024 bytes set in the Laptop Analyzer is used. Using (3.4), an average PER of 10% translates into an average BER of approximately 10^{-5}. For Ricean fading channels, the temporal fading margins as a function of the K-factor, the average BER, and the percentage of the time this average BER has to be maintained, were determined through Monte Carlo simulations in [6]. Based on these results, a temporal fading margin M_Y of about 4 dB has to be included in the link budget to continuously maintain an average BER of 10^{-5} (see Table 3.2).

3.3.4 Theoretical range R_{theor}

The theoretical range R_{theor} in meter of the wireless system under consideration can be determined using the descriptions in Sections 3.3.1 through 3.3.3. At distance $d = R_{theor}$ from the AP, the path loss, as determined by the industrial path loss model and the fading margins, is equal to the maximal path loss PL_{max}, as determined by the 802.11b/g system (Fig. 3.3).

$$PL_{med}\left(R_{theor}\right) + M_X + M_Y = PL_{max} \tag{3.5}$$

Equation (3.5) can be solved for R_{theor} using (3.2):

$$R_{theor} = d_0 \cdot 10^{(PL_{max} - M_X - M_Y - PL(d_0))/(10n)} \tag{3.6}$$

Using (3.6), the range R_{theor} of the wireless system can be calculated for the different 802.11b/g data rates and the different LSF topographies. The wireless range is calculated for some of these data rates and industrial topographies:

- From the different 802.11b/g data rates, three data rates of **2, 11, and 18 Mbps** were chosen for the calculation of the link budget. Data rates between 2 and 11 Mbps are adequate to fulfill most needs for current industrial wireless communication, such as warehouse stock monitoring and uninterrupted observation and adjustment of industrial processes. Ranges are also calculated for the larger data rate of 18 Mbps, to account for potentially more traffic-intensive industrial applications in the near future. For example, a multitude of process parameters could be monitored by the nodes of a wireless sensor network which uses the ZigBee standard [7]. The data aggregated from these nodes can then be sent to a wireless AP over an 802.11 link. As wireless sensor networks with a large number of nodes could generate a substantial amount of aggregated traffic, a data rate of 11 Mbps may not be sufficient when such networks are rolled out in industrial environments.
- Visits to the different factories revealed that in most production centers, the industrial inventory's height does not largely exceed the height of the Rx: industrial machinery was usually of height 2 to 3 m. Because OBstructed line of Sight (OBS) situations limit the range of a wireless communication system the most, **LSF topography 2** (Table 3.2) is considered most suitable for range prediction in **production centers**. The physical layout of factory warehouses is substantially different when compared to production centers. The inventory in warehouses is for the largest part made up from storage racks which often reach to the ceiling. Storage racks are usually set up in an orderly fashion, so that several parallel aisles, separated from one another

by stored goods, are created. Line Of Sight (LOS) paths are important in warehouses and can often stretch from wall to wall along long aisles. In an OBS situation, the attenuation of the received signal is dependent on the density of the stored goods, which changes over time. At one time, the location of the receiver is situated in LSF topography 3 when goods are heavily stacked, while at another time, the same location could be categorized into LSF topography 2 with low stacking of goods. Because of the importance of LOS paths and the dynamic change in number and height of stored goods, the general **LSF topography 4** (Table 3.2) is considered most suitable for range prediction in **warehouses**.

The theoretical ranges R_{theor} (formula (3.6)) are given in Table 3.3.

Data rate [Mbps]	R_{theor} [m] production center	R_{theor} [m] warehouse
2	84	34
11	53	25
18	29	16

Table 3.3: Theoretical ranges R_{theor} in production centers and warehouses at data rates of 2, 11, and 18 Mbps

3.4 Site survey data analysis

In this section, it is explained how the site survey measurement data is analyzed to assess the wireless range of the AP. Firstly, a floor plan of the measured industrial room is used to graphically determine the coverage area around the AP. Next, the empirical range R_{emp} is extracted from the covered area. A flow graph for the extraction of R_{emp} from site survey data is provided in Fig. 3.3, in the block entitled 'empirical range'.

3.4.1 Graphical determination of the site survey coverage area

To determine the range of the site survey measurement system, the RSS values recorded along each measurement track were compared to the receiver sensitivities P_{RS} at 2, 11, and 18 Mbps (Fig. 3.3). An example of such a comparison is shown in Fig. 3.5 for a site survey conducted in production I at height h_{Rx} of the receiving antenna equal to 0.5 m. The positioning of the AP for the site survey is also indicated.

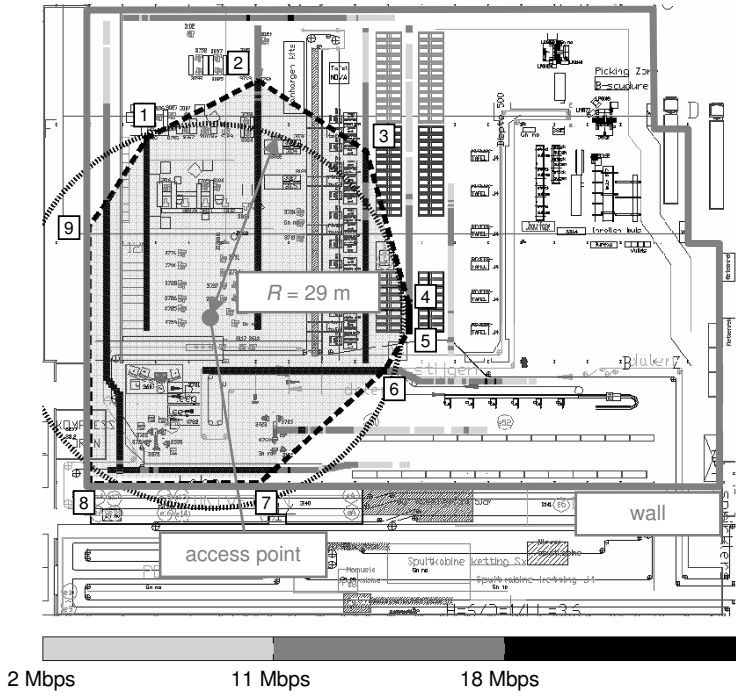

Figure 3.5: Achievable data rates of 2, 11, and 18 Mbps along several site survey measurement tracks in production I, and contour (dashed line) and topography 2 link budget circle (dotted line) for a data rate of 18 Mbps

In Fig. 3.5, the parts of the measurement tracks where a data rate of at least 18 Mbps can be achieved are shown in black. Along these partial tracks, the recorded RSS is greater than or equal to -73 dBm, the receiver sensitivity at 18 Mbps (see Table 3.1). Parts of tracks where a data rate between 11 and 18 Mbps is obtained are shown in a dark gray, and the RSS parameter satisfies -77 dBm $\leq$ RSS $<$ -73 dBm along those parts. Finally, parts of tracks where the achievable data rate is between 2 and 11 Mbps are shown in a light gray, and correspond to -80 dBm $\leq$ RSS $<$ -77 dBm.

Based on this plot, simple contours within which the data rate is at least 18, 11, or 2 Mbps are drawn. A contour for 18 Mbps is shown in Fig. 3.5 (dashed line), for which the coverage area within the contour is lightly shaded. The contour's vertices are chosen to coincide with the points along the measurement tracks farthest from the Tx at which the data rate under consideration is still achievable, or to end on a wall of the industrial room. For the contour in Fig. 3.5, nine vertices were obtained, numbered 1 through 9 in the figure. These vertices are then interconnected by straight lines, so that the resulting site survey contour has a simple polygonal

shape. From the manner in which these contours are constructed, it follows that the measurement tracks enclosed by a contour are nearly 100% covered for the data rate under consideration. Other locations within the contour are also likely to receive the same data rate: they are similarly cluttered by industrial inventory and at the same or smaller distances from the AP as points along the measured tracks.

3.4.2 Empirical range R_{emp}

From the site survey contours, the empirical range of the site survey measurement configuration is estimated (Fig. 3.3). For each data rate and measured industrial room, samples of the empirical range R_{emp} in meter are collected from the distances between the contour's vertices and the AP. Vertices that end on a wall of the industrial room are not considered, as the empirical ranges that follow from those vertices are not limited by industrial inventory (e.g., for Fig. 3.5, only vertices 1 through 6 are considered for samples of R_{emp}).

3.5 Validation of link budget by site survey

In this section, the wireless range and the required number of APs according to the link budget and the site survey are compared (see flow graph in Fig. 3.3). In Section 3.5.1, this comparison is done for site surveys conducted at height h_{Rx} of the receiving antenna equal to 0.5 m, which is the Rx height at which most of the site survey measurements were executed. In Section 3.5.2, the effect on the empirical range when changing h_{Rx} between 0.5, 1.5, and 2 m is discussed.

3.5.1 Comparison between theoretical and empirical ranges

3.5.1.1 Production centers

Fig. 3.5 shows the site survey contour (dashed line) and the theoretical link budget circle with radius R_{theor} (dotted line) for a data rate of 18 Mbps in production I. Also shown is the position of the AP, and the wall separating production I from the rest of the industrial site. As shown in Section 3.3.4, the path loss model for industrial topography 2 is best used for range calculation in production centers. Then, according to Table 3.3, the wireless range R_{theor} at 18 Mbps equals 29 m. In Fig. 3.5, good agreement between the site survey contour and the link budget circle is observed. For a data rate of 18 Mbps, the industrial topography 2 path loss model seems fit for theoretical range prediction which reflects the true range of an 802.11b/g system.

Fig. 3.6 shows the site survey contour (solid line) and the link budget circle for industrial topography 2 (dotted line, R_{theor} = 53 m) for a data rate of 11 Mbps in production I. The AP's location is the same as in Fig. 3.5. For a data rate of

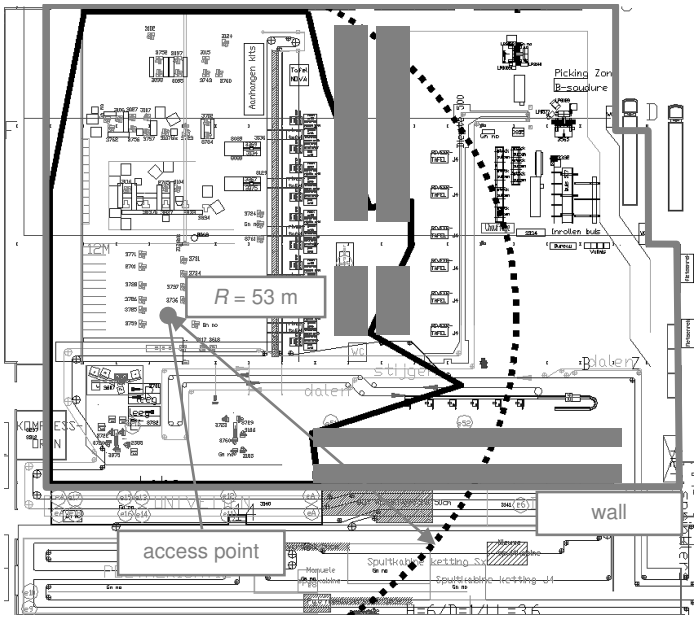

Figure 3.6: Site survey contour (solid line) and topography 2 link budget circle (dotted line) in production I for a data rate of 11 Mbps

11 Mbps, the agreement between the empirical and the theoretical range is reasonable, but not as good as in Fig. 3.5 for 18 Mbps. In Fig. 3.6, the link budget circle encloses the site survey contour entirely. The reduced range of the site survey measurement is attributed to several large obstacles present in production I, which are higher than the Tx (h_{Tx} = 6 m) and are therefore not part of industrial topography 2. These large obstacles are shown as gray rectangles in Fig. 3.6 and consist of densely stacked metal containers holding various metal parts. These containers are also shown in Fig. 3.7 (green). These metal containers greatly reduce the signal strength of the 802.11b/g signal, as a data rate of 11 Mbps is nearly unfeasible beyond these obstacles. Similarly, the containers were also found to heavily attenuate the propagating signal for a data rate of 2 Mbps, by which the theoretical range R_{theor} = 84 m at 2 Mbps again overestimated the real, empirical range for this data rate.

To maximize the wireless range, industrial APs are best installed as far as possible from large obstacles and walls, as these objects greatly attenuate the 802.11b/g signal. When considering the link budget circle in Fig. 3.6, one could conclude that one AP in the centre of production I is sufficient to wirelessly cover

Figure 3.7: Stacked metal containers in production I

the entire room. However, the site survey shows that two APs are needed to obtain a data rate of 11 Mbps all over the room. An AP should be installed both left and right of the large obstacles in Fig. 3.6, as these obstacles divide the production center in roughly two equal-sized isolated parts. If the link budget circle encloses a few large obstacles, it is recommended to install additional APs in the areas that are shadowed by these obstacles. These observations made for production I are also found to be valid for the site surveys conducted in production II and III.

To quantify the deviation between the site survey contour and the theoretical link budget circle in production centers, differences ΔR in meter between samples of the empirical range R_{emp} and the theoretical range R_{theor} are calculated:

$$\Delta R = R_{emp} - R_{theor} \tag{3.7}$$

Samples of ΔR are grouped together according to data rate, without distinguishing between the specific measurement site (production I, II, or III) or the location of the AP at the measurement site. In Table 3.4, statistics of the deviations ΔR between site survey and link budget in production centers are given for each data rate D of 2, 11, and 18 Mbps. Per data rate, point estimates of the mean and the standard deviation of ΔR are given as $\overline{\Delta R}$ and $S_{\Delta R}$, respectively [8]. Also shown is the number of ΔR samples used in the calculation of $\overline{\Delta R}$ and $S_{\Delta R}$, and the mean relative error $\left|\overline{\Delta R}\right| / R_{theor}$ between the empirical and theoretical range.

Prior to discussing the results in Table 3.4, it should be noted that the ΔR

Production center				
D [Mbps]	samples [-]	$\overline{\Delta R}$ [m]	$S_{\Delta R}$ [m]	$\lvert\overline{\Delta R}\rvert / R_{theor}$ [%]
2	62	-31.8 ($[-34.9, -28.8]$)	12.0 ($[10.2, 14.6]$)	37.9
11	68	-6.4 ($[-9.4, -3.4]$)	12.4 ($[10.6, 14.9]$)	12.1
18	76	4.6 ($[2.9, 6.3]$)	7.2 ($[6.2, 8.6]$)	15.9
Warehouse				
D [Mbps]	samples [-]	$\overline{\Delta R}$ [m]	$S_{\Delta R}$ [m]	$\lvert\overline{\Delta R}\rvert / R_{theor}$ [%]
2	61	3.6 ($[0.8, 6.4]$)	10.9 ($[9.2, 13.2]$)	10.6
11	32	2.6 ($[-1.8, 6.9]$)	12.1 ($[9.7, 16.0]$)	10.4
18	12	10.3 ($[6.0, 14.5]$)	6.7 ($[4.7, 11.4]$)	64.4

Table 3.4: Statistics of $\Delta R = R_{emp} - R_{theor}$ for the production centers and the warehouse at data rates of 2, 11, and 18 Mbps

samples in production centers passed a Kolmogorov-Smirnov (KS) test for normality at significance level 5% for each individual data rate. Therefore, under the assumption of normality, $\overline{\Delta R}$ and $S_{\Delta R}$ can be used to calculate 95% Confidence Intervals (CIs) for the true mean $\mu_{\Delta R}$ and true standard deviation $\sigma_{\Delta R}$ of ΔR [8]. Calculated 95 % CIs are given between brackets in Table 3.4 and indicate how reliable the point estimates $\overline{\Delta R}$ and $S_{\Delta R}$ can be deemed. For production centers in Table 3.4, it is found that the difference between $\overline{\Delta R}$ ($S_{\Delta R}$) and the bounds of the corresponding CI is maximally 3.0 m (2.6 m). These small differences show that $\overline{\Delta R}$ and $S_{\Delta R}$ can be considered reliable point estimates.

The mean $\overline{\Delta R}$ can be interpreted as a measure for the agreement between the empirical and the theoretical range. For a data rate of 2 Mbps in production centers, the theoretical range overestimates the empirical range of the AP ($\overline{\Delta R}$ = -31.8 m and a relative error of 37.9% in Table 3.4). As the theoretical range is the largest for the lowest data rate of 2 Mbps, it becomes more likely for the propagating signal to encounter large obstacles at some point within the theoretical range. Consequently, the largest discrepancy between theoretical and empirical range can be expected for the lowest data rate. For a data rate of 11 Mbps, the theoretical range still somewhat overestimates the empirical range ($\overline{\Delta R}$ = -6.4 m and a relative error of 12.1% in Table 3.4). However, the deviation is less when compared to 2 Mbps, and can again be attributed to attenuation by large obstacles. Finally, for a data rate of 18 Mbps, the theoretical range slightly underestimates the empirical range ($\overline{\Delta R}$ = 4.6 m and a relative error of 15.9% in Table 3.4). Because of the small theoretical range for this data rate, it is not unlikely that LOS is still present at a number of locations at distance $d = R_{theor}$. As the used path loss model for LSF topography 2 only accounts for obstructed paths (see Section 3.3.2), it is understandable that the theoretical range is somewhat smaller when compared to

the average empirical range at 18 Mbps.

The standard deviation $S_{\Delta R}$ of the difference ΔR (which is also the standard deviation of R_{emp}, as R_{theor} is a constant) can be interpreted as a measure of the degree in which the site survey contour resembles an ideal circular geometry (see the link budget circle), with a lower standard deviation meaning a better resemblance. From the results for the $S_{\Delta R}$ parameter in production centers in Table 3.4, it is clear that the area covered by an AP deviates from the ideal circular shape, although to a limited extent. The lowest value of $S_{\Delta R}$ is recorded for the highest data rate of 18 Mbps. As large obstacles randomly located in the production center play an more important role at the lower data rates of 2 and 11 Mbps, the spread of the R_{emp} samples, and therefore also $S_{\Delta R}$, increases.

3.5.1.2 Warehouse

As motivated in Section 3.3.4, the path loss model for LSF topography 4 is best used for range calculation in warehouses. Therefore, the ranges R in Table 3.3 calculated for topography 4 are further used. Fig. 3.8 shows the site survey contour (solid line) and the link budget circle (dotted line, R_{theor} = 25 m) for a data rate of 11 Mbps in the warehouse. Fig. 3.8 exhibits good agreement between the site survey contour and the link budget circle. Similar good agreement was also found for the site surveys at data rates of 2 and 18 Mbps.

As for the site surveys conducted in production centers, differences ΔR in meter between samples of the empirical range R_{emp} and the theoretical range R_{theor} are calculated for each site survey in the warehouse. For the warehouse, point estimates $\overline{\Delta R}$ of the mean and $S_{\Delta R}$ of the standard deviation of ΔR are given for each data rate in Table 3.4, as well as the number of ΔR samples used in the calculation of $\overline{\Delta R}$ and $S_{\Delta R}$. As for the production centers, the ΔR samples for each data rate in the warehouse also passed a KS test for normality at significance level 5%. Under this assumption of normality, 95% CIs for the true mean $\mu_{\Delta R}$ and true standard deviation $\sigma_{\Delta R}$ of ΔR are calculated and given between brackets in Table 3.4. For the warehouse, it is found that the difference between $\overline{\Delta R}$ ($S_{\Delta R}$) and the bounds of the corresponding CI is maximally 4.3 m (4.7 m). As for the production centers, these small differences again show that $\overline{\Delta R}$ and $S_{\Delta R}$ can be considered reliable point estimates for the site surveys executed in the warehouse.

For a data rate of 2 Mbps in the warehouse, the theoretical range R_{theor} agrees well with the empirical range R_{emp} of the AP ($\overline{\Delta R}$ = 3.6 m and a relative error of 10.6% in Table 3.4). Similar good agreement is found for a data rate of 11 Mbps, where $\overline{\Delta R}$ = 2.6 m and the relative error is 10.4%. For a data rate of 18 Mbps, the theoretical range underestimates the empirical range ($\overline{\Delta R}$ = 10.3 m and a relative error of 64.4% in Table 3.4). This is because the site survey measurements showed that a data rate of 18 Mbps in the warehouse is only attainable in LOS with the

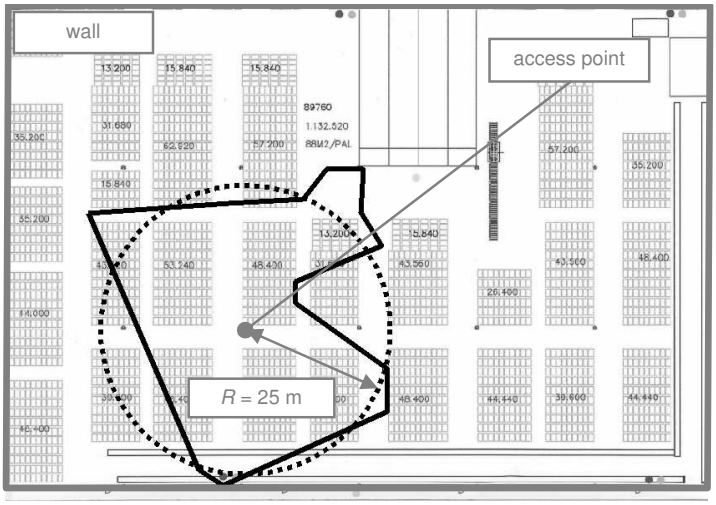

Figure 3.8: Site survey contour (solid line) and topography 2 link budget circle (dotted line) in the warehouse for a data rate of 11 Mbps

Tx. However, for the calculation of the theoretical range, the path loss model for LSF topography 4 was used. This topography includes, apart from LOS paths, also highly lossy obstructed paths (see Section 3.3.2). It is therefore explainable that the topography 4 path loss model could underestimate the true, empirical range for data rates for which only low loss LOS communication seems possible.

Regarding the values of the standard deviation $S_{\Delta R}$ of the ΔR samples, the same conclusions as those in Section 3.5.1.1 for production centers can be drawn. For each data rate separately in Table 3.4, standard deviations $S_{\Delta R}$ are comparable between production centers and the warehouse. For each individual data rate, Levene's test for equality of variances was run to verify whether the variance $\sigma^2_{\Delta R}$ is equal for the production centers and the warehouse [8]. These tests passed at a 5% significance level for all three data rates, as a result of which equal variances $\sigma^2_{\Delta R}$, and therefore standard deviations $\sigma_{\Delta R}$, can be assumed for the production centers and the warehouse.

3.5.2 Effect of h_{Rx} on the empirical range

In this section, the effect of the receiving antenna's height h_{Rx} on the empirical range is investigated. The majority of the site survey measurements were performed with h_{Rx} equal to 0.5 m. Additional site surveys with h_{Rx} equal to 1.5 and 2 m were carried out for one location of the AP in two industrial rooms, namely production III and the warehouse. Fig 3.9 shows site survey contours for the three

h_{Rx} in production III, and the LSF topography 2 link budget circle (R_{theor} = 53 m). From 3.9, it is clear that all three site survey contours cover similar areas, leading us to suspect that the effect of h_{Rx} on the empirical range is limited. Additionally, all three site survey contours also show satisfactory agreement with the topography 2 link budget circle.

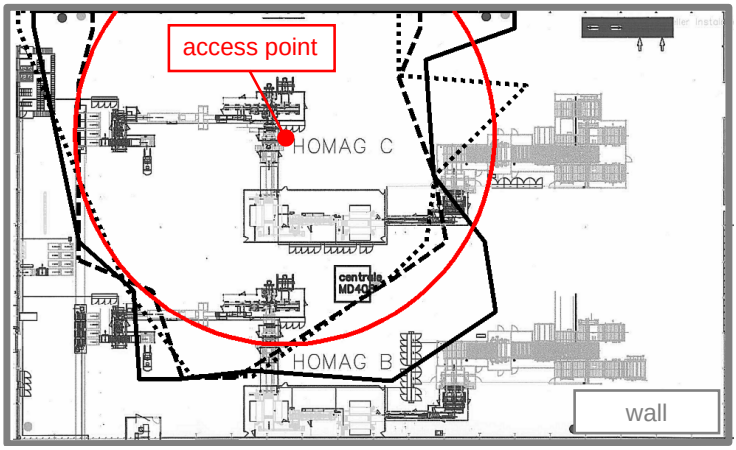

Figure 3.9: Site survey contour for h_{Rx} = 0.5 m (solid black line), 1.5 m (dashed black line), and 2 m (dotted black line), and topography 2 link budget circle (solid red line) in production III for a data rate of 18 Mbps

To investigate the effect of h_{Rx} on the empirical range R_{emp}, a one-way ANalysis Of VAriance (ANOVA) was performed with response variable R_{emp} and independent grouping variable h_{Rx} [8]. Samples of the empirical range collected at h_{Rx} = 0.5 m are associated with the variable $R_{emp,0.5}$, which has mean $\mu_{0.5}$ and standard deviation $\sigma_{0.5}$. Analogously, samples of the empirical range gathered at h_{Rx} = 1.5 and 2 m are grouped as $R_{emp,1.5}$ (mean $\mu_{1.5}$, standard deviation $\sigma_{1.5}$) and $R_{emp,2}$ (mean μ_2, standard deviation σ_2), respectively. The analysis of variance tests the null hypothesis that $\mu_{0.5} = \mu_{1.5} = \mu_2$, or put differently, that the height h_{Rx} has no significant effect on the empirical range. An analysis of variance was executed for each of the three data rates of 2, 11, and 18 Mbps in both production III and the warehouse, so a total of 6 tests of the null hypothesis were run.

Prior to performing the analysis of variance, various assumptions on the R_{emp} samples have to be checked. Firstly, it is assumed that $R_{emp,0.5}$, $R_{emp,1.5}$, and $R_{emp,2}$ are independent by design of the experiment. Normality and equality of variances of $R_{emp,0.5}$, $R_{emp,1.5}$, and $R_{emp,2}$ were checked by performing KS tests and Levene's tests, respectively. Both types of tests passed for all 6 combinations of measured industrial room and data rate at a significance level of 5%. The analy-

sis of variance showed that there was no significant effect of h_{Rx} on the empirical range R_{emp} for 5 out of 6 combinations of measured industrial room and data rate, i.e., the null hypothesis $\mu_{0.5} = \mu_{1.5} = \mu_2$ could not be rejected at the 5% significance level for those 5 combinations. Only in production III for a data rate of 11 Mbps, a significant effect of h_{Rx} on the empirical range R_{emp} was found. This can be explained by the observation that the site survey contours for 11 Mbps in production III cut across an area where wooden boards are stacked to a height of about 1 m. These wooden boards cause substantially different reception of the 802.11b/g signal between the two Rx heights of 0.5 and 2 m. Nevertheless, the receiving antenna's height does not appear to have a significant effect on the empirical range in the majority of cases.

3.6 Conclusions

In this chapter, a validation of link budget calculations based on the industrial propagation models of chapter 2 by a number of site survey measurements has been presented for IEEE 802.11b/g wireless systems deployed in an industrial environment. More specifically, it was investigated if the wireless range according to an industrial propagation model matches the range extracted from site survey measurements.

For the site surveys, the AP was mounted at 6 m above ground level, while the received signal strength was recorded at 0.5 m above the ground for the majority of measurements, and at 1.5 and 2 m above the ground for some of the measurements. For range calculation in production centers, the path loss model for LSF topography 2 was used. For range calculation in warehouses, LSF topography 4 was chosen. The comparison between link budget and site survey was made for three practically important 802.11b/g data rates of 2, 11, and 18 Mbps.

Generally good statistical agreement was established between the theoretical range according to the link budget and the empirical range according to the site survey measurements. However, the empirical range in production centers at lower data rates (2 and 11 Mbps) can at certain occasions be substantially lower than the calculated theoretical range. These statistical deviations can be explained from the physical layout of the environment: the lower empirical range in some production centers can be attributed to severe signal attenuation by large obstacles, which are present in some production halls. These large obstacles consist of densely packed storage racks and gantries which have heights often exceeding that of the AP. It is therefore advised to install additional APs in areas shadowed by these obstacles, as these are often impenetrable to the 802.11b/g signal. Furthermore, to maximize the range of an industrial AP, it is recommended to keep the APs clear of these large obstacles as well as of walls. Additionally, a result was that there appears to be very limited differences in empirical site survey ranges for receiving antenna

heights of 0.5, 1.5, and 2 m.

In conclusion, it was found that an industrial propagation model can be used with success for indoor site planning, provided that the physical layout of the environment is taken into consideration: most notably the large obstacles in some production centers.

References

[1] IEEE Standards Association. *Wireless LAN Medium Access Control (MAC) and Physical Layer (PHY) Specifications*. ANSI/IEEE Std 802.11, 1999.

[2] J. De Bruyne, W. Joseph, L. Verloock, and L. Martens. *Evaluation of Link Performance of an Indoor 802.11g Network*. In Fifth IEEE Consumer Communications and Networking Conference Proceedings, pages 425–429, Las Vegas, NV, USA, January 2008.

[3] B. E. Henty. *Throughput Measurements and Empirical Prediction Models for IEEE 802.11b Wireless LAN (WLAN) Installations*. Master's thesis, Virginia Polytechnic Institute and State University, Blacksburg, VA, USA, August 2001.

[4] S. R. Saunders. *Antennas and Propagation for Wireless Communication Systems*. Wiley and Sons, 1999.

[5] H. Lin and L. Cheng. *Modeling Network Bandwidth of IEEE 802.11 Wireless Local Area Networks*. In IEEE International Conference on Systems, Man and Cybernetics Proceedings, pages 3563–3568, Waikoloa, HI, USA, October 2005.

[6] F. Davarian. *Fade Margin Calculation for Channels Impaired by Rician Fading*. IEEE Transactions on Vehicular Technology, 34(1):41–44, February 1985.

[7] ZigBee Alliance. *ZigBee Specification v1.0*. ZigBee Document 053473r00, 2005.

[8] M. H. Kutner, C. J. Nachtsheim, J. Neter, and W. Li. *Applied Linear Statistical Models*. McGraw-Hill, fifth edition, 2005.

4

Delay characteristics in an industrial environment

4.1 Introduction and related work

In this chapter, an analysis of the Channel Impulse Response (CIR) in industrial environments is presented. The CIR is defined as the (complex) amplitude of received MultiPath Components (MPCs) as function of their delay. Analyzing the CIR thus makes it possible to assess the delay dispersion (i.e., the spread of received power in the time delay domain) of the industrial channel. Delay dispersion can have a noticeable impact on the performance of wireless communication systems. Delay dispersion gives rise to multiple echoes of the same signal at the receiver's side and is caused by multipath propagation. For example for Orthogonal Frequency-Division Multiplexing (OFDM) communication systems, echoes can potentially corrupt the communication when a transmitted symbol experiences crosstalk from echoes of other symbols transmitted at another time (this phenomenon is also called "inter-symbol interference"). There do however exist various schemes to combat the negative effects of delay dispersion. In OFDM for example, symbols are modulated onto a large number of narrowband frequency carriers. A large number of carriers allows to modulate each carrier at a smaller symbol rate. For all carriers together, the combined symbol rate will still be equal to the large symbol rate of a single carrier transmission scheme. Because each carrier is modulated more slowly, the duration of each symbol is larger which reduces the chances of inter-symbol interference. Another strategy to deal with delay dis-

persion is found in rake receivers which are designed to "rake in" different MPCs and to subsequently add them coherently. A rake receiver therefore not as much combats multipath as it tries to make advantage of it to increase the signal-to-noise ratio.

Only limited literature about the CIR in industrial channels exists, e.g., [1–4]. In [1] and [2], narrowband models for the CIR at a center frequency of 1300 MHz are presented. The focus of the work in [1] and [2] is on the statistical modelling of the number of captured MPCs, which is applied in rake receiver design. Wideband frequency-domain channel sounding measurements are reported in [3] and [4]. In [3], the squared magnitude of the CIR as a function of delay is approximated by the well-established exponential decay. In [4], CIR measurements are fitted to the widely used Saleh-Valenzuela (SV) model [5]. This model assumes that the MPCs arrive within separate clusters, and therefore received power versus delay is modelled as a double exponential decay.

In our measurements, a distinct clustering of MPCs is also notable, and therefore, the SV model will also be adopted here. New statistical modifications to the rates of power decay in the SV model are presented. The statistical soundness of these modifications is verified through hypothesis tests and Confidence Intervals (CIs). Where possible, the proposed adjustments are explained from propagation mechanics characteristic for industrial environments. Additionally, other propagation parameters such as the statistical distribution of Small-Scale Fading (SSF), and delay spread are investigated. In this chapter, the measurements of the CIR are performed through frequency-domain channel sounding and the virtual array method [6]. Channel time-invariance during measurements, a prerequisite for this type of channel sounding, is validated for industrial environments. In total, 480 samples of the CIR were obtained.

The outline of this chapter is as follows. Section 4.2 details the measurement procedure and subsequent processing of measurement data to gather samples of the CIR. In Section 4.3, propagation models for the measurement data are discussed. Section 4.4 presents the results of fitting the measurement data to the proposed propagation models. Finally, important findings and conclusions are summarized in Section 4.5.

4.2 Measurement procedure and data processing

4.2.1 Description of the measured environment

Propagation measurements were conducted in different production rooms of a wood processing facility located in Flanders, Belgium. The factory produces and stores wooden flooring products. Raw wooden materials are processed in workplaces by semi-automated machinery used for sawing, breaking, and painting the

wood. The buildings at the factory site are one-storied, and have a ceiling height of approximately 7 m. All measured industrial halls exhibited similar physical properties: they have concrete floors and metal ceilings supported by steel truss work. Moreover, building walls are made of thick, precast concrete. The industrial inventory at all measurement locations consists for the largest part of similar metal machinery and piping. The machinery extends to heights between 2 and 3 m above ground level. Fig. 4.1 presents a view of the measurement environment.

Figure 4.1: Measurement environment: production room in a wood processing facility

4.2.2 Frequency-domain measurements

Measurements of the CIR were performed in the frequency domain using a Rohde & Schwarz ZVR vector network analyzer. This allows for the determination of the complex channel transfer function $\mathcal{H}(f)$ for a certain range of the frequency f. The frequency f of the transmitted signal was swept from 800 MHz to 4 GHz (measurement bandwidth of 3200 MHz), corresponding to a resolution of $(3200\ \mathrm{MHz})^{-1}$ = 0.31 ns in the delay domain or a path resolution of $c \cdot 0.31$ ns = 9.4 cm (where c is the speed of light in free space). The wireless channel was probed at 801 points in the measured frequency range. This implies a separation of 4 MHz between two adjacent frequency points, giving a maximum resolvable time delay of $(4\ \mathrm{MHz})^{-1}$ = 250 ns or a path delay of $c \cdot 250$ ns = 75 m. Because the measurement bandwidth is large, the channel is frequency-selective over this bandwidth. This means that the measured CIRs include both the effects of multipath propagation and of channel frequency-selectivity. The latter effect causes a widening of the basic pulse shape in the delay domain, a phenomenon which is

not present in narrowband CIRs [7]. Prior to transmission, the swept-frequency signal generated by the network analyzer is amplified by an amplifier of type Amplifier Research 5S1G4. Omnidirectional, vertically polarized broadband antennas of type European Antennas XPO2V-0.3-10.0/1381 were used for both the transmitting antenna (Tx) and the receiving antenna (Rx). In the frequency range of interest, these antennas have a gain of 2 dBi and a 3 dB elevation beamwidth of 65°. Fig. 4.2 shows the measurement setup schematically.

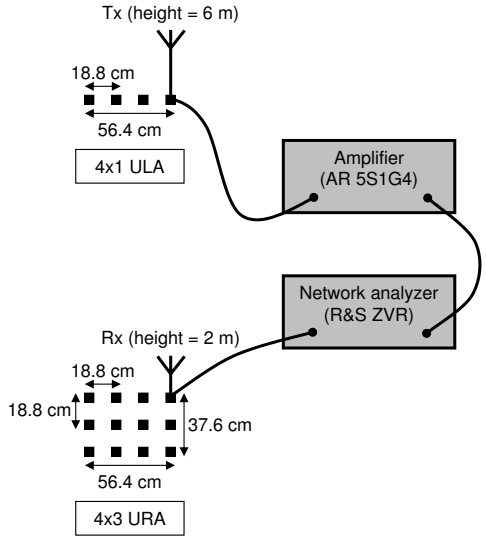

Figure 4.2: Measurement setup

4.2.3 Virtual array method

The CIR was measured using the virtual antenna array method, in order to allow analysis of SSF between elements of the virtual array [6]. In an area where Large-Scale Fading (LSF) is roughly constant, both the Tx and the Rx were moved between successive measurements to create the virtual antenna array. The Tx was shifted along a Uniform Linear Array (ULA) consisting of 4 elements. On the other end, the Rx was moved along a Uniform Rectangular Array (URA) made of 4x3 = 12 elements (see Fig. 4.2). Thus, the virtual antenna array allows for a total of 48 combinations of Tx and Rx positions. To promote independent fading at the different elements of the virtual array, the minimum spacing between two elements was chosen equal to 18.8 cm, which corresponds to half a wavelength at the lowest measurement frequency of 800 MHz. These choices for the virtual antenna array were made in agreement with [8], where some 50 measurement points spaced half

a wavelength or more apart are considered necessary for the determination of SSF.

Measurements were conducted with Tx and Rx heights equal to 6 m and 2 m above ground level, respectively. In total, the virtual antenna array was moved to 10 locations with different LSF in different industrial halls. Thus, the measured data pool contains 10 times 48 or 480 samples of the industrial CIR. The locations consist of 5 Line Of Sight (LOS) locations in LSF topography 1 and 5 OBstructed line of Sight (OBS) locations in LSF topography 2, and cover distances of 10 to 35 m between the transmitter and the receiver end.

4.2.4 Channel time-invariance

A basic requirement for frequency-domain channel sounding is that the channel remains time-invariant during the measurement time. In other words, the multipath profile should not be disrupted by motion taking place in the environment during the time the 48 combinations of Tx and Rx positions in the virtual array are scanned. This condition is not self-evident: measurements were performed during regular working hours when various sources of motion (e.g., workmen, machinery, fork-lift trucks) were present. Scanning all 48 elements of the virtual array approximately takes an hour, therefore it was checked whether a time-invariant channel can be guaranteed within this time frame. To investigate this, 20 measurements of the channel transfer function $\mathcal{H}(f)$ were performed at regular 3 minute time intervals for a fixed location of the Tx and the Rx. These measurements were done in OBS conditions for a Tx-Rx separation of 26 m.

Following, the correlation coefficient between each of the 20 frequency responses and the first frequency response is calculated [9]. Results for the correlation coefficient are shown in Fig. 4.3. Fig. 4.3 shows a very high correlation coefficient (> 0.96) between each frequency response and the first one. This indicates that, for a time frame of an hour, the channel is not easily disturbed by motion or changes in the physical layout of the environment. A similar conclusion could also be expected from the Temporal Fading (TF) measurements performed in Chapter 2. The measured production rooms in this chapter can be categorized under TF topography 2 (partially automated production line). In Chapter 2, temporal fading in TF topography 2 was shown to be Ricean with high K-factors which average to about 14 dB. The large value of these K-factors points to limited temporal variability of signal levels in the measured rooms, which renders these environments suitable for frequency-domain channel sounding.

4.2.5 Calculation of power delay profiles

Between the a-th element of the Tx array ($a = 1, \ldots, 4$) and the b-th element of the Rx array ($b = 1, \ldots, 12$), the complex channel transfer function $\mathcal{H}(f, a, b)$

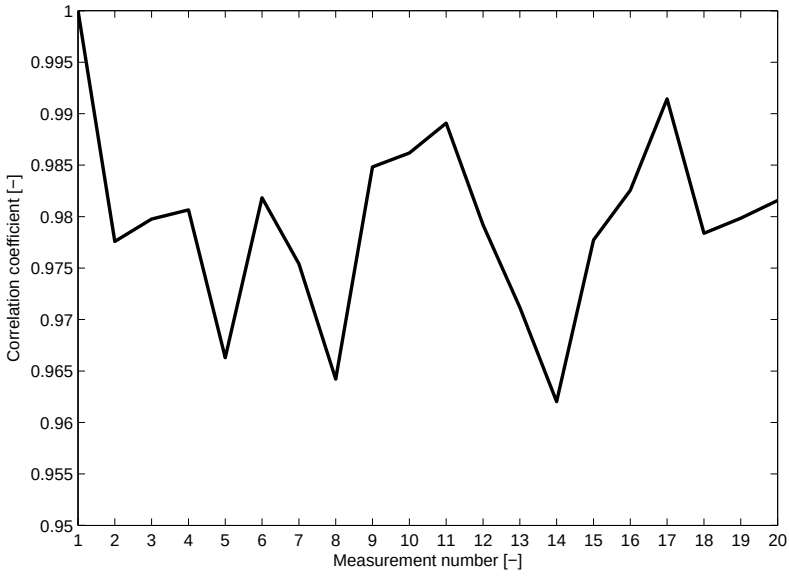

Figure 4.3: Correlation coefficient between 20 measurements of the channel frequency response and the first measurement to validate a time-invariant channel

is measured and converted to the delay domain using an Inverse Discrete Fourier Transform (IDFT) algorithm. Before applying the IDFT, the channel transfer function is multiplied by a Hann window $\mathrm{hann}\,(f)$ [4]. In the delay domain, the Hann window reduces leakage of the power in a delay bin to adjoining delay bins, compared to no windowing. This lessens a possible smearing effect of the delay bin powers, and helps to ascertain that the delay bin power can be attributed solely to the MPCs which effectively arrive within that delay bin. After conversion to the delay domain, the power delay profile $\mathrm{PDP}\,(\tau, a, b)$ as a function of delay τ is calculated as the squared magnitude of the CIR:

$$\mathrm{PDP}\,(\tau, a, b) = \left|\mathrm{IDFT}\left[\mathcal{H}\,(f, a, b) \times \mathrm{hann}\,(f)\right]\right|^2 \tag{4.1}$$

Next, the 48 PDPs constructed according to (4.1) are linearly averaged to form an Averaged Power Delay Profile (APDP). Prior to averaging, work in literature has suggested to shift the delay axis of $\mathrm{PDP}\,(\tau, a, b)$ in such a manner that the first arriving MPC falls within the same delay bin for all a and b [4, 10]. This procedure counters a possible spatial smearing effect, i.e., a phenomenon where MPCs, which should be found in only one delay bin, are instead present in several delay bins close together in the delay domain. This adjustment of the delay axis of $\mathrm{PDP}\,(\tau, a, b)$ is also done for our measurements, because a spatial smearing effect could be significant in our data. In Section 4.2.2, our measurement setup implies

a path resolution of 9 cm, while the smallest spacing between two elements of the virtual array is greater at 18.8 cm. Therefore, it is conceivable that the same physical MPC falls within different delay bins when the antennas are moved along the virtual array. The shift of the delay axis is done manually: $\mathrm{PDP}\,(\tau, a, b)$ is plotted for all a en b, and the PDPs are circularly shifted so that the first strong component of all PDPs presents itself within the same delay bin.

4.3 Modelling

4.3.1 Saleh-Valenzuela model

4.3.1.1 Description of the model

The main assumption of the SV model is the arrival of MPCs within several distinctly recognizable clusters [5]. In the SV model, the complex CIR $h(\tau)$ as a function of delay τ is given as:

$$h(\tau) = \sum_{l=0}^{\infty} \sum_{k=0}^{\infty} \beta_{kl} \exp(j\theta_{kl}) \cdot \delta(\tau - T_l - \tau_{kl}) \tag{4.2}$$

In (4.2), β_{kl} and θ_{kl} are the amplitude gain and phase of the k-th ray in the l-th cluster, respectively. The parameters T_l and τ_{kl} are the arrival times of l-th cluster and the k-th ray in the l-th cluster (measured from the time the cluster starts), respectively, and $\delta(\cdot)$ denotes the Dirac delta function. In the SV model, the LSF power gain $\overline{\beta_{kl}^2}$, i.e. the power gain β_{kl}^2 averaged over an area where large-scale fading remains unchanged, is modelled as a double exponential decay as function of delay:

$$\overline{\beta_{kl}^2} = \overline{\beta_{11}^2} \cdot \exp\left[\frac{-T_l}{\Gamma}\right] \exp\left[\frac{-\tau_{kl}}{\gamma_l}\right] \tag{4.3}$$

In (4.3), Γ is the cluster power decay constant, γ_l is ray power decay constant for cluster l, and $\overline{\beta_{11}^2}$ denotes the averaged power gain of the first arriving ray of the CIR. Furthermore, the model assumes that clusters and rays within clusters arrive according to a stochastic Poisson process. This means that the interarrival times of clusters and rays obey exponential rate laws:

$$p_{\exp}(T_l \mid T_{l-1}) = \Lambda \exp\left[-\Lambda (T_l - T_{l-1})\right] \tag{4.4}$$

$$p_{\exp}\left(\tau_{kl} \mid \tau_{(k-1)l}\right) = \lambda \exp\left[-\lambda \left(\tau_{kl} - \tau_{(k-1)l}\right)\right] \tag{4.5}$$

In (4.4), $p_{\exp}(T_l \mid T_{l-1})$ is the conditional probability of a cluster arriving at time T_l when the last cluster started at time T_{l-1}. Analogously in equation (4.5),

$p_{\exp}\left(\tau_{kl} \mid \tau_{(k-1)l}\right)$ refers to the conditional probability of a ray arriving at time τ_{kl}, given the previous ray arrived at time $\tau_{(k-1)l}$. The parameters Λ and λ are the cluster and ray arrival rate, respectively.

4.3.1.2 Extraction of the model's parameters

The parameters of the SV model (the decay constants Γ and γ_l, and the arrival rates Λ and λ) constitute large-scale fading parameters. Hence, their values are extracted from the APDPs. Fig. 4.4 shows an APDP of a LOS measurement for a separation of 10 m between the Tx and the Rx. The origin of the delay axis is set to the delay of the first arriving MPC, and the received power is normalized to the power of the first component. The normalized power is displayed in dB, and the delay in ns.

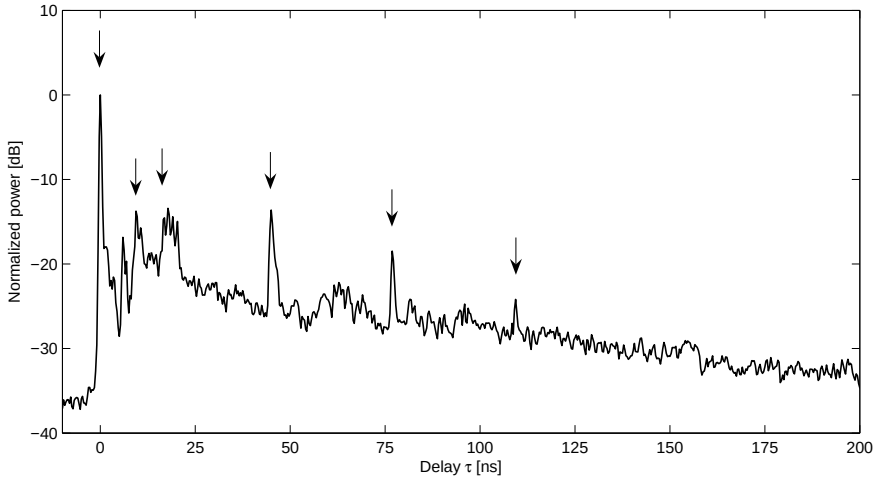

Figure 4.4: APDP for a 10 m LOS measurement (the arrows indicate the onset of a new cluster)

In Fig. 4.4, several clearly identifiable clusters can be distinguished. This confirms the practicability of the SV model for describing the power delay profile in this case. For our measurements, the onsets of individual clusters are determined through visual inspection of the APDP: the start of new cluster is marked by a visually well detectable rise of received power. In Fig. 4.4, six easily recognizable rises of received power can be spotted, as pointed to by arrows. Following cluster detection, the parameters of the SV model in (4.3)-(4.5) are extracted from each APDP. The model's parameters are calculated as follows:

1. *Ray power decay constant γ_l:* For a certain cluster l, the exponential relationship between (linear) power and delay in (4.3) translates into a linear de-

pendence when the received power is considered on a logarithmic dB-scale. Hence, the ray power decay constant γ_l can be determined by performing a linear regression (in a least-squares sense) of received power in dB as a function of delay. This procedure is visualized in Fig. 4.5, which shows an APDP of a OBS measurement for 20 m Tx-Rx separation. Seven clusters could be identified for this measurement, and the linear regressions of logarithmic power within each individual cluster are represented as solid straight lines (intra-cluster in Fig. 4.5). For cluster l, the slope s_l of the regression line is considered and converted to the exponential ray power decay constant γ_l, using:

$$\gamma_l = -\frac{10}{\ln(10)\, s_l} \tag{4.6}$$

2. *Cluster power decay constant* Γ*:* Similar to the ray power decay constant, the cluster power decay constant Γ can be determined by performing a linear regression with dependent variable the peak cluster power in dB, and independent variable the delay of the peak powers. This linear regression is done for peak powers gathered from several APDPs at once, so attention must be given to the different total power of each APDP (which is due to distance-dependent large-scale fading). Therefore, all linear delay bin powers are normalized to the power in the first delay bin, and the delay axis is adjusted so that the first cluster starts at a delay of 0 ns. The slope S following from the linear regression can then be turned into the cluster power decay constant Γ by doing a conversion similar to formula (4.6):

$$\Gamma = -\frac{10}{\ln(10)\, S} \tag{4.7}$$

   As an example, the dashed straight line in Fig. 4.5 shows linear regression performed on the logarithmic cluster peak powers of only the shown APDP (inter-cluster in Fig. 4.5).

3. *Ray arrival rate* λ*:* From typical APDPs such as the one in Fig. 4.4, it is clear that individual MPCs cannot be isolated due to the limited time resolution of our measurements (0.31 ns). Each delay bin or ray contains an appreciable amount of power. **For this reason, what constitutes as a "ray" in this chapter is in fact the vector summation of multiple MPCs with about the same delay, all falling within the same delay bin.** The SV model in equations (4.2)-(4.5) is thus interpreted as a classical tapped delay line model: delay taps are assumed to arrive at regular time intervals of 0.31 ns, or, in other words, at rate λ equal to $(0.31\ \text{ns})^{-1}$ = 3.23 GHz.

4. *Cluster arrival rate* Λ*:* To determine the cluster arrival rate Λ, the cluster interarrival times $\Delta T_l = T_l - T_{l-1}$ are considered. As the ΔT_l are assumed to

follow an exponential distribution (formula (4.4)), a Maximum Likelihood Estimator (MLE) $\hat{\Lambda}$ of the rate parameter Λ can be calculated as:

$$\hat{\Lambda} = 1/\overline{\Delta T_l} \tag{4.8}$$

In (4.8), $\overline{\Delta T_l}$ denotes the arithmetic mean of ΔT_l samples for a single APDP or several APDPs within a specified scenario, e.g., LOS or OBS situation.

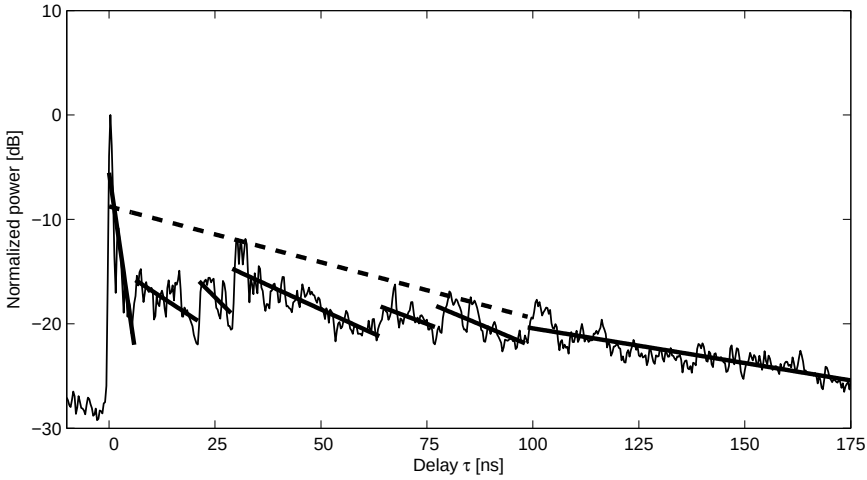

Figure 4.5: Averaged power delay profile for a 20 m OBS measurement with modelled intra-cluster and inter-cluster power decays

4.3.2 Small-scale fading

In this section, we elaborate on a methodology to investigate small-scale amplitude fading. In literature, small-scale amplitude fading has been shown to agree with certain statistical distributions, e.g., Nakagami-m for measurements in a modern office building in [10], Nakagami-m and Rayleigh for measurements in industrial environments in [4], and lognormal for indoor near-ground measurements in [11]. To determine the most suitable distribution of SSF samples for our measurements, the 48 small-scale PDPs used to construct each large-scale APDP are considered. In the following, each of the small-scale PDPs associated with a single APDP is assigned a serial number $i = 1, \ldots, q$, where $q = 48$. Then, for each delay bin j, it is investigated if the amplitude gains c_{ij} of the 48 small-scale PDPs are most likely drawn from a Nakagami-m, a Rayleigh, or a lognormal distribution. Formulas (4.9), (4.10), and (4.11) show the Probability Density Functions (PDFs)

of the Nakagami-m (parameters Ω_j and m_j), Rayleigh (parameter $\sigma_{\mathrm{rayl},j}$), and lognormal (parameters $\mu_{\mathrm{logn},j}$ and $\sigma_{\mathrm{logn},j}$) distributions, respectively.

$$p_{\mathrm{nak}}\left(c_{ij}\ ;\ \Omega_j, m_j\right) = \frac{2}{\mathrm{Gamma}\left(m_j\right)}\left(\frac{m_j}{\Omega_j}\right)^{m_j} c_{ij}^{2m_j-1}\exp\left[-\frac{m_j c_{ij}^2}{\Omega_j}\right] \tag{4.9}$$

$$p_{\mathrm{rayl}}\left(c_{ij}\ ;\ \sigma_{\mathrm{rayl},j}\right) = \frac{c_{ij}}{\sigma_{\mathrm{rayl},j}^2}\exp\left[-\frac{c_{ij}^2}{2\sigma_{\mathrm{rayl},j}^2}\right] \tag{4.10}$$

$$\begin{aligned} p_{\mathrm{logn}}\left(\ln\left(c_{ij}\right)\ ;\ \mu_{\mathrm{logn},j}, \sigma_{\mathrm{logn},j}\right) = {} & \frac{1}{\sqrt{2\pi\sigma_{\mathrm{logn},j}^2}} \\ & \cdot \exp\left[-\frac{\left(\ln\left(c_{ij}\right)-\mu_{\mathrm{logn},j}\right)^2}{2\sigma_{\mathrm{logn},j}^2}\right] \end{aligned} \tag{4.11}$$

In (4.9), $\mathrm{Gamma}\left(\cdot\right)$ is the Gamma function. The parameters characterizing each of these three distributions are estimated in a maximum-likelihood manner. MLEs are chosen because they will permit the use of likelihood ratio tests for selecting the best fit distribution.

- For the Nakagami-m distribution and for delay bin j, the MLEs $\hat{\Omega}_j$ of the scale parameter Ω_j and $\hat{m}_j$ of the shape parameter m_j are calculated as derived in [12]:

$$\hat{\Omega}_j = \frac{1}{q}\sum_{i=1}^{q} c_{ij}^2, \tag{4.12}$$

$$\hat{m}_j = \frac{6+\sqrt{36+48\Delta_j}}{24\Delta_j}, \tag{4.13}$$

  where,

$$\Delta_j = \ln\left(\frac{\frac{1}{q}\sum_{i=1}^{q} c_{ij}^2}{\left(\prod_{i=1}^{q} c_{ij}^2\right)^{\frac{1}{q}}}\right) \tag{4.14}$$

- For the Rayleigh distribution and for delay bin j, the MLE $\hat{\sigma}_{\mathrm{rayl},j}$ of the distribution's parameter $\sigma_{\mathrm{rayl},j}$ is given as:

$$\hat{\sigma}_{\mathrm{rayl},j} = \sqrt{\frac{1}{2q}\sum_{i=1}^{q} c_{ij}^2} \tag{4.15}$$

- For the lognormal distribution and for delay bin j, the MLE $\hat{\mu}_{\mathrm{logn},j}$ ($\hat{\sigma}_{\mathrm{logn},j}$) of the distribution's mean $\mu_{\mathrm{logn},j}$ (standard deviation $\sigma_{\mathrm{logn},j}$) is given by the

mean (standard deviation) of the $\ln(c_{ij})$ samples:

$$\hat{\mu}_{\mathrm{logn},j} = \frac{1}{q}\sum_{i=1}^{q}\ln(c_{ij}) \tag{4.16}$$

$$\hat{\sigma}_{\mathrm{logn},j} = \sqrt{\frac{1}{q-1}\sum_{i=1}^{q}\left(\ln(c_{ij}) - \hat{\mu}_{\mathrm{logn},j}\right)^2} \tag{4.17}$$

In order to identify the statistical distribution which provides the best fit to the amplitude gains in delay bin j, Likelihood Ratio Tests (LRTs) are performed.

4.3.2.1 Nakagami-m versus Rayleigh

Firstly, the possibility of a Nakagami-m or Rayleigh distribution for the amplitude gains is investigated. For delay bin j, the likelihood ratio ξ_j is constructed:

$$\xi_j = \frac{f_{\mathrm{rayl}}\left(c_{1j},\ldots,c_{qj} \mid \hat{\sigma}_{\mathrm{rayl},j}\right)}{f_{\mathrm{nak}}\left(c_{1j},\ldots,c_{qj} \mid \hat{\Omega}_j, \hat{m}_j\right)} \tag{4.18}$$

In (4.18), $f_{\mathrm{rayl}}(\cdot)$ and $f_{\mathrm{nak}}(\cdot)$ denote the likelihood functions of the Rayleigh and the Nakagami-m distributions, respectively. For example for the Rayleigh distribution, the likelihood function is calculated as:

$$f_{\mathrm{rayl}}\left(c_{1j},\ldots,c_{qj} \mid \hat{\sigma}_{\mathrm{rayl},j}\right) = \prod_{i=1}^{q} p_{\mathrm{rayl}}\left(c_{ij}\,;\,\hat{\sigma}_{\mathrm{rayl},j}\right) \tag{4.19}$$

Through the fact that Rayleigh is merely a special case of Nakagami-m, with its shape parameter m set to 1, Nakagami-m always provides a better fit to the data compared to Rayleigh (i.e., $0 < \xi_j < 1$). Therefore, a Rayleigh distribution can never be preferred to a Nakagami-m distribution. However, it can be checked whether it is *reasonable* to exchange the complicated Nakagami-m model for the simple Rayleigh model. An often used LRT states that the assumption to use the simple Rayleigh model for delay bin j can be accepted at a 5% significance level, if [13]:

$$-2\ln\xi_j < \chi^2_{0.95;1} = 3.84 \tag{4.20}$$

In (4.20), $\chi^2_{0.95;1}$ is the 95th percentile of a chi-square distribution with one degree of freedom.

4.3.2.2 Rayleigh versus lognormal

Secondly, it is investigated if a Rayleigh distribution for the amplitude gains could possibly be traded in for a lognormal distribution. For delay bin j, the likelihood ratio ψ_j is calculated:

$$\psi_j = \frac{f_{\text{rayl}}\left(c_{1j}, \ldots, c_{qj} \mid \hat{\sigma}_{\text{rayl},j}\right)}{f_{\text{logn}}\left(c_{1j}, \ldots, c_{qj} \mid \hat{\mu}_{\text{logn},j}, \hat{\sigma}_{\text{logn},j}\right)} \tag{4.21}$$

In (4.21), $f_{\text{logn}}(\cdot)$ denotes the likelihood function of the lognormal distribution. Because the Rayleigh distribution is not a degenerate case of the lognormal distribution or vice versa, a criterion for distribution selection similar to inequality (4.20) cannot be used for ψ_j. Instead, a Rayleigh distribution is considered more suitable for delay bin j if $\psi_j > 1$ [13].

4.3.3 RMS delay spread

The Root Mean Square (RMS) delay spread is an often used parameter which quantifies the amount of time dispersion of the received power. For each APDP, the RMS delay spread is calculated as the second central moment of the powers of each delay bin. If $\text{APDP}(\tau_j)$ is the averaged received power sampled at delay instance τ_j, then the RMS delay spread τ_{rms} follows as [14]:

$$\tau_{\text{rms}} = \sqrt{\frac{\sum_j \text{APDP}(\tau_j) \cdot \tau_j^2}{\sum_j \text{APDP}(\tau_j)} - \left(\frac{\sum_j \text{APDP}(\tau_j) \cdot \tau_j}{\sum_j \text{APDP}(\tau_j)}\right)^2} \tag{4.22}$$

4.4 Results

Results of the industrial CIR modelling are discussed in the following. A summary of the proposed models is found in Table 4.1 on page 94.

4.4.1 Saleh-Valenzuela model

For each of the measured APDPs, the number of clusters found by visual inspection varies between 6 and 8. For all APDPs together, a total of 66 clusters are considered for the determination of the SV model parameters. These clusters arrive at delays up to 120 ns relative to the arrival time of the first cluster. In the following, numerical values and models for the SV parameters are discussed.

4.4.1.1 Ray power decay constant γ_l

Firstly, we remark that the intra-cluster power decay is well described by the exponential law proposed in the SV model. This was validated by performing the

linear regression of logarithmic power as function of delay within each cluster of the APDP, and by subsequently calculating the coefficient of determination of all linear fits combined. The coefficient of determination associated with each APDP varied between 0.74 and 0.91, and was 0.82 on average. This means that, on average, 82% of the variance of logarithmic received power is explained by the fitted linear decays in each cluster. This high percentage asserts that a simple exponential decay model for linear power within each cluster is well-suited for the accurate characterization of the APDP.

The original SV model proposes a ray power decay constant γ_l which remains the same for all clusters of an APDP [5]. However, measurements in industrial facilities have shown that γ_l seems to increase with delay in these environments: a linear dependence between γ_l and delay τ was proposed in [4]. To make a comparison of ray power decays possible between different APDPs, the delay of a cluster with power decay γ_l is defined as the arrival time of that cluster relative to the arrival time of the first cluster within the same APDP (i.e., $T_l - T_1$ for cluster l in (4.2)). Measured ray power decay constants γ_l vary between 1.2 and 65.3 ns, which is comparable to values between 0.5 and 70 ns found in [4].

With respect to [4], we suggest a few alterations to the modelling of γ_l versus delay. Firstly, the intra-cluster decay γ_l only assumes positive values. To promote normality of the deviations between measured ray power decay and a linear model, $\ln(\gamma_l)$ is used as dependent variable in the model, because both positive and negative values of $\ln(\gamma_l)$ can then be meaningful. Normality of deviations is preferable, as this assumption allows of the calculation of CIs and the execution of hypothesis tests for the significance of certain parameters in the model. Secondly, whether the power decay constant arises from a cluster following from a LOS or an OBS measurement is encoded in the model as a dummy variable V: V equals 0 for LOS and 1 for OBS. A linear relationship between dependent variable $\ln(\gamma_l)$ and independent variables V and delay τ is proposed:

$$\ln(\gamma_l) = \alpha_0 + \alpha_1 \cdot \tau + \alpha_2 \cdot V + \alpha_3 \cdot \tau \cdot V + \epsilon \tag{4.23}$$

The parameters α_0 to α_3 in (4.23) are determined through linear regression. The parameters α_0 and α_1 represent the intercept and the slope of the regression between $\ln(\gamma_l)$ and τ, while α_2 and α_3 account for changes in the value of the intercept and the slope between LOS and OBS situations. Furthermore, ϵ is a random variable expressing the errors between the measured $\ln(\gamma_l)$ samples and the linear model in $\alpha_0, \ldots, \alpha_3$. Fig. 4.6 shows 66 measured samples of $\ln(\gamma_l)$ as a function of their associated relative cluster delay for clusters of all measured APDPs, without distinguishing between LOS or OBS measurements.

The model in (4.23) is further refined through backward elimination: t-tests were carried out on $\alpha_0, \ldots, \alpha_3$ to determine which of these regression parameters

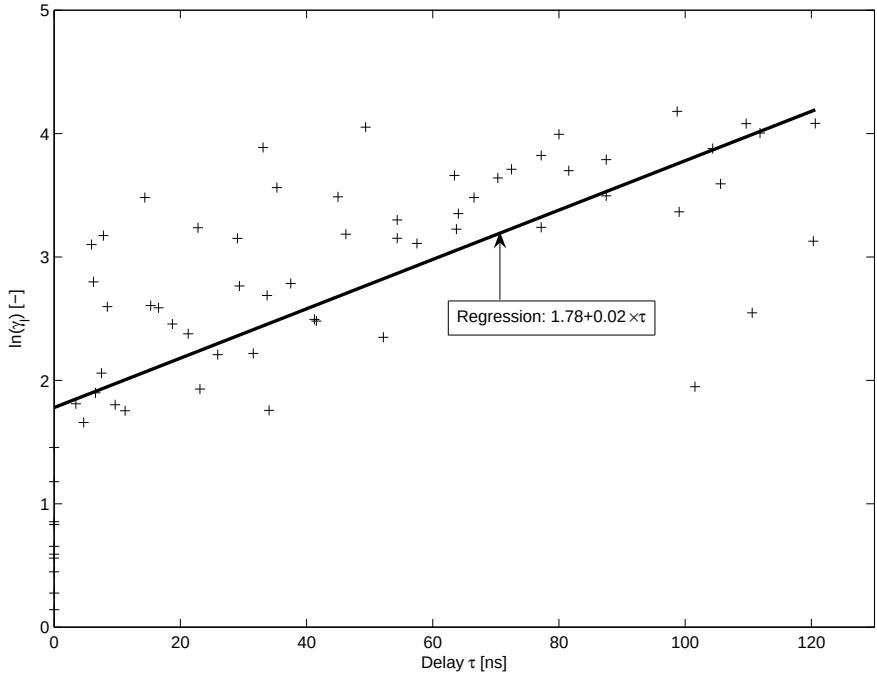

Figure 4.6: Samples of $\ln(\gamma_l)$ of the clusters of all APDPs versus relative cluster delay τ

are not significant at a 5% significance level, i.e., which parameters can assumed to be zero [13]. At each step of the backward elimination process, normality of the errors ϵ (and thus the validity of the t-tests) is confirmed by a Kolmogorov-Smirnov (KS) test at a 5% significance level. The t-tests showed that α_2 and α_3 can be dropped from the model in (4.23) at convincingly high p-values greater than 0.4. Inspecting (4.23), this means that the regression between $\ln(\gamma_l)$ and τ does not depend on LOS or OBS circumstances. Furthermore, the remaining regression parameters α_0 and α_1 prove to be significant at p-values less than 10^{-4}. Numerically, this statistical analysis allows us to formulate the following simple model for $\ln(\gamma_l)$, which does not depend on LOS or OBS (also see regression line in Fig. 4.6):

$$\ln(\gamma_l) = 1.78 + 0.02 \cdot \tau + 0.76 \cdot Z \tag{4.24}$$

In (4.24), Z is a standard normally distributed random variable, and γ_l and τ are in units of ns. We note that $0.76^2 = 0.58$ is the estimated variance of the error term ϵ, while for the model's simplicity, the uncertainty inherent to the estimation of α_0 and α_1 is not accounted for. The variance of the regression line in Fig. 4.6 was found to be maximally 0.04 in the available range of cluster delays, which

we neglect with respect to 0.58. Furthermore, the correlation coefficient between $\ln(\gamma_l)$ and τ equals 0.71, which highlights a sufficiently strong linear component in the relationship between these two variables.

4.4.1.2 Cluster power decay constant Γ

The cluster power decay constant Γ is determined by performing linear regression between the cluster peak powers P_{peak} in dB and their associated delays τ in ns. For this linear regression, all clusters of all APDPs are considered simultaneously: the data of each APDP is scaled so that the peak power of the first cluster equals 0 dB and occurs at 0 ns (see Section 4.3.1.2). According to the theoretical double exponential decay in (4.3), $P_{peak} = 10\log(\exp(-\tau/\Gamma))$. As for the ray power decay, possible differences between LOS and OBS clusters are accounted for by incorporating the dummy variable V in the regression. Thus, the following linear model is considered:

$$P_{peak} = \delta_1 \cdot \tau + \delta_2 \cdot \tau \cdot V + \epsilon' \tag{4.25}$$

In (4.25), the regression parameter δ_1 relates to the exponential decay constant Γ, δ_2 accounts for a possible change in Γ between LOS and OBS situations, and ϵ' expresses the error between observations of the peak power and the linear model in δ_1 and δ_2. A t-test shows that, with a p-value of 0.11, regression parameter δ_2 does not significantly differ from zero at a 5% significance level. On the other hand, parameter δ_1 is significant with a p-value less than 10^{-4}. As for the ray power decay in Section 4.4.1.1, the peak cluster power decay does not seem to depend on LOS or OBS circumstances. Next, when omitting δ_2 from the linear model in (4.25), linear regression estimates δ_1 at -0.20. The 95% CI for the true value of δ_1 is $[-0.23, -0.17]$. Normality of errors ϵ' was confirmed by a KS test at a 5% significance level.

A value of -0.20 for δ_1 is equivalent to a value of 21.87 ns for the exponential decay constant Γ (formula (4.7) with $S = \delta_1$). The 95% CI for the true value of Γ is $[18.89\text{ ns}, 25.98\text{ ns}]$. This result agrees well with Γ values between 13 and 30 ns previously found for measurements in industrial environments in [4], in spite of the overall lower antenna heights in [4] compared to our setup.

For the model in (4.25) without δ_2, it should be noted that the standard deviation of the error term ϵ' amounts to 7.37 dB. Fig. 4.7 shows 66 samples of cluster peak power P_{peak} versus cluster delay τ, together with the fitted linear regression line. Although a linear decrease of logarithmic peak power with delay can be accepted (the coefficient of determination for the fitted linear model equals 0.71), Fig. 4.7 also shows a noticeable contribution of the error term ϵ' to the cluster peak power. Therefore, we propose to let the peak power P_{peak} not only depend on δ_1 (or Γ), but also to include a normally distributed error term in the linear model:

$$P_{peak} = -0.20 \cdot \tau + 7.37 \cdot Z \tag{4.26}$$

In (4.26), we remark that $7.37^2 = 54.32$ is the estimated variance of ϵ'. Again, the variance of the regression line in Fig. 4.7, equal to 3.61, is neglected with respect to 54.32 to retain a simpler model. In Table 4.1 on page 94, both the exponential cluster power decay constant Γ according to the classical SV model and the newly proposed model for P_{peak} are shown.

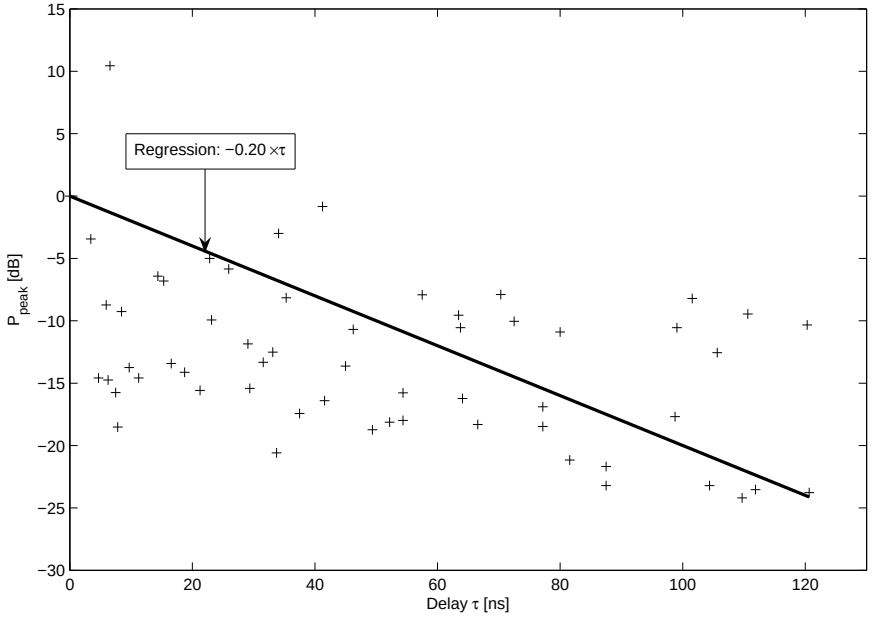

Figure 4.7: Samples of P_{peak} of the clusters of all APDPs versus delay τ

4.4.1.3 Cluster arrival rate Λ

The cluster arrival rate Λ is determined separately for LOS and OBS measurements. For LOS measurements, 29 interarrival times ΔT_l of five different APDPs are considered. The mean interarrival time $\overline{\Delta T_l} = 1/\hat{\Lambda}$, with $\hat{\Lambda}$ the MLE of Λ in (4.4), equals 19.55 ns for the LOS clusters. For OBS measurements, 27 interarrival times ΔT_l of five different APDPs are determined. For the OBS clusters, the mean interarrival time $\overline{\Delta T_l}$ is equal to 17.16 ns.

The mean cluster interarrival times $\overline{\Delta T_l}$ for LOS measurements (19.55 ns) and for OBS measurements (17.16 ns) do not seem to differ much. In this perception, a two-sample KS test was performed between the observations of ΔT_l grouped

according to LOS or OBS circumstances. For this test, the null hypothesis that the observations of ΔT_l following from LOS and OBS measurements separately are drawn from the same distribution could not be rejected at a 5% significance level (p-value = 0.43). For LOS and OBS considered together, the mean interarrival time $\overline{\Delta T_l}$ is found to be 18.40 ns. A chi-squared goodness-of-fit test retained the null hypothesis that the arrival times of both LOS and OBS clusters together are drawn from an exponential distribution at a 5% significance level (p-value = 0.08). The p-value indicates that exponentiality is just accepted. This could be partly due to the fact that accurate cluster arrival times are difficult to obtain: clusters are identified in a visual, and therefore more or less subjective, manner.

Fig. 4.8 shows the empirical probability density function or PDF of the cluster interarrival times of both LOS and OBS measurements. A solid line also shows the theoretical PDF of an exponential distribution with estimated mean interarrival time of 18.40 ns. From Fig. 4.8, the cluster interarrival times could reasonably be assumed to be exponentially distributed.

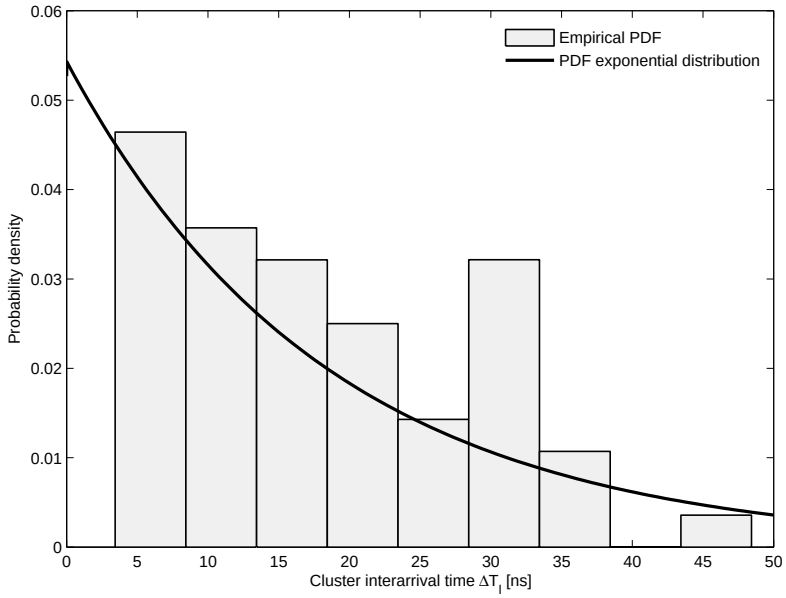

Figure 4.8: Empirical PDF and estimated exponential PDF for the interarrival times of all APDPs

For measurements in industrial environments in [4], mean cluster interarrival times $\overline{\Delta T_l}$ between 13 and 16 ns are found, which are comparable to our obtained value of 18.40 ns. In literature, when comparing industrial environments to office environments, clusters usually arrive further in between in the latter: $\overline{\Delta T_l}$ = 60 ns

for measurements in a university building in [15], and $\overline{\Delta T_l}$ is 27 ns for LOS and 40 ns for OBS measurements in an office building in [16]. This would mean that in office environments, groups of reflective objects (where objects within a group give rise to multipath reflections within the same APDP cluster) are spatially more separated. Because the inventory in industrial environments (machinery, transport belts, steel piping) is more irregularly shaped, more clusters in rapid succession are expected to be found in these environments. Also, in contrast to office environments, the inventory in industrial environments largely consists of highly reflective metal surfaces [4, 17]. In industrial halls, more objects are therefore expected to actively participate in the wave propagation while giving rise to noticeable received powers at the receiver's end. This means that more clusters could be detected in industrial halls when compared to office buildings.

4.4.2 Small-scale fading

In this section, the statistical distribution of the amplitude gains within each delay bin is determined according to the procedure put forward in Section 4.3.2. In the following, it is investigated whether a Nakagami-m, a Rayleigh, or a lognormal distribution provides a better fit to the experimental data.

4.4.2.1 Nakagami-m versus Rayleigh

For all measured APDPs, it was found that at least 89% of delay bins j satisfy inequality (4.20): a Rayleigh distribution therefore proves to be an adequate fit for the amplitude fading within each delay bin. However, for the *first* delay bin of each APDP, the LRT in (4.20) consistently failed. A distinctly non-Rayleigh character for the first delay bin can also be seen in Fig. 4.9, which shows the MLEs (4.13) of the Nakagami m parameter as function of bin delay for a LOS measurement at 15 m Tx-Rx separation. For the first delay bin in Fig. 4.9, $\hat{m}_1 = 26.5$ shows that Rayleigh fading for the amplitude gains cannot be assumed. For the subsequent delay bins however, the $\hat{m}_j$ with $j > 1$ are notably closer to one, which points out that Rayleigh fading can be accepted for most of these delay bins.

4.4.2.2 Rayleigh versus lognormal

Based on the likelihood ratio in (4.21) and for all measured APDPs, a Rayleigh distribution is preferred to a lognormal distribution for at least 79% of the delay bins. This percentage may not seem convincingly high. However, it should be noted that the lognormal distribution has one degree of freedom more than the Rayleigh distribution. Hence, a lognormal distribution is already advantaged *prior* to performing the LRT. Summarizing, it may be stated that the Rayleigh distribution is most suitable to describe the amplitude gains in each delay bin with the

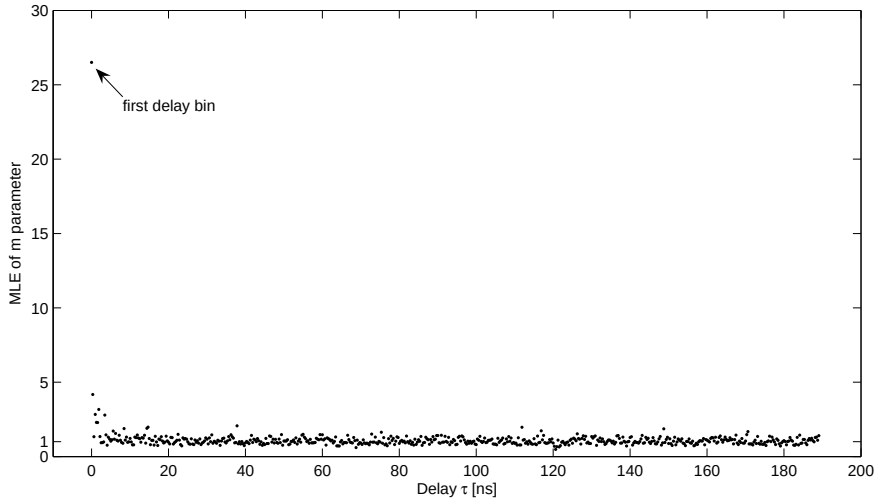

Figure 4.9: MLEs of the Nakagami-m parameter versus delay for a LOS measurement at 15 m

exception of the first delay bin, where Nakagami-m with $m \neq 1$ provides a better fit. This conclusion is in agreement with the results presented in [4].

Fig. 4.10 shows the empirical Cumulative Distribution Function (CDF) (solid line) of the amplitude gains in the first and the hundredth delay bin of the same measurement as in Fig. 4.9. The amplitude gains on the abscissa are expressed in arbitrary units. Also shown for delay bin 1 and for delay bin 100 are theoretical Nakagami-m and Rayleigh CDFs, respectively, with their parameters estimated in a maximum-likelihood manner from the amplitude gains in the respective delay bins. Fig. 4.10 shows that amplitude fading in the first delay bin is well described by a Nakagami-m distribution, while for delay bin 100, Rayleigh fading agrees well with the empirical fading distribution.

The fact that Rayleigh fading occurs instead of lognormal fading shows that enough MPCs arrive in one delay bin to hold the Central Limit Theorem (CLT). This can be explained by the abundance of (metal) scatterers in a typical industrial environment, which give rise to a multitude of paths arriving within one delay bin [4]. Also, because the MPCs in one delay bin have approximately the same path length, they can be expected to have undergone similar interactions with the environment, i.e. similar reflections and diffractions off the same surfaces. Therefore, the RMS power of these MPCs should be about the same, which explains why the amplitude distribution tends to Rayleigh rather than to Nakagami-m with $m \neq 1$. This is with the exception of the first delay bin, where amplitude fading is distinctly Nakagami-m and the CLT therefore does not hold. In LOS situa-

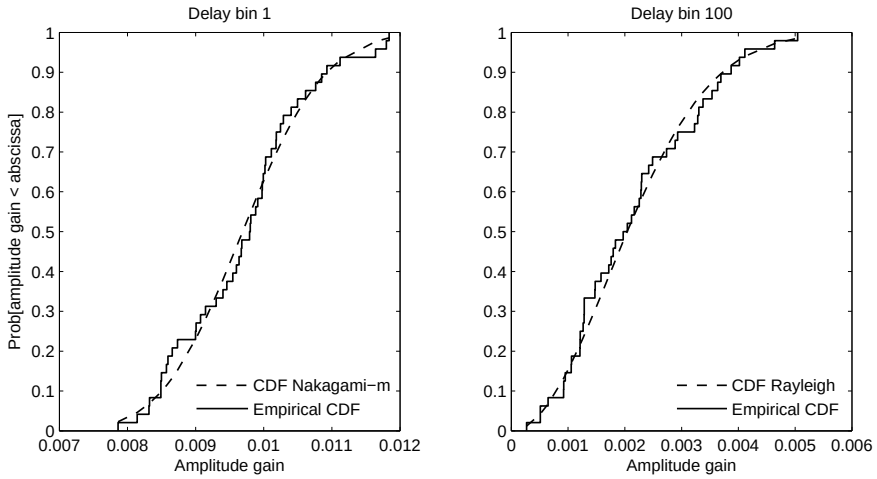

Figure 4.10: Empirical CDFs and estimated theoretical CDFs for the amplitude gains in delay bins 1 and 100 of a LOS measurement at 15 m

tions, the CLT may not hold because the RMS power of the LOS MPC exceeds the RMS power of the reflected paths (which also fall within the first delay) enough to cause Ricean fading. In OBS situations, the CLT may not hold because not enough MPCs arrive within the first delay bin.

4.4.3 RMS delay spread

For each APDP, the RMS delay spread τ_{rms} was calculated using (4.22). For LOS measurements, τ_{rms} varies between 41.37 ns and 48.51 ns. For OBS measurements, τ_{rms} ranges from 43.90 ns to 53.70 ns. Generally, these values are slightly higher than, but still comparable to values between 28 ns and 50 ns reported in [4]. This increase in RMS delay spread could possibly be attributed to the height difference between the Tx and the Rx in our measurements, whereas the Tx and the Rx in [4] are at the same height.

4.5 Conclusions

In this chapter, measurements of the CIR for indoor industrial environments have been presented. Measurements were performed through frequency-domain channel sounding (from 800 MHz to 4 GHz) and by using the virtual antenna array method. Stationarity of the wireless channel during measurements, which is required for this type of channel sounding, was validated through a statistical correlation analysis. Transmitting and receiving antenna heights were chosen equal to 6 m

Parameter	Model
exponential ray power decay constant γ_l [ns]	$\ln(\gamma_l) = 1.78 + 0.02 \cdot \tau + 0.76 \cdot Z$
ray arrival rate	*constant* interarrival time $= 0.31$ ns
exponential cluster power decay constant Γ [ns]	$\Gamma = 21.87$ ns
cluster peak power P_{peak} [dB]	$P_{peak} = -0.20 \cdot \tau + 7.37 \cdot Z$ first cluster: $P_{peak} = 0$ dB
cluster arrival rate	exponential with *averaged* interarrival time $\overline{\Delta T_l} = 18.40$ ns
small-scale amplitude fading	first delay bin: Nakagami-m other delay bins: Rayleigh
RMS delay spread τ_{rms} [ns]	LOS: $\tau_{\mathrm{rms}} = 41.37 - 48.51$ ns OBS: $\tau_{\mathrm{rms}} = 43.90 - 53.70$ ns

(τ [ns] = delay, Z = standard normally distributed variable)

Table 4.1: Power delay profile parameters and modelling (APDPs are assumed to start at 0 ns and have their powers normalized to the power of the first arriving component)

and 2 m, respectively, to imitate wireless communication between an access point near the ceiling of the industrial hall and a wireless client closer to the industrial processes.

The power delay profiles, averaged over an SSF area, were found to clearly exhibit clustering of received power as function of delay. Because of this, the well-known SV model for the averaged power delay profile was fitted to the measurement data. For our delay resolution of 0.31 ns, a significant amount of multipath energy was present in each delay bin. In this work, the SV model was therefore interpreted as a classical tapped delay line model with taps arriving at regular time intervals of 0.31 ns. For the parameters of the adapted SV model, results are summarized as follows:

- The ray power decay constant γ_l was found to be dependent on the delay of the corresponding cluster. A linear model between $\ln(\gamma_l)$ and delay τ with a normally distributed error term was proposed. A finding was that the parameters of the linear model do not significantly differ between LOS and OBS scenarios.
- The cluster power decay constant Γ was determined at 21.87 ns, and was found to be independent of LOS or OBS circumstances. A model for the cluster peak powers P_{peak} as a function of delay τ was presented.

- The mean cluster interarrival time $\overline{\Delta T_l}$ (i.e., the inverse of the cluster arrival rate Λ) equalled 19.55 ns and 17.16 ns for LOS and OBS clusters, respectively. The distribution of cluster interarrival times was found to be independent of LOS or OBS. For all clusters regardless of LOS or OBS, cluster interarrival times were determined to be exponentially distributed with $\overline{\Delta T_l}$ equal to 18.40 ns.
- Small-scale amplitude fading was found to be Rayleigh distributed for all delay bins except the first one. For the first delay bin, Nakagami-m fading provided a better fit.

Generally, the difference between LOS and OBS had only limited effect on the parameters of the SV model. The parameter's values were in the same range of those in literature of other measurements of the industrial CIR, despite the new antenna heights used in this study. Finally, the RMS delay spread τ_{rms} was investigated and found to range between 41.37 ns and 48.51 ns for LOS scenarios and between 43.90 ns to 53.70 ns for OBS scenarios.

References

[1] T. S. Rappaport. *Characterization of UHF Multipath Radio Channels in Factory Buildings*. IEEE Transactions on Antennas and Propagation, 37(8):3028–3037, August 1989.

[2] T. S. Rappaport, S. Y. Seidel, and K. Takamizawa. *Statistical Channel Impulse Response Models for Factory and Open Plan Building Radio Communication System Design*. IEEE Transactions on Communications, 39(5):794–807, May 1991.

[3] J. Kunisch and J. Pamp. *UWB Radio Channel Measurements for Sensor Communication in an Industrial Environment*. In Proceedings of 9th International Conference on Electromagnetics in Advanced Applications (ICEAA), Turin, ITA, September 2005.

[4] J. Karedal, S. Wyne, P. Almers, F. Tufvesson, and A. F. Molisch. *A Measurement-Based Statistical Model for Industrial Ultra-Wideband Channels*. IEEE Transactions on Wireless Communications, 6(8):3028–3037, August 2007.

[5] A. A. M. Saleh and R. A. Valenzuela. *A Statistical Model for Indoor Multipath Propagation*. IEEE Journal on Selected Areas in Communications, 5(2):128–137, February 1987.

[6] A. J. Levy. *Fine Structures of the Urban Mobile Propagation Channel*. In Proceedings Commsphere, pages 5.1.1–5.1.6, Herzliya, IL, December 1991.

[7] A. F. Molisch. *Ultrawideband Propagation Channels - Theory, Measurement, and Modeling*. IEEE Transactions on Vehicular Technology, 54(5):1528–1545, September 2005.

[8] A. F. Molisch, K. Balakrishnan, C. Chong, S. Emami, A. Fort, J. Karedal, J. Kunisch, H. Schantz, U. Schuster, and K. Siwiak. *IEEE 802.15.4a Channel Model - Final Report*. Technical report, IEEE 802.15.4a Channel Modeling Subgroup, 2004. Online available at http://www.ieee802.org/15/pub/04/15-04-0662-02-004a-channel-model-final-report-r1.pdf.

[9] J. Jiang. *Measurement, Modeling, and Performance of Indoor MIMO Channels*. PhD thesis, School of Electrical and Computer Engineering at the Georgia Institute of Technology, Atlanta, GA, USA, July 2004.

[10] D. Cassioli, M. Z. Win, and A. F. Molisch. *The Ultra-Wide Bandwidth Indoor Channel: From Statistical Model to Simulations*. IEEE Journal on Selected Areas in Communications, 20(6):1247–1257, August 2002.

[11] A. Hugine, H. I. Volos, J. Gaeddert, and R. M. Buehrer. *Measurement and Characterization of the Near-Ground Indoor Ultra Wideband Channel*. In Proceedings of the IEEE Wireless Communications and Networking Conference (WCNC), Las Vegas, NV, USA, April 2006.

[12] J. Cheng and N. C. Beaulieu. *Maximum-Likelihood Based Estimation of the Nakagami m Parameter*. IEEE Communications Letters, 5(3):101–103, March 2001.

[13] M. H. Kutner, C. J. Nachtsheim, J. Neter, and W. Li. *Applied Linear Statistical Models*. McGraw-Hill, fifth edition, 2005.

[14] T. S. Rappaport. *Wireless Communications, Principles and Practice*. Prentice Hall PTR, second edition, 2002.

[15] I. Marinović, I. Zanchi, and Z. Blažević. *Estimation of Channel Parameters for "Saleh-Valenzuela" Model Simulation*. In Proceedings of the International Conference on Applied Electromagnetics and Communications, pages 1–4, Dubrovnik, HR, October 2005.

[16] P. Pagani and P. Pajusco. *Experimental Analysis of the Ultra Wideband Propagation Channel over the 3.1 GHz-10.6 GHz Frequency Band*. In Proceedings of the IEEE International Symposium on Personal, Indoor, and Mobile Radio Communications, pages 1–5, Helsinki, FI, September 2006.

[17] T. S. Rappaport and C. D. McGillem. *UHF Fading in Factories*. IEEE Journal on Selected Areas in Communications, 7(1):40–48, January 1989.

5

Delay and angular characteristics in an office environment

5.1 Introduction

The potential benefits of implementing Multiple Input Multiple Output (MIMO) are highly dependent on the characteristics of the propagation environment. Chapter 4 discussed the time delay characteristics of MultiPath Components (MPCs). Because MIMO means using arrays of spatially separated antennas, also the spatial characteristics of MPCs become important in assessing MIMO performance. The spatial characteristics of an MPC as seen from the transmitting array and from the receiving array are determined by the MPC's direction of departure and direction of arrival, respectively. The distributions of these directional MPC parameters at the transmit and the receive side, in combination with the antenna arrays' geometries, are what determine the correlations between the signals on each of the antennas [1]. In turn, these correlations are what ultimately determine the practical benefits of MIMO, i.e. the spatial diversity gain and/or spatial multiplexing gain that can be achieved with respect to the use of single antennas.

A lot of progress has been made in the development of different types of MIMO channel models for signal processing algorithm testing [2]. In recent years, the geometry-based stochastic type of channel model, first proposed in [3], gains research interest. This kind of model presents a statistical distribution for the propagation path parameters (e.g., direction of arrival, direction of departure, delay, etc.), while also taking some geometry parameters of the environment into account

(e.g., the location of scatterers). For the moment, most geometry-based stochastic channel models use MPC clusters in their description. Clustering of MPCs seems to occur naturally in wave propagation and as an added benefit helps to reduce the number of statistical parameters needed to construct the model. Examples of geometry-based stochastic channel models can be found in [4–7].

This chapter investigates the statistics of MPC parameters including directions of arrival and departure, delay, and power in an indoor office environment. For this, MIMO channel sounding measurements with a virtual antenna array are carried out on an office floor. Propagation path parameters are extracted from measurement data and are subsequently grouped into clusters using an automatic clustering algorithm. Following, propagation path parameters are split up into an *inter-cluster* part and an *intra-cluster* part: the former is representative for the location in propagation path parameter space of the cluster to which the path belongs, while the latter is defined as the propagation path parameter's deviation from the inter-cluster part. Additionally, a new notational improvement of the wireless channel matrix is proposed which makes the separation of propagation path parameters into inter-cluster and intra-cluster parts more visible. This decomposition of the MIMO channel matrix is named FActorization into a BLock-diagonal Expression (FABLE), because the decomposition includes a block-diagonal form of the intra-cluster parameters.

Next, the inter-cluster and intra-cluster dynamics are modelled statistically. Choices for the statistical distributions are physically and statistically motivated: those types of distributions are chosen which in our opinion most accurately agree with the underlying propagation physics and which match the support of the propagation parameters. Distributional choices are justified compared to choices made in literature, e.g., the stochastic channel models in [4–7]. The main emphasis of this chapter is on the good statistical treatment of the data: the soundness of using specific distributions is validated through statistical hypothesis tests. Care is taken in the choice of appropriate hypothesis tests that have sufficient power even at low sample sizes. Additionally, parameter correlations are calculated and tested for their significance. For this, a rank correlation coefficient is used. These kind of tests can be valuable in deciding which parameter correlations can be neglected to reduce model complexity.

The outline of this chapter is as follows. First, the MIMO measurements and measurement data processing are detailed in Section 5.2. Section 5.3 presents the FABLE construction of the wireless channel transfer function. The correlations and statistical distributions of the propagation path parameters within clusters are discussed in Section 5.4. The statistical descriptions of the intra-cluster and inter-cluster parameters are further discussed in Section 5.5. Finally, conclusions are provided in Section 5.6.

5.2 Measurements and data processing

5.2.1 Measurement setup

The measurement setup for the MIMO measurements is shown in Fig. 5.1 and is detailed in the following along with the measurement procedure. A network analyzer (Agilent E8257D) is used to measure the complex channel frequency response for a set of transmitting and receiving antenna positions. The channel is probed in a 40 MHz measurement bandwidth from 3460 MHz to 3500 MHz. As transmitting antenna (Tx) and receiving antenna (Rx), broadband omnidirectional discone antennas of type Electro-Metrics EM-6116 are used. These antennas can operate in a range from 2 to 10 GHz with a nominal gain of 1 dBi. The gain variation in the measured frequency range is less than 0.5 dB, which shows a sufficiently flat antenna frequency response. The vertical half-power beamwidth of the antenna is 60°. To be able to perform measurements for large Tx-Rx separations, one port of the network analyzer is connected to the Tx through an RF/optical link with an optical fiber of length 500 m. The RF signal sent into the Tx is amplified using an amplifier of type Nextec-RF NB00383 with an average gain of 37 dB. The amplifier assures that the signal-to-noise ratio at the receiving port of the network analyzer is at least 20 dB for each measured location of the Tx and Rx. The calibration of the network analyzer is done at the connectors of the Tx and Rx antenna, and as such includes both the RF/optical link and the amplifier.

Measurements are performed using a virtual MIMO array [8]. The virtual array is created by moving the antennas to predefined positions along rails in two directions in the horizontal plane. For this, stepper motors with a spatial resolution of 0.5 mm are used. Both Tx and Rx are moved along 10 by 4 virtual Uniform Rectangular Arrays (URAs), and are polarized vertically and positioned at a height of 1.80 m during measurements (Fig. 5.1). The URA elements are spaced 4.29 cm apart, which corresponds to half a wavelength at the highest measurement frequency of 3.5 GHz and ascertains that spatial aliasing does not occur when estimating the directional characteristics of propagation paths [9]. The stepper motor controllers, as well as the network analyzer, are controlled by a Personal Computer (PC).

One important drawback of using a virtual array is that the channel has to remain time-invariant during measurements. Contrary to the procedure in chapter 4, time-invariance was assured here by performing the measurements at night in the absence of (people) movement. Furthermore, one measurement location was done per night with the fluorescent lights switched on only in the hallway. At each of 1600 ($10 \times 4 \times 10 \times 4$) combinations of Tx and Rx positioning along the URAs, the network analyzer measured the S_{21} scattering parameter ten times (i.e., 10 time observations). The total measurement time for a single MIMO measurement

is about 1h 30min.

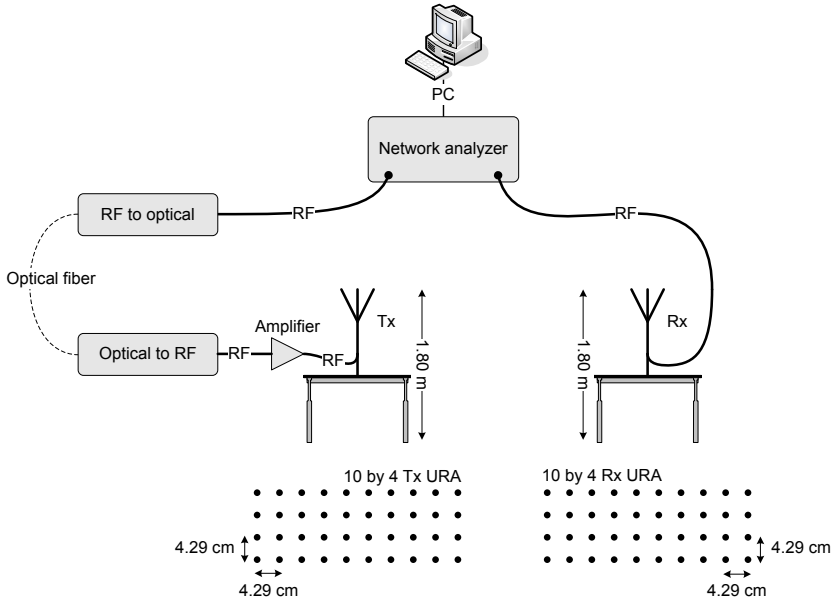

Figure 5.1: Measurement setup

5.2.2 Measurement environment

MIMO measurements are carried out on the first floor of an office building. The office floor has a rectangular shape with dimensions 57.9 m by 14.2 m. Fig. 5.2 presents a floor plan of the measurement environment, along with some relevant dimensions. The office floor consists of a hallway, which stretches horizontally in the center of Fig. 5.2 and leads to various offices at the top and bottom in the figure. All inner walls are plasterboard, except for the concrete walls between rooms 118 and 120, and between rooms 115 and 117. Fig. 5.2 also shows locations of the Tx and Rx during measurements. A total of 9 MIMO measurements are performed, their Tx and Rx locations indicated by couples of Tx_i and Rx_i ($i = 1, \ldots, 9$). Measurements are executed in both Line Of Sight (LOS) and Non Line Of Sight (NLOS) conditions[1] and cover distances between Tx and Rx from 13 to

[1] In chapters 2 to 4 concerning industrial propagation modelling, blockage of the LOS path is refered to as OBstructed line of Sight (OBS). In this chapter about office propagation modelling, blockage of the LOS path is called NLOS. This distinction is made because LOS blockage in offices is caused by walls, which stretch from floor to ceiling and as such partition the office environment. This is opposed to the factory environments, where measurements were done with Tx and Rx in the same room and blockage was caused by industrial inventory not stretching from floor to ceiling and not partitioning the room. OBS is thus defined as a "softer" form of NLOS.

45 m. Measurement locations 1, 5, and 6 are LOS. Measurements were performed with the doors of the offices closed. Fig. 5.3(a) shows a picture of the hallway together with the receiving virtual array. The hallway is free of any furniture or clutter otherwise. Fig. 5.3(b) shows a typical office on this floor together with the transmitting virtual array. The offices contain clutter comprising (wood and metal) desks, chairs, desktop PCs, and (metal) filing cabinets.

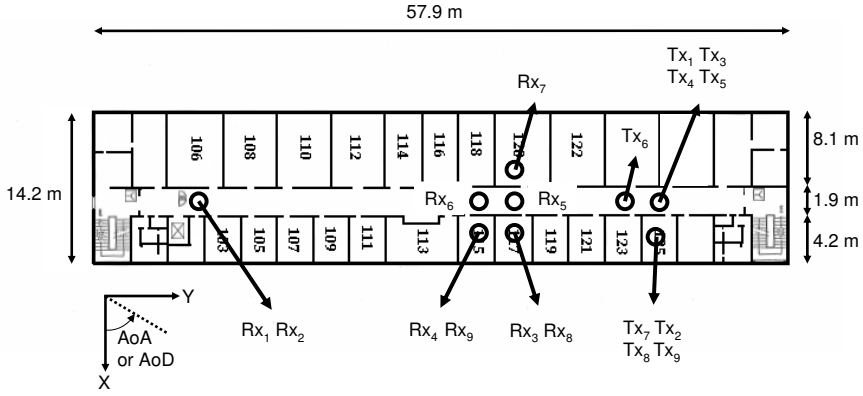

Figure 5.2: Floor plan of the measurement environment with Tx and Rx locations

(a) Hallway + Rx

(b) Office + Tx

Figure 5.3: Photos of the measurement environment including the virtual arrays

5.2.3 Parameter extraction and clustering

5.2.3.1 Extraction of directional and delay properties of MPCs

The directional Azimuth Of Arrival (AOA) and Azimuth Of Departure (AOD) parameters and the delay parameter of MPCs are extracted from measurement data using a Five-Dimensional (5D) unitary Estimation of Signal Parameters via Rotational Invariance Techniques (ESPRIT) algorithm [10]. The ESPRIT algorithm is referred to as 5D, because elevations of arrival and departure are also incorporated in its data model: this alleviates the issue of biased azimuthal angle estimates when only the azimuthal cut is present in the data model [11, 12]. Statistics of the elevation angles are however left out from further analysis, as these angles possess the "above-below" ambiguity inherent to URAs. The ESPRIT algorithm is used in combination with the simultaneous Schur decomposition procedure for automatic pairing of AOA, AOD, and delay estimates [13]. The coordinate system with respect to which AOA and AOD are defined is shown in Fig. 5.2.

URAs allow easy application of the spatial smoothing technique to increase the number of observations, while at the same time increasing the detection possibilities of coherent or correlated MPCs [14]. A downside to the technique is the reduced estimation accuracy when the dimensions of the URA subarrays are chosen too small. A possible compromise chooses sub-URAs with dimensions $2/3$ of the length in each direction of the original 10 by 4 URA (rounded to the nearest integer), i.e., 7 by 3 sub-URAs [15]. In total at both link ends, 64 different 7 by 3 sub-URAs can be found, thereby increasing the number of observations by a factor of 64. Together with the previously mentioned 10 time observations (Section 5.2.1), the total number of available observations is 640.

Furthermore, in the 40 MHz measurement bandwidth, 10 equally spaced frequency points are used with the ESPRIT algorithm. The considered constant spacing Δf between these frequencies is 4 MHz. With this choice, the corresponding maximum resolvable delay $\tau_{\max}$ is $1/\Delta f = 250$ ns or the maximum resolvable path length $d_{\max}$ is $c/\Delta f = 75$ m. This $d_{\max}$ is slightly larger than the sum of the length and width of the measured office floor. Therefore, nearly all physically possible MPCs are expected to have a path length less than $d_{\max}$, consequently limiting possible aliasing in the delay domain. **Summarizing, 5D unitary ESPRIT is applied to a 5D vector space of size $7 \times 3 \times 7 \times 3 \times 10$ (spatial dimensions of size 7 and 3 following from each the Tx and Rx URA, and the frequency dimension of size 10) with 640 observations.**

The ESPRIT algorithm is used to estimate the 100 strongest paths from measurement data [7, 16]. Next, the estimated MPCs are postprocessed in the delay domain by considering the Power Delay Profile (PDP), i.e. MPC power versus delay. For a typical PDP, power is concentrated at small delays while at large delays only the noise floor remains. In our measurements, the noise floor is set to

the power of the MPC with the largest delay. Following, all MPCs with power less than the noise floor plus a noise threshold of 6 dB are omitted from further analysis [7]. This is exemplified in Fig. 5.4, which shows a PDP of MPCs detected at measurement location 2: all MPCs with power below the solid horizontal line are discarded. For all measurement locations after postprocessing, between 35 and 87 MPCs are retained. Figs. 5.5(a) and 5.6(a) show AOA/AOD/delay scatter plots of MPCs detected at measurement locations 1 (LOS) and 7 (NLOS), respectively. The power on a dB-scale of each MPC is indicated by a color.

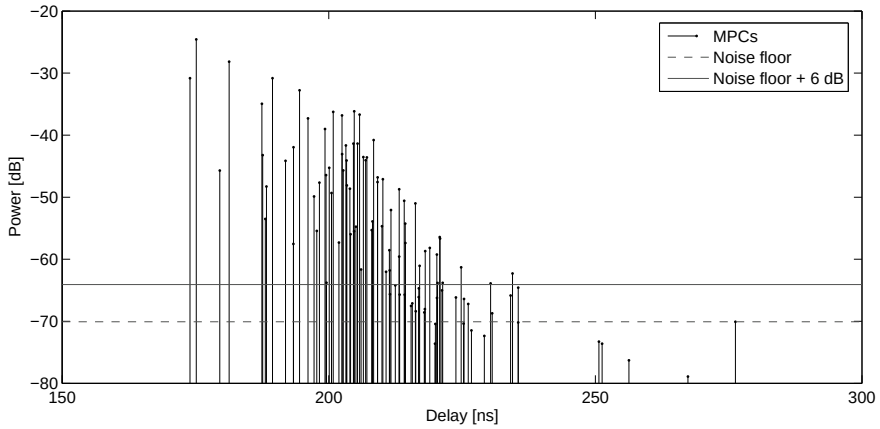

Figure 5.4: PDP of MPCs at measurement location 2

5.2.3.2 Clustering of MPCs

Automatic joint clustering of AOA, AOD, and delay is performed using the statistical K-power-means algorithm [17]. The K-power-means algorithm is an improvement of the common K-means algorithm which also takes MPC powers into account: more important MPCs with large power act as centers of gravity which pull the cluster centroid positions towards them. The K-power-means algorithm result is in agreement with the COST 273 definition of a cluster as a set of MPCs with similar propagation characteristics [6]. Because some parameters for clustering are circular, Multipath Component Distance (MCD) is used as the distance measure for clustering [18]. A delay scaling factor of 5 was used with the MCD, the same value as used for clustering in indoor office environments in [7]. Clustering results will usually depend on the initial choice (seeding) of the cluster centroid positions. For this reason, the K-power-means algorithm is repeated 200 times with different, randomly chosen initial seedings. Clustering results are retained for the seeding which gives the smallest total power-weighted MCD between MPCs and their respective cluster centroids [17].

For each measurement location, the number of clusters for the K-power-means algorithm is varied between 2 and 10. The optimal number of clusters is selected according to Kim-Parks index [19]. The Kim-Parks index is preferred over other more common validity indices that make use of intra-cluster and inter-cluster separation measures, such as the Davies-Bouldin and Caliñski-Harabasz indices, as these indices tend to decrease or increase monotonically with the number of clusters [16, 20]. The Kim-Parks index circumvents this behavior by normalizing the index by the index values at the minimum and maximum number of clusters. The number of detected clusters varies from 3 to 8 between measurement locations, and for all MIMO measurements combined, a total of 45 clusters are found (16 clusters from LOS and 29 clusters from NLOS measurements). Next, to ease the statistical analysis, clearly outlying MPCs are removed from each cluster using the shapeprune algorithm detailed in [17]. To preserve the cluster's original power and shape, outliers are discarded with the restraint that the total cluster power and the cluster Root Mean Square (RMS) AOA, AOD, and delay spreads remain within 10% of their values prior to outlier removal.

After pruning outliers, the average cluster RMS AOA and AOD spreads are 22° and 36°, respectively. For comparison, cluster RMS azimuthal spreads between 2° and 9° were found in [21]. The main reason for the larger spread values obtained here is that the clustering for our measurements takes the delay domain into account, while the study in [21] restricts clustering to the AOA/AOD domains. It is also mentioned in their work that restricting clustering to the azimuthal domains results in more clusters and hence smaller spread values. The spread values obtained here compare more to those in the related work of [21], where values between 22° and 27° are found. Next, cluster RMS delay spreads vary between 0.5 and 3.4 ns for LOS. For NLOS, cluster RMS delay spreads are between 0.4 and 9.9 ns, and are comparable to spreads between 2 and 15 ns found in [16]. Figs. 5.5(b) and 5.6(b) show scatter plots of the clustering results for measurement locations 1 and 7. For these measurements, the Kim-Parks index estimated the number of clusters at 7 and 4, respectively. MPCs grouped into different clusters are shown with different marker shapes and colors.

5.3 Model

5.3.1 Signal model

For the analysis of the intra-cluster and inter-cluster MPC parameters, we use the following basic signal model, based on the double-directional channel model first proposed in [22]. For one of the measurement locations, the complex received envelope $h\left(\phi^A, \phi^D, \tau\right)$ is written as function of the propagation path parameters:

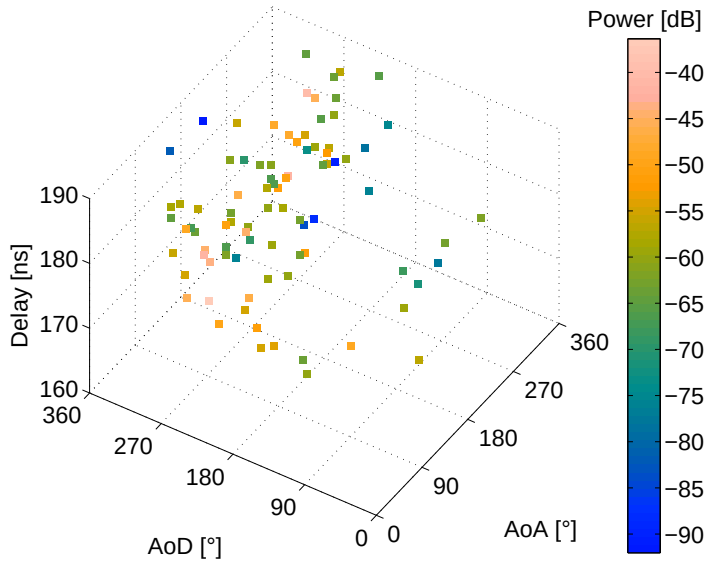

(a) MPC AOA/AOD/delay scatter plot

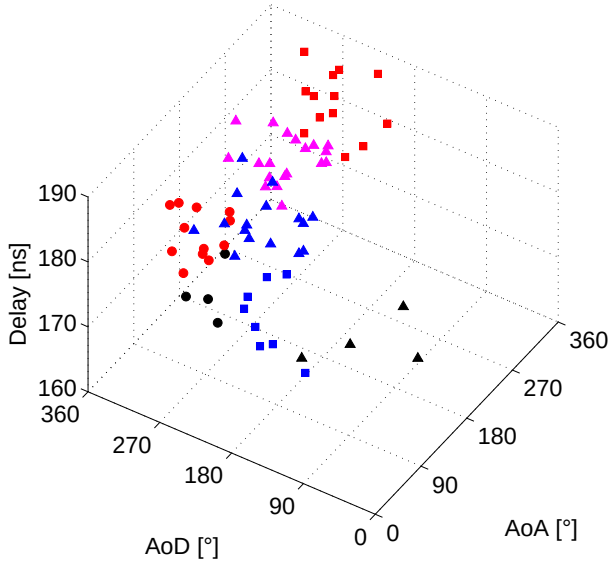

(b) MPC K-power-means clustering

Figure 5.5: MPC scatter plot and clustering for measurement location 1 (LOS)

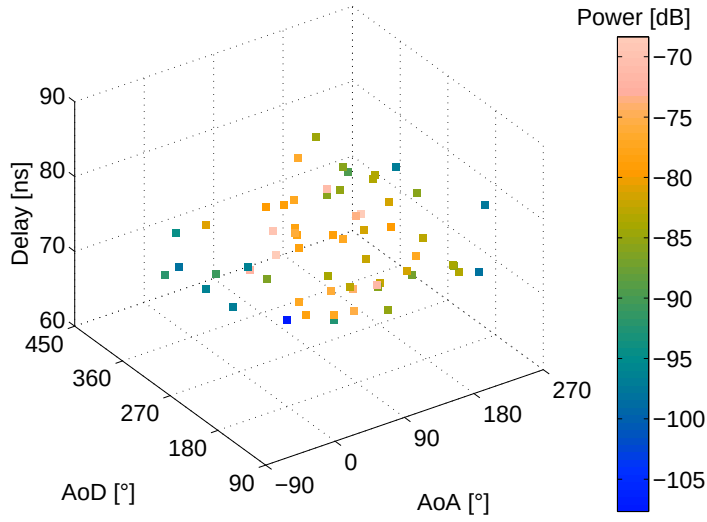

(a) MPC AOA/AOD/delay scatter plot

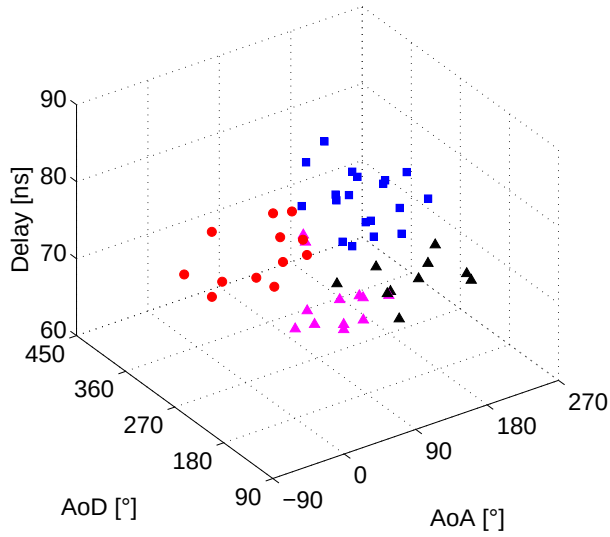

(b) MPC K-power-means clustering

Figure 5.6: MPC scatter plot and clustering for measurement location 7 (NLOS)

ϕ^A denotes the AOA, ϕ^D the AOD, and τ is the path delay. The use of MPC clusters is reflected in the complex envelope's notation:

$$h\left(\phi^A, \phi^D, \tau\right) = \sum_{c=1}^{n_C} \sum_{k=1}^{n_{P,c}} A_{c,k} \cdot \delta\left(\phi^A - \Phi_{c,k}^A\right) \cdot \delta\left(\phi^D - \Phi_{c,k}^D\right) \cdot \delta\left(\tau - T_{c,k}\right) \tag{5.1}$$

In (5.1), n_C is the number of clusters and $n_{P,c}$ is the number of MPCs within cluster c. For the k-th propagation path in cluster c, $A_{c,k}$ is its received complex amplitude, $\Phi_{c,k}^A$ and $\Phi_{c,k}^D$ are its AOA and AOD, respectively, and $T_{c,k}$ is its delay. $\delta(\cdot)$ denotes the Dirac delta function. We also define $P_{c,k}$ as the power of path k in cluster c, i.e., $P_{c,k} = \mathrm{E}\left[\left|A_{c,k}\right|^2\right]$ where the expectation operator $\mathrm{E}[\cdot]$ is taken over all observations. Instead of directly modelling the statistics of the complex amplitude $A_{c,k}$, the path's power $P_{c,k}$ will be modelled. To allow statistical analysis of propagation parameters of all measurement locations collectively, the dependence of power $P_{c,k}$ and delay $T_{c,k}$ on distance is removed. Power is rescaled such that the total received MPC power equals one and the origin of the delay axis is set to coincide with the first arriving MPC. Assuming larger values of c or k mean later arriving paths:

$$\sum_{c=1}^{n_C} \sum_{k=1}^{n_{P,c}} P_{c,k} = 1 \quad \text{and} \quad T_{1,1} = 0 \text{ ns} \tag{5.2}$$

The signal model in (5.1) is extended by splitting up each of the MPC parameters into an inter-cluster and an intra-cluster part:

$$\begin{cases} A_{c,k} = \sqrt{p_c}\, a_{c,k} \\ P_{c,k} = p_c\, p_{c,k} \\ \Phi_{c,k}^A = \phi_c^A + \phi_{c,k}^A \\ \Phi_{c,k}^D = \phi_c^D + \phi_{c,k}^D \\ T_{c,k} = \tau_c + \tau_{c,k} \end{cases} \tag{5.3}$$

In (5.3), the parameters p_c, ϕ_c^A, ϕ_c^D, and τ_c denote *inter-cluster* propagation parameters, and are representative for the *location* of each cluster in the power/AOA/AOD/delay parameter space. Also in (5.3), $a_{c,k}$, $p_{c,k}$, $\phi_{c,k}^A$, $\phi_{c,k}^D$, and $\tau_{c,k}$ are *intra-cluster* propagation parameters. The intra-cluster parameters can be seen as the deviations of the path parameters from the cluster's location as dictated by the inter-cluster parameters. The intra-cluster parameters are therefore fully determined by the *spread* of power, AOA, AOD, and delay in each of the clusters. With the definitions in (5.3), the signal model in (5.1) is rewritten as:

$$h\left(\phi^A, \phi^D, \tau\right) = \sum_{c=1}^{n_C} \sum_{k=1}^{n_{P,c}} \sqrt{p_c}\, a_{c,k} \cdot \delta\left(\phi^A - \phi_c^A - \phi_{c,k}^A\right) \cdot \delta\left(\phi^D - \phi_c^D - \phi_{c,k}^D\right) \cdot \delta\left(\tau - \tau_c - \tau_{c,k}\right) \tag{5.4}$$

Section 5.4 discusses the statistical distributions of $P_{c,k}$, $\Phi_{c,k}^A$, $\Phi_{c,k}^D$, and $T_{c,k}$ within each cluster. The most common probability distributions are location-scale distributions: they are parameterized by a location parameter, which determines the distribution's location or shift, and a scale parameter, which determines the distribution's dispersion or spread. These two types of distributional parameters can fully describe the inter-cluster and intra-cluster propagation parameters, and hence the signal model in (5.4): the distributional location parameter can be identified with the inter-cluster propagation parameter, and the distributional scale parameter fully characterizes the intra-cluster propagation parameter. The distributional location and scale parameters are further discussed in Section 5.5.

5.3.2 FABLE notation

The goal of this section is to provide a new notation for the MIMO channel matrix. This notation is named FABLE [23, 24]. The appeal of the FABLE notation laid out here is in its future incorporation in the data model of multipath estimation algorithms. The FABLE notation further subdivides each of the angular and delay dimensions into an intra- and inter-cluster subdimension. This subdivision has the potential to further reduce the computational complexity of space-alternating estimation algorithms, as the harmonic retrieval problem is broken down into more dimensions. For appropriate antenna arrays at transmit and receive side, the transformation of (5.4) to aperture space is given by:

$$\mathcal{H}\left(r, s, f\right) = \sum_{c=1}^{n_C} \sum_{k=1}^{n_{P,c}} \sqrt{p_c}\, a_{c,k} \cdot \exp\left[-j2\pi\left(r-1\right) \mathrm{G}_{\mathrm{Rx}}\left(\phi_c^A + \phi_{c,k}^A\right)\right] \cdot \exp\left[-j2\pi\left(s-1\right) \mathrm{G}_{\mathrm{Tx}}\left(\phi_c^D + \phi_{c,k}^D\right)\right] \cdot \exp\left[-j2\pi f\left(\tau_c + \tau_{c,k}\right)\right] \tag{5.5}$$

In (5.5), the variables r, s, and f denote the transform variables of the Fourier transform of ϕ^A, ϕ^D, and τ, respectively. Each (integer) value of r and s can be associated with one of the antennas of the Rx and Tx antenna array. The variable f denotes the frequency of the transmitted signal. The functions $\mathrm{G}_{\mathrm{Rx}}\left(\cdot\right)$ and $\mathrm{G}_{\mathrm{Tx}}\left(\cdot\right)$ depend on the Rx and Tx array geometry. For example, $\mathrm{G}_{\mathrm{Rx}}\left(\cdot\right) = d/\lambda \sin\left(\cdot\right)$ for a Uniform Linear Array (ULA) at receive side, where d is the spacing between antenna array elements and λ is the wavelength.

In the following, it is assumed that the array geometry functions $\mathrm{G}_{\mathrm{Rx}}\left(\cdot\right)$ and $\mathrm{G}_{\mathrm{Tx}}\left(\cdot\right)$ are linear, e.g. for the Rx, that it holds that $\mathrm{G}_{\mathrm{Rx}}(\phi_c^A + \phi_{c,k}^A) = \mathrm{G}_{\mathrm{Rx}}(\phi_c^A) +$

$\mathrm{G_{Rx}}(\phi^A_{c,k})$. Unfortunately, this assumption is usually not valid, e.g., for the ULA, URA, and Uniform Circular Array (UCA) geometries. This can be remedied by transforming the inter-cluster and intra-cluster angular propagation parameters. For example for the receive side, the FABLE notation in the following can be used with ψ^A_c and $\psi^A_{c,k}$ as inter-cluster and intra-cluster AOA, respectively, for which it is satisfied that $\mathrm{G_{Rx}}(\Phi^A_{c,k}) = \mathrm{G_{Rx}}(\psi^A_c) + \mathrm{G_{Rx}}(\psi^A_{c,k})$. For example for a ULA, this can be shown to hold if ψ^A_c and $\psi^A_{c,k}$ are defined such that $\sin(\psi^A_c) = \sin(\phi^A_c)\cos(\phi^A_{c,k})$ and $\sin(\psi^A_{c,k}) = \cos(\phi^A_c)\sin(\phi^A_{c,k})$. This transformation can be done without consequence as there is an inherent arbitrariness on how the AOA is split up into its respective inter- and intra-cluster parts. The disadvantage of redefining the inter- and intra-cluster AOA is however that $\Phi^A_{c,k} \neq \psi^A_c + \psi^A_{c,k}$, contrary to the definition with ϕ-s in (5.3). This means that, unlike the definition with ϕ-s, the inter- and intra-cluster AOAs defined as ψ-s cannot be quickly related to the corresponding MPC AOA $\Phi^A_{c,k}$, and also depend on the array geometry function $\mathrm{G_{Rx}}(\cdot)$ under consideration.

We assume that the Rx and Tx antenna arrays consist of R and S antenna elements, respectively ($r = 1, \ldots, R$ and $s = 1, \ldots, S$). The MIMO channel transfer function $\mathcal{H}(r, s, f)$ is first rewritten as the MIMO channel matrix $\boldsymbol{H}(f)$. The channel matrix $\boldsymbol{H}$ has the common structure where the row dimension of $\boldsymbol{H}$ is made up from receive elements r and its column dimension is made up from transmit elements s ($\boldsymbol{H}$ has dimensions $R \times S$). The channel matrix $\boldsymbol{H}(f)$ is decomposed as the product of three matrices:

$$\boldsymbol{H}(f) = \boldsymbol{B^{Rx}}(f) \cdot \boldsymbol{W}(f) \cdot \boldsymbol{B^{Tx}} \tag{5.6}$$

In (5.6), $\boldsymbol{B^{Rx}}(f)$ and $\boldsymbol{B^{Tx}}$ contain inter-cluster propagation parameters associated with the Rx and Tx, respectively. By choice, the inter-cluster parameters p_c, ϕ^A_c, and τ_c are considered to be properties of cluster c as seen by the Rx, while ϕ^D_c is considered to characterize cluster c as seen from the Tx. Because of the choice to include delay τ_c in $\boldsymbol{B^{Rx}}(f)$, the elements of this matrix depend on the frequency f. Also in (5.6), $\boldsymbol{W}(f)$ gathers the intra-cluster propagation parameters $a_{c,k}$, $\phi^A_{c,k}$, $\phi^D_{c,k}$, and $\tau_{c,k}$. The matrices $\boldsymbol{B^{Rx}}$, $\boldsymbol{W}$, and $\boldsymbol{B^{Tx}}$ are built from submatrices $\boldsymbol{B^{Rx}_c}$, $\boldsymbol{W_c}$, and $\boldsymbol{B^{Tx}_c}$ which contain the inter-cluster and intra-cluster propagation parameters solely associated with cluster c. The stacking of these submatrices is done as follows (the f dependency is left out for better readability):

$$\begin{aligned}\boldsymbol{H} &= \boldsymbol{B}^{\mathbf{Rx}} \cdot \boldsymbol{W} \cdot \boldsymbol{B}^{\mathbf{Tx}} \\ &= \begin{bmatrix} \boldsymbol{B}_{\mathbf{1}}^{\mathbf{Rx}} \\ \boldsymbol{B}_{\mathbf{2}}^{\mathbf{Rx}} \\ \vdots \\ \boldsymbol{B}_{\boldsymbol{n_C}}^{\mathbf{Rx}} \end{bmatrix}^T \cdot \begin{bmatrix} \boldsymbol{W_1} & \mathbf{0} & \dots & \mathbf{0} \\ \mathbf{0} & \boldsymbol{W_2} & \dots & \mathbf{0} \\ \vdots & \vdots & \ddots & \vdots \\ \mathbf{0} & \mathbf{0} & \dots & \boldsymbol{W_{n_C}} \end{bmatrix} \cdot \begin{bmatrix} \boldsymbol{B}_{\mathbf{1}}^{\mathbf{Tx}} \\ \boldsymbol{B}_{\mathbf{2}}^{\mathbf{Tx}} \\ \vdots \\ \boldsymbol{B}_{\boldsymbol{n_C}}^{\mathbf{Tx}} \end{bmatrix}\end{aligned} \tag{5.7}$$

The stacking of the submatrices $\boldsymbol{W_c}$ gives rise to a block-diagonal form for the intra-cluster matrix $\boldsymbol{W}$, from which the name FActorization into a BLock-diagonal Expression (FABLE) is derived.

5.3.2.1 Inter-cluster submatrices $\boldsymbol{B_c^{Rx}}$ and $\boldsymbol{B_c^{Tx}}$

For cluster c, the submatrices $\boldsymbol{B_c^{Rx}}$ and $\boldsymbol{B_c^{Tx}}$ have the following structure.

$$\boldsymbol{B_c^{Rx}} = \sqrt{p_c}\, \exp\left[-j2\pi f \tau_c\right] \cdot \begin{bmatrix} 1 & 0 & \dots & 0 \\ 0 & \exp\left[-j2\pi \mathrm{G_{Rx}}\left(\phi_c^A\right)\right] & \dots & 0 \\ \vdots & \vdots & \ddots & \vdots \\ 0 & 0 & \dots & \exp\left[-j2\pi\left(R-1\right)\mathrm{G_{Rx}}\left(\phi_c^A\right)\right] \end{bmatrix} \tag{5.8}$$

$$\boldsymbol{B_c^{Tx}} = \begin{bmatrix} 1 & 0 & \dots & 0 \\ 0 & \exp\left[-j2\pi \mathrm{G_{Tx}}\left(\phi_c^D\right)\right] & \dots & 0 \\ \vdots & \vdots & \ddots & \vdots \\ 0 & 0 & \dots & \exp\left[-j2\pi\left(S-1\right)\mathrm{G_{Tx}}\left(\phi_c^D\right)\right] \end{bmatrix} \tag{5.9}$$

It is clear that $\boldsymbol{B_c^{Rx}}$ only contains inter-cluster propagation parameters associated with the Rx: the cluster mean AOA ϕ_c^A, the cluster onset τ_c at receive side, and the cluster median received power p_c. The submatrix $\boldsymbol{B_c^{Tx}}$ contains the inter-cluster parameter associated with the Tx, i.e., the cluster mean AOD ϕ_c^D. The submatrices $\boldsymbol{B_c^{Rx}}$ and $\boldsymbol{B_c^{Tx}}$ have dimensions $R \times R$ and $S \times S$, respectively.

5.3.2.2 Intra-cluster submatrix $\boldsymbol{W_c}$

For cluster c, the submatrix $\boldsymbol{W_c}$ is written as the product of three matrices.

$$\boldsymbol{W_c} = \boldsymbol{V_c^{Rx}} \cdot \boldsymbol{D_c^{Rx}} \cdot \boldsymbol{V_c^{Tx}} \tag{5.10}$$

The three matrices $\boldsymbol{V_c^{Rx}}$, $\boldsymbol{D_c^{Rx}}$ and $\boldsymbol{V_c^{Tx}}$ possess the following structure:

$$\boldsymbol{V_c^{Rx}} = \begin{bmatrix} 1 & \dots & 1 \\ \exp\left[-j2\pi \mathrm{G_{Rx}}\left(\phi_{c,1}^{A}\right)\right] & \dots & \exp\left[-j2\pi \mathrm{G_{Rx}}\left(\phi_{c,n_{P,c}}^{A}\right)\right] \\ \vdots & \ddots & \vdots \\ \exp\left[-j2\pi\left(R-1\right)\mathrm{G_{Rx}}\left(\phi_{c,1}^{A}\right)\right] & \dots & \exp\left[-j2\pi\left(R-1\right)\mathrm{G_{Rx}}\left(\phi_{c,n_{P,c}}^{A}\right)\right] \end{bmatrix} \tag{5.11}$$

$$\boldsymbol{D_c^{Rx}} = \begin{bmatrix} a_{c,1}\exp\left[-j2\pi f\left(\tau_{c,1}\right)\right] & \dots & 0 \\ \vdots & \ddots & \vdots \\ 0 & \dots & a_{c,n_{P,c}}\exp\left[-j2\pi f\left(\tau_{c,n_{P,c}}\right)\right] \end{bmatrix} \tag{5.12}$$

$$\boldsymbol{V_c^{Tx}} = \begin{bmatrix} 1 & \exp\left[-j2\pi \mathrm{G_{Tx}}\left(\phi_{c,1}^{D}\right)\right] & \dots & \exp\left[-j2\pi\left(S-1\right)\mathrm{G_{Tx}}\left(\phi_{c,1}^{D}\right)\right] \\ 1 & \exp\left[-j2\pi \mathrm{G_{Tx}}\left(\phi_{c,2}^{D}\right)\right] & \dots & \exp\left[-j2\pi\left(S-1\right)\mathrm{G_{Tx}}\left(\phi_{c,2}^{D}\right)\right] \\ \vdots & \vdots & \ddots & \vdots \\ 1 & \exp\left[-j2\pi \mathrm{G_{Tx}}\left(\phi_{c,n_{P,c}}^{D}\right)\right] & \dots & \exp\left[-j2\pi\left(S-1\right)\mathrm{G_{Tx}}\left(\phi_{c,n_{P,c}}^{D}\right)\right] \end{bmatrix} \tag{5.13}$$

$\boldsymbol{V_c^{Rx}}$ and $\boldsymbol{V_c^{Tx}}$ are Vandermonde matrices which contain for cluster c the intra-cluster AOAs $\phi_{c,k}^{A}$ and the intra-cluster AODs $\phi_{c,k}^{D}$ respectively ($k = 1, \dots, n_{P,c}$). The diagonal matrix $\boldsymbol{D_c^{Rx}}$ comprises the received intra-cluster complex amplitude $a_{c,k}$ and the intra-cluster delay $\tau_{c,k}$. The matrices $\boldsymbol{V_c^{Rx}}$, $\boldsymbol{D_c^{Rx}}$, and $\boldsymbol{V_c^{Tx}}$ have dimensions $R \times n_{P,c}$, $n_{P,c} \times n_{P,c}$, and $n_{P,c} \times S$, respectively.

As a closing remark, the FABLE notation in (5.7) can intuitively be understood as follows. Firstly, clusters with their average directional characteristics are created at transmit side by the matrix $\boldsymbol{B^{Tx}}$. Next, the block-diagonal $\boldsymbol{W}$ matrix introduces several discrete paths into each cluster. The matrix $\boldsymbol{W}$ can be thought of as the operator which unfolds each cluster into its discrete paths. Finally, the matrix $\boldsymbol{B_c^{Rx}}$ describes how the clusters' average directional characteristics are seen by the Rx when they arrive at receive side.

5.4 Statistics of the MPC parameters

This section discusses the statistical distributions within each cluster of the MPC parameters $\Phi^A_{c,k}$, $\Phi^D_{c,k}$, $T_{c,k}$, and $P_{c,k}$. Preliminarily, the correlations between these four parameters are investigated to check whether they can be modelled separately by univariate distributions. A summary of this section's results is found in Table 5.2 (first and second column) on page 128.

5.4.1 Correlations

In this section, correlations between azimuthal angles $\Phi^A_{c,k}$ and $\Phi^D_{c,k}$, delay $T_{c,k}$, and power $P_{c,k}$ are calculated. The measure of correlation used is Spearman's rank correlation coefficient [25]. This correlation coefficient is non-parametric in the sense that it does not make any assumptions on the form of the relationship between the two variables, other than being a monotonic relationship. This is opposed to parametric measures of correlation: the most well-known is Pearson's product-moment correlation coefficient which searches specifically for a linear relationship, an assumption which cannot always be motivated. Spearman's correlation is calculated between the four MPC parameters on a per cluster basis. For the MPCs in cluster c, Spearman's correlation coefficient $\rho_c\left(X_{c,k}, Y_{c,k}\right)$ between MPC parameters $X_{c,k}$ and $Y_{c,k}$ is given by ($X_{c,k}$, $Y_{c,k}$ = $\Phi^A_{c,k}$, $\Phi^D_{c,k}$, $T_{c,k}$, or $P_{c,k}$):

$$\rho_c\left(X_{c,k}, Y_{c,k}\right) = 1 - \frac{6\sum_{k=1}^{n_{P,c}}\left(x_{c,k} - y_{c,k}\right)^2}{n_{P,c}\left(\left(n_{P,c}\right)^2 - 1\right)} \tag{5.14}$$

In (5.14), $x_{c,k}$ and $y_{c,k}$ represent the statistical ranks[2] of $X_{c,k}$ and $Y_{c,k}$. Before calculating their ranks, the azimuthal angle variables are restricted to their principal value in $(-\pi, \pi]$ to avoid the 2π ambiguity. Table 5.1 shows average values of $\rho_c\left(X_{c,k}, Y_{c,k}\right)$ taken over all 45 clusters detected in the measurement campaign. Table 5.1 shows fairly weak average correlations between the MPC parameters. The strongest correlation is found between path power $P_{c,k}$ and path delay $T_{c,k}$ (negative average correlation of -0.28). This correlation is expected and well-established by the Saleh-Valenzuela (SV) model, where power decay within a cluster is modelled as a monotonically decreasing exponential function of delay (see formula (4.3) and [26]). For all $\rho_c\left(X_{c,k}, Y_{c,k}\right)$, hypothesis tests (non-parametric permutation tests) are carried out to decide whether or not the correlation coefficients differ significantly from zero. Table 5.1 lists the success rates of these tests, i.e. for which percentage of clusters the test decided in favor of zero correlation, at both the 5% and 1% significance levels. Table 5.1 shows that, for

[2] If tied ranks should exist (i.e., $\exists k$: $x_{c,k} = y_{c,k}$), then Spearman's correlation is calculated as Pearson's correlation coefficient between ranks $x_{c,k}$ and $y_{c,k}$.

most clusters, the MPC parameter correlations can assumed to be zero (success rates of more than 80% and more than 93% at the 5% and 1% significance level, respectively). As expected, the success rates are the lowest for correlation between $P_{c,k}$ and $T_{c,k}$, for which the strongest correlation was found. Correlations between MPC parameters within clusters can assumed to be weak and often indistinguishable from zero. Therefore, the MPC parameters $\Phi^A_{c,k}$, $\Phi^D_{c,k}$, $T_{c,k}$, and $P_{c,k}$ are modelled separately by univariate distributions in the next sections, without taking any relationships between them into account[3].

	Average correlation [-]			Success rates at 5%/1% significance [%]		
	$\Phi^D_{c,k}$	$T_{c,k}$	$P_{c,k}$	$\Phi^D_{c,k}$	$T_{c,k}$	$P_{c,k}$
$\Phi^A_{c,k}$	0.04	-0.12	0.18	100.0/100.0	88.9/95.6	86.7/95.6
$\Phi^D_{c,k}$		-0.01	-0.09		95.6/100.0	95.6/100.0
$T_{c,k}$			-0.28			80.0/93.3

Table 5.1: Average Spearman's correlation of MPC parameters within each cluster and success rates for zero correlation

5.4.2 Azimuths of arrival $\Phi^A_{c,k}$ and departure $\Phi^D_{c,k}$

In this section, we discuss the marginal distributions of AOAs $\Phi^A_{c,k}$ and AODs $\Phi^D_{c,k}$ for each individual cluster c. In literature, various distributions are proposed for the azimuth angles within a certain cluster. In [7], a normal distribution is chosen where realizations are mapped to their principal value in $(-\pi, \pi]$. A Laplacian distribution for the azimuth angles is first proposed in [27]. Additionally, we consider the von Mises distribution [28]. The von Mises distribution can be thought of as an analogue of the normal distribution for circular data. Special consideration is given to this distribution, because the von Mises distribution seems natural in describing the statistics of azimuth data: the support of the von Mises distribution is an interval of length 2π, the same as the support of azimuth data, while the support of the normal and Laplacian distribution is an interval of infinite length. For example for the AOAs $\Phi^A_{c,k}$ in cluster c, the von Mises Probability Density Function (PDF) $p_{\mathrm{vm}}(\Phi^A_{c,k}\,;\,\alpha^A_c, \kappa^A_c)$ is given as:

[3]It is noted that zero correlation does not necessarily imply independence where MPC parameters can be fully described solely by their marginal distributions. The fact that correlations often cannot be distinguished from zero, means that relating different MPC parameters through circular-circular, circular-linear, or linear-linear regression will complicate the model without significantly reducing the model's error. Dependence means that more complicated relations between the MPC parameters may however exist.

$$p_{\mathrm{vm}}\left(\Phi_{c,k}^{A}\,;\,\alpha_{c}^{A},\kappa_{c}^{A}\right)=\frac{\exp\left[\kappa_{c}^{A}\cos\left(\Phi_{c,k}^{A}-\alpha_{c}^{A}\right)\right]}{2\pi I_{0}\left(\kappa_{c}^{A}\right)} \tag{5.15}$$

In (5.15), $I_0(\cdot)$ is the modified Bessel function of the zeroth order. The two parameters that characterize the von Mises PDF are α_c^A, the circular mean of $\Phi_{c,k}^A$, and κ_c^A, which is a measure of concentration of $\Phi_{c,k}^A$ angles around α_c^A (and hence an inverse measure of angular dispersion or variance). For the von Mises PDF of AODs $\Phi_{c,k}^D$ in cluster c, an expression analogous to (5.15) can be written.

The most fit distributions for the intra-cluster AOAs and AODs are investigated as follows. From the azimuth angles $\Phi_{c,k}^A$ and $\Phi_{c,k}^D$, the Maximum Likelihood Estimators (MLEs) of the parameters of the normal, Laplacian, and von Mises PDF are calculated separately for AOAs and AODs and for each cluster c. For cluster c, the likelihood of observing the samples $\Phi_{c,k}^A$ (analogously $\Phi_{c,k}^D$) for $k = 1,\ldots,n_{P,c}$ as possible outcomes under each of the three statistical distributions (with the MLEs as distributional parameters) is calculated. The most fit distribution is determined by performing simple Likelihood Ratio Tests (LRTs): the statistical distribution which renders the largest likelihood is most appropriate for describing the azimuth angle statistics for that cluster. For the 45 clusters in this measurement campaign, all LRTs decided in favor of the von Mises distribution for both $\Phi_{c,k}^A$ and $\Phi_{c,k}^D$. Fig. 5.7 shows the empirical Cumulative Distribution Function (CDF) of the AOAs $\Phi_{c,k}^A$ of a cluster at measurement location 5. Also shown are the estimated CDFs of the Von Mises, normal, and Laplacian distributions. Visually, it could be concluded from Fig. 5.7 that all three investigated theoretical distributions provide a reasonable fit to the empirical data, and that any of these distributions could be chosen for modelling the AOA. However, the LRTs allow to quantitatively measure the Goodness Of Fit (GOF) and decide in favor of the von Mises distribution.

5.4.3 Delay $T_{c,k}$

In this section, the statistics within each cluster c of the delay parameter $T_{c,k}$ are discussed. The marginal distribution of the delay parameter can be modelled in a number of ways. In [7], MPC delays within a cluster are assumed to be normally distributed. A possible issue with this modeling approach is that MPC delays inherently only take on positive values, which does not match the support of the normal distribution. To avoid this issue, MPC delays $T_{c,k}$ within cluster c are modelled according the principle laid out by the well-known, cluster-based SV model [26]. Herein, the waiting time between the arrival of two consecutive MPCs within a certain cluster is modelled by an exponential distribution (see formula (4.5)). For the MPCs in cluster c (assuming the delays are ordered such that $T_{c,1} <$

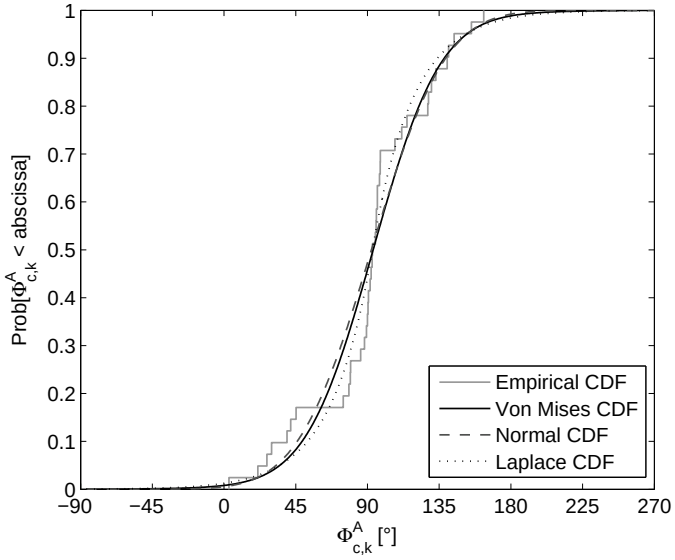

Figure 5.7: CDF plot of $\Phi^A_{c,k}$ and estimated theoretical CDFs for a cluster at measurement location 5

$T_{c,2} < \ldots < T_{c,n_{P,c}}$), the exponential PDF $p_{\exp}(T_{c,k} \mid T_{c,k-1}\,;\,\lambda_c)$ as function of the delay $T_{c,k}$ of the k-th MPC, given that the $(k-1)$-th MPC arrived at known delay $T_{c,k-1}$, is written as:

$$p_{\exp}\left(T_{c,k} \mid T_{c,k-1}\,;\,\lambda_c\right) = \frac{1}{\lambda_c} \exp\left[-\frac{T_{c,k} - T_{c,k-1}}{\lambda_c}\right] \tag{5.16}$$

In (5.16), the exponential distribution has the parameter λ_c which corresponds to the mean waiting time between consecutive MPCs in cluster c. An additional distributional parameter θ_c is defined as the delay of the first arriving path in cluster c, i.e., $\theta_c = T_{c,1}$, as $T_{c,1}$ does not follow from (5.16). The SV approach to modeling the delay distribution within clusters is also mentioned in the MIMO channel model in [29]. However, the actual channel modeling effort herein consists of a tapped delay line model, therefore the mean waiting time λ_c and the cluster onset θ_c are not explicitly modeled.

For each cluster c, the mean waiting time λ_c is estimated by its MLE following from the exponential distribution, i.e., the MLE of λ_c is calculated as the mean of samples $T_{c,k} - T_{c,k-1}$ for $k = 2, \ldots, n_{P,c}$. The plausibility of an exponential distribution for the arrival times $T_{c,k}$ is then validated by executing an Anderson-Darling (AD) GOF test for composite exponentiality [30]. For the 45 clusters in the measurement campaign, the minimum, average, and maximum p-values associated

with the AD test are equal to 0.06, 0.40, and 0.92, respectively. This means that, at the 5% significance level, all 45 clusters retain exponentiality. Fig. 5.8 shows the Quantile-Quantile (QQ) plot of the empirical quantiles of samples $T_{c,k} - T_{c,k-1}$ versus the theoretical quantiles of the exponential distribution (5.16) for a cluster detected at measurement location 3 (the MLE of λ_c equals 0.53 ns). Fig. 5.8 shows good agreement of the waiting times in this cluster with an exponential distribution.

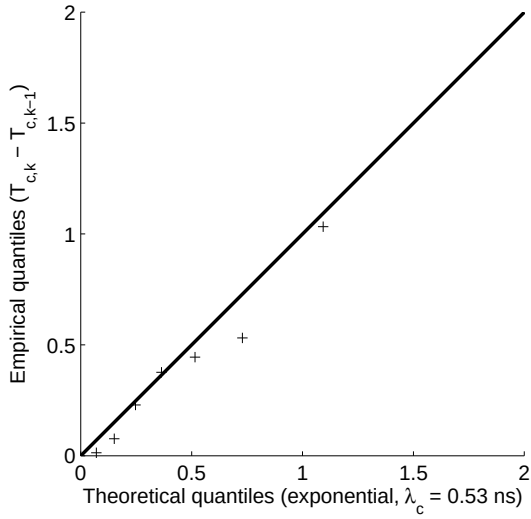

Figure 5.8: QQ plot of quantiles of $T_{c,k} - T_{c,k-1}$ versus quantiles of an exponential distribution for a cluster at measurement location 3

5.4.4 Power $P_{c,k}$

A natural model for the fading of MPC powers $P_{c,k}$ in cluster c is the lognormal fading model [31, 32]. For cluster c, it is investigated whether the samples $P_{c,k}$ on a dB-scale could originate from a normal distribution. The normal PDF $p_{\mathrm{norm}}(P_{c,k}\ [\mathrm{dB}]\ ;\ \mu_c, \sigma_c)$ is parameterized by the mean μ_c and the standard deviation σ_c of $P_{c,k}$ in dB:

$$p_{\mathrm{norm}}\left(P_{c,k}\ [\mathrm{dB}]\ ;\ \mu_c, \sigma_c\right) = \frac{1}{\sqrt{2\pi\sigma_c^2}} \exp\left[-\frac{\left(P_{c,k}\ [\mathrm{dB}] - \mu_c\right)^2}{2\sigma_c^2}\right] \tag{5.17}$$

The distributional parameters are estimated by their MLEs, i.e., the sample mean and sample standard deviation of the $P_{c,k}$ samples in dB. Composite normality of $P_{c,k}$ [dB] is assessed with a few statistical tests in literature such as

the AD test [30], the Shapiro-Wilk (SW) test [33], and the Henze-Zirkler (HZ) test [34]. Multiple tests for normality are executed as no uniformly most powerful test exists against all possible alternative distributions. The AD, SW, and HZ tests are generally considered to be relatively powerful against a variety of alternatives. Of the 45 clusters in this measurement campaign, normality of $P_{c,k}$ [dB] is retained at the 5% significance level for 39, 38, and 40 clusters with the AD, SW, and HZ tests, respectively. For the 45 clusters, average p-values are 0.38 (AD), 0.43 (SW), and 0.44 (HZ). Concluding, normality for $P_{c,k}$ [dB] is assumed in the following, as the majority of clusters pass the different GOF tests.

5.5 Statistics of the distributional parameters

This section models the inter-cluster and intra-cluster propagation parameters laid out in the signal model of Section 5.3 in equations (5.1), (5.3), and (5.4). The inter-cluster and intra-cluster propagation parameters are fully determined by the distributional parameters of the location-scale distributions of the previous section. In the following, the inter-cluster propagation parameters are identified with the location parameters of the distributions, i.e., for cluster c:

$$\begin{aligned} \phi_c^A &\triangleq \alpha_c^A \quad \text{(von Mises circular mean of AOAs)} \\ \phi_c^D &\triangleq \alpha_c^D \quad \text{(von Mises circular mean of AODs)} \\ \tau_c &\triangleq \theta_c \quad \text{(onset of delays)} \\ p_c &\triangleq \mu_c \quad \text{(normal mean of powers in dB)} \end{aligned} \tag{5.18}$$

The intra-cluster propagation parameters are characterized by the scale parameters of the distributions, i.e., for the MPCs in cluster c:

$$\begin{aligned} \phi_{c,k}^A &\rightarrow \kappa_c^A \quad \text{(von Mises concentration of AOAs)} \\ \phi_{c,k}^D &\rightarrow \kappa_c^D \quad \text{(von Mises concentration of AODs)} \\ \tau_{c,k} &\rightarrow \lambda_c \quad \text{(exponential mean waiting time between delays)} \\ p_{c,k} &\rightarrow \sigma_c \quad \text{(normal standard deviation of powers in dB)} \end{aligned} \tag{5.19}$$

In the following, the statistics of the distributional parameters are discussed. Preliminarily, correlations between these parameters are investigated. In this section, distinction is made between distributional parameters originating from LOS and NLOS measurements, and it is assessed whether the parameters' statistics differ significantly between LOS and NLOS. A summary of this section's results is found in Table 5.2 (third and fourth column) on page 128.

5.5.1 Correlations

Spearman's rank correlation coefficient is calculated between the location and scale parameters, and the two number parameters n_C and $n_{P,c}$. 45 samples for each of these parameters are available (45 clusters in this campaign). Figs. 5.9(a) and 5.9(b) show the upper triangles of the correlation matrices of estimated parameters stemming from LOS and from NLOS measurements. The correlation coefficient's value is color coded according to the color scale to the right of each matrix. Permutation tests are carried out to decide on the significance of each of the correlations. Correlation coefficients which prove to significantly differ from zero at a 5% level are marked with the text "5%". Correlation coefficients which are different from zero at the more strict 1% significance level are marked with a "1%" label. For correlations without a label, the permutation test accepted the hypothesis of zero correlation at the 5% significance level.

Firstly, we look at the correlations between the distributional parameters in (5.18) and (5.19) (part of the correlation matrices inside the dashed rectangles in Figs. 5.9(a) and 5.9(b)). Most notably, the correlation between cluster mean power p_c and cluster onset τ_c proves to be strong at the 1% significance level, and this for both LOS (negative correlation of -0.80, p-value of $1.8 \cdot 10^{-4}$) and NLOS (negative correlation of -0.58, p-value of $9.7 \cdot 10^{-4}$). This is well-established in the SV model, where linear cluster power is modelled as exponentially decaying with cluster delay (see formula (4.3) and [26]). This strong correlation can not be easily ignored, so p_c is modelled through regression with τ_c in the following. Additionally in Fig. 5.9, some correlations are significant at the 5% level but not at the 1% level. These correlations can sometimes be explained from the expected propagation physics: for example, regarding the positive correlation of 0.37 between σ_c and λ_c in NLOS, it is expected that the variability of MPC power σ_c will be larger if the MPCs are characterized by a larger λ_c, i.e., have delays that are further in between. For simplicity of the provided models, we choose to not perform regression between distributional parameters for which the correlation is significant at the 5% level but not at the 1% level, also because these correlations are between different distributional parameters for LOS and NLOS. Summarizing, the distributional parameters will be modelled by their marginal statistical distributions in the next sections, except for the mean cluster power p_c which strongly depends on the cluster onset τ_c.

Secondly, we look at the correlations with the number parameters n_C and $n_{P,c}$ (part of the correlation matrices outside the dashed rectangles in Figs. 5.9(a) and 5.9(b)). For our measurements, no model is provided for the number of paths per cluster $n_{P,c}$: MPC parameter extraction in Section 5.2.3.1 estimated the 100 strongest MPCs without deciding on the actual number of paths through heuristics. Nevertheless, the significant correlations with $n_{P,c}$ in Fig. 5.9 can give information about the effect of the number of paths per cluster on the

estimation accuracy of other cluster parameters, in particular scale (dispersion) parameters. For example at the 1% level, the correlation between $n_{P,c}$ and λ_c is significant for both LOS (negative correlation of -0.73) and NLOS (negative correlation of -0.61). As clusters contain paths with similar delay characteristics, it can be expected that a larger number of paths $n_{P,c}$ will yield closer spacing of these paths on the delay axis, i.e., smaller estimated values of λ_c. In contrast to this, the estimation of the other scale parameters κ_c^A, κ_c^D, and σ_c does not seem to be greatly affected by $n_{P,c}$. In Fig. 5.9(a), the number of clusters n_C is not strongly correlated with the distributional parameters for the LOS measurements. In Fig. 5.9(b) for NLOS, the correlation between n_C and the location ϕ_c^A of the clusters on the AOA axis is significant at the 5% level (negative correlation of -0.39). However, as there is no physical basis to assume that the arrival angle of a cluster should depend on the total number of arriving clusters, this correlation will not be taken into account while modelling the statistics of n_C.

From the data in Fig. 5.9, the conclusion is that a majority of the correlations can assumed to be zero, which means the multivariate postulation can be weakened without completely moving to the univariate assumption. Future work on this topic is to investigate whether or not omitting correlations which are assumed to be zero would significantly degrade channel matrix estimates. Finally, we compare the correlation analysis in this section with the observations made in [35]. In this work, strong correlations between spreads in the AOA, AOD, and delay domains are found, i.e., clusters are small or large in all domains at once. These strong correlations are not found for our measurements (see the correlations between the scale parameters in Fig. 5.9), except for LOS were κ_c^A and κ_c^D show significant correlation. Contrary to [35], where a LOS/obstructed LOS scenario is considered, our measurements also include a heavy NLOS scenario with propagation through walls. For our NLOS case, cluster spreads in all domains appear to be decorrelated. For our LOS case, the azimuthal spreads are significantly correlated as in [35]. However, in contrast to this work, correlation with delay spread is weak for our measurements, which is likely caused by our LOS cases being restricted to hallway propagation.

5.5.2 Location parameters (inter-cluster)

This section discusses the statistics of the distributional location parameters, as defined in equation (5.18).

5.5.2.1 Cluster angular means ϕ_c^A and ϕ_c^D

In indoor environments, multipath clusters result from scattering of a group of closely spaced physical objects, e.g., a desk with computer equipment and of-

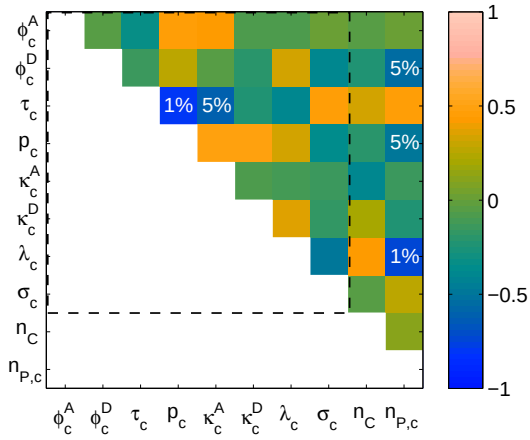

(a) LOS measurements

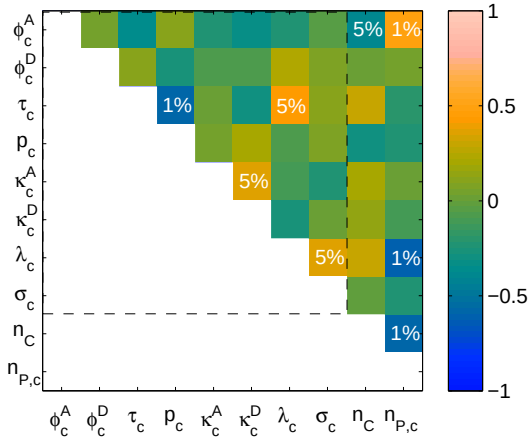

(b) NLOS measurements

Figure 5.9: Spearman's correlation of distributional and number parameters

fice supplies, the drawers of a file cabinet, etc. The cluster mean AOA and mean AOD depend on the position of these groups of scatterers relative to the Rx and Tx. Without prior information on the layout of objects, possible scatterers can assumed to be positioned randomly in the propagation environment. Together with random locations of the Tx and Rx, this means that from a modeling perspective there is no physical basis for a certain mean AOA or AOD to have a higher probability of occurrence than another mean AOA or AOD. For this reason, the uniform distribution is most suitable for modelling ϕ_c^A and ϕ_c^D. In this section, no distinction is made between LOS and NLOS, because the uniform distribution is not parameterized by any distributional parameter (which could change between these two

circumstances). The PDF of a uniform distribution in $(-\pi, \pi]$ for ϕ_c^A and ϕ_c^D is given by:

$$p_{\text{uni}}\left(\phi_c^A\right) = p_{\text{uni}}\left(\phi_c^D\right) = \frac{1}{2\pi} \tag{5.20}$$

The premise of a uniform distribution in $(-\pi, \pi]$ for the inter-cluster mean azimuth angles is validated through statistical hypothesis tests. In [5], the popular Kolmogorov-Smirnov (KS) test is advocated for GOF of the propagation parameters' underlying distributions. However, for small sample sizes, the KS test is known to have low power. Because of this, we use Rao's spacing test for uniformity [36]. This test has the following advantages over the KS test: it is designed for circular data, has higher power, and is non-parametric which means that no error-prone distributional assumption is made on the test statistic. For both the 45 cluster mean AOAs ϕ_c^A and the 45 cluster mean AODs ϕ_c^D, Rao's spacing test retained the null hypothesis of a uniform distribution in $(-\pi, \pi]$ at the 5% significance level (p-values of 0.67 and 0.14, respectively). Fig. 5.10 shows a QQ plot of empirical quantiles of ϕ_c^A versus theoretical quantiles of a uniform distribution: good agreement between both is established.

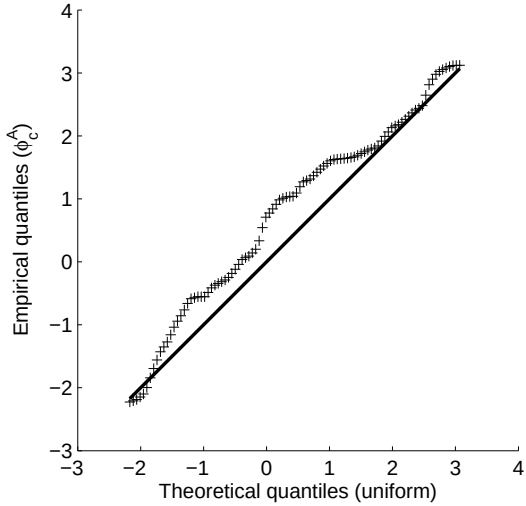

Figure 5.10: QQ plot of quantiles of ϕ_c^A versus quantiles of a uniform distribution

5.5.2.2 Cluster onset τ_c

For consistency with the modelling of the intra-cluster delay in Section 5.4.3, we also adopt the SV model for the inter-cluster delay: the waiting time between the

onsets $\tau_c - \tau_{c-1}$ of two consecutively arriving clusters is modelled by an exponential distribution (see formula (4.4) and [26]). The exponential PDF is fully parameterized by the mean waiting time $\mathrm{E}[\tau_c - \tau_{c-1}]$:

$$p_{\exp}\left(\tau_c \,|\tau_{c-1}\,;\, \mathrm{E}[\tau_c - \tau_{c-1}]\right) = \frac{1}{\mathrm{E}[\tau_c - \tau_{c-1}]} \exp\left[-\frac{\tau_c - \tau_{c-1}}{\mathrm{E}[\tau_c - \tau_{c-1}]}\right] \quad (5.21)$$

Under the assumption of an exponential distribution, it is first investigated whether the waiting time between clusters differs between LOS and NLOS measurements. This is done by executing the two-sample AD test, which assesses whether the two groups of $\tau_c - \tau_{c-1}$ samples coming from LOS and NLOS could have originated from the same statistical distribution. This test results in a p-value of 0.04, which is borderline significant at the 5% level and prompts us to distinguish between LOS and NLOS. Next, for LOS and NLOS separately, composite exponentiality of $\tau_c - \tau_{c-1}$ is verified using the one-sample AD test. An exponential distribution is accepted for both LOS and NLOS at the 5% significance level (p-values of 0.13 and 0.12, respectively). The mean waiting time $\mathrm{E}[\tau_c - \tau_{c-1}]$ is estimated at 2.30 ns for LOS and 1.21 ns for NLOS. Clusters seem to arrive in more rapid succession in NLOS than in LOS, which could be due to the choice of measurement locations in Fig. 5.2. For the NLOS measurements at least either the Tx or Rx are located in an office, while the LOS measurements are strictly hallway to hallway propagation. The offices have smaller dimensions and contain more closely spaced groups of scatterers (desks, etc.) than the hallway, which renders them more likely to produce clusters closer in the delay domain.

Other measurement campaigns in offices which used the SV model found mean waiting times between cluster onsets ranging from 27 to 60 ns [37, 38]. These larger values compared to our measurements could be attributed to the fact that measurements in literature clustered propagation paths based only on path delay. The two extra dimensions (two azimuth angles) used in our clustering procedure increase the discriminatory power of the clustering, i.e., more clusters can be distinguished between. It is therefore expected that joint AOA/AOD/delay clustering results in clusters more closely spaced in the delay domain.

5.5.2.3 Cluster mean power p_c

For both LOS and NLOS, significant correlation was found between cluster mean power p_c and cluster onset τ_c in Section 5.5.1. In literature, two commonly used models exist for the monotonic decay of p_c with increasing τ_c. The first model (SV model) proposes a linear decrease of the average p_c of MPC powers in dB with the cluster onset τ_c (exponential law (4.3)) [26]. The second model proposes a linear decrease of p_c in dB with the logarithm of τ_c (power law) [31].

$$p_c\,[\text{dB}] = a_0 + a_1 \cdot \tau_c\,[\text{ns}] + a_2 \cdot D_c + a_3 \cdot \tau_c\,[\text{ns}] \cdot D_c + \epsilon_c \tag{5.22}$$

$$p_c\,[\text{dB}] = b_0 + b_1 \cdot 10\log\left(\tau_c\,[\text{ns}]\right) + b_2 \cdot D_c + b_3 \cdot 10\log\left(\tau_c\,[\text{ns}]\right) \cdot D_c + \chi_c \tag{5.23}$$

In the models (5.22) and (5.23), p_c (in dB) is made dependent on τ_c (in ns) or $10\log(\tau_c)$ (in dBns) and the dummy variable D_c. The value of D_c is one for clusters stemming from LOS measurements and is zero for NLOS clusters. As such, D_c accounts for possible changes in the intercept and slope of (5.22) and (5.23) between LOS and NLOS situations. Furthermore, a_0 through a_3 and b_0 through b_3 are regression parameters. The terms ϵ_c and χ_c denote the models' errors for cluster c and are generally assumed to be zero-mean normally distributed. The regression parameters a_0 through a_3 and b_0 through b_3 are estimated using a backward elimination procedure [39]: simple t-tests are carried out to determine which of the regression parameters can assumed to be zero at the 5% significance level. For this, several iterations of the models in (5.22) and (5.23) are performed in which regression parameters are estimated and for which the regression parameter with the largest associated p-value is made equal to zero for the subsequent iteration. This is done until the final model only holds non-zero regression parameters with associated p-values smaller than 0.05. The backward elimination procedure resulted in the following estimated regression parameters:

$$a_0 = -20.14\text{ dB}, a_1 = -0.81\text{ dB/ns}, a_2 = 0\text{ dB}, a_3 = 0\text{ dB/ns} \tag{5.24}$$

$$b_0 = -22.35\text{ dB}, b_1 = -0.55, b_2 = 0\text{ dB}, b_3 = 0 \tag{5.25}$$

The standard deviations of ϵ_c in (5.22) and χ_c in (5.23) are estimated at 4.72 dB and 5.09 dB, respectively. In (5.24) and (5.25), it is noted that the regression parameters a_2, a_3, b_2, and b_3 associated with the dummy variable D_c are assumed to be zero at the 5% significance level by the backward elimination procedure. This means that the form of the exponential and power law models is not significantly different between LOS and NLOS measurements[4]. The coefficients of determination for the exponential and power law models are equal to 0.42 and 0.26, respectively. The exponential law model is therefore preferred as it explains a larger part of the variability of p_c than the power law model. Fig. 5.11 shows a scatter plot of p_c versus τ_c along with the fitted exponential law model (5.22).

[4]Note that the difference in path loss experienced in LOS and NLOS situations is already removed by the normalization of (5.2).

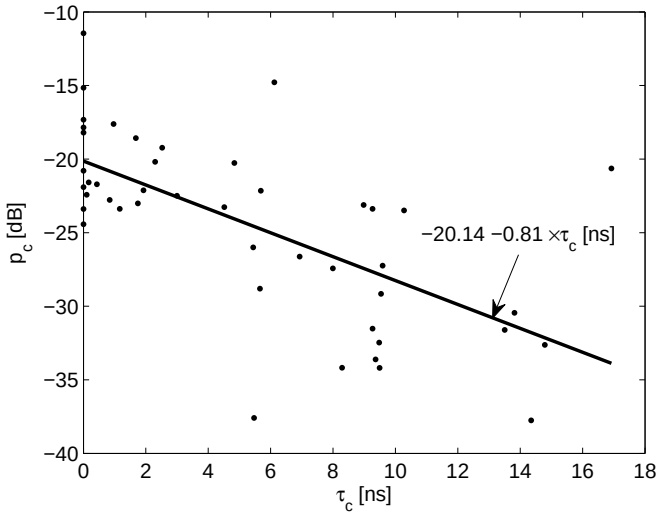

Figure 5.11: Scatter plot of p_c versus τ_c and fitted exponential law model

5.5.3 Scale parameters (intra-cluster)

This section discusses the statistics of the distributional scale parameters in (5.19). To our knowledge, no examples of possible statistical distributions for the scale parameters exist in literature. We will therefore use the entropy-maximizing normal distribution to model these parameters. As the scale parameters can only take on positive values, they are first log-transformed to match the support of the normal distribution (i.e., any positive or non-positive number). Also, log-transformation has the additional benefit of softening the impact of outliers (large values of the scale parameters), which makes it more probable that log-transformed variables are well described by a normal distribution. In the next sections, the premise of a normal distribution is investigated for the log-transformed scale parameters $z_c = \log\left(\kappa_c^A\right)$, $\log\left(\kappa_c^D\right)$, $\log\left(\lambda_c\right)$, and $\log\left(\sigma_c\right)$, with PDF:

$$p_{\text{norm}}\left(z_c\,;\,\mathrm{E}\left[z_c\right],\mathrm{Std}\left[z_c\right]\right) = \frac{1}{\sqrt{2\pi\cdot\mathrm{Std}^2\left[z_c\right]}}\exp\left[-\frac{\left(z_c-\mathrm{E}\left[z_c\right]\right)^2}{2\cdot\mathrm{Std}^2\left[z_c\right]}\right] \quad (5.26)$$

In (5.26), $\mathrm{E}\left[\cdot\right]$ and $\mathrm{Std}\left[\cdot\right]$ represent the mean and standard deviation of their arguments, respectively.

5.5.3.1 Cluster angular concentrations κ_c^A and κ_c^D

For both κ_c^A and κ_c^D, the two-sample AD test detects no difference between LOS and NLOS distributions at the 5% significance level (p-values of 0.16 and 0.20, re-

spectively). Without making distinction between LOS and NLOS, the assumptions of normality for $\log\left(\kappa_c^A\right)$ and $\log\left(\kappa_c^D\right)$ are validated using the statistical tests of Section 5.4.4: the AD, SW, and HZ tests. For $\log\left(\kappa_c^A\right)$, all three tests accepted normality at the 5% level with p-values of 0.37 (AD), 0.46 (SW), and 0.31 (HZ). The sample mean and sample standard deviation of $\log\left(\kappa_c^A\right)$ are equal to 0.50 and 0.33, respectively. Furthermore, normality is also accepted for $\log\left(\kappa_c^D\right)$ with p-values of 0.09 (AD), 0.14 (SW), and 0.59 (HZ). The sample mean and standard deviation of $\log\left(\kappa_c^D\right)$ equal 0.36 and 0.32, respectively.

The concentration parameters κ_c^A and κ_c^D range from 0.42 to 14.73 and from 0.46 to 16.25. For comparison, the von Mises distribution is also proposed for the non-isotropic angular dispersion in outdoor suburban/urban environments in [28]. Herein, the concentration of AOAs perceived by a mobile antenna below rooftop height ranges from 0.6 to 3.3. Compared to our measurement campaign, the AOAs seem to be somewhat less concentrated in outdoor environments, which could be explained from the larger physical structures in outdoor environments which cause scattering in a broader angular range.

5.5.3.2 Cluster mean waiting time between MPCs λ_c

It is first assessed whether λ_c (in ns) originating from LOS or NLOS measurements could have been drawn from the same statistical distribution. A two-sample AD test on λ_c grouped according to LOS or NLOS results in a p-value of 0.19, indicating no significant difference between LOS and NLOS at the 5% level. Next, normality for $\log\left(\lambda_c\right)$ without making distinction between LOS and NLOS is considered: AD, SW, and HZ hypothesis tests accepted normality at the 5% level with p-values of 0.13, 0.21, and 0.13, respectively. We therefore assume a normal distribution for $\log\left(\lambda_c\right)$: the sample mean and sample standard deviation of $\log\left(\lambda_c\right)$ are equal to 0.03 and 0.35, respectively.

The parameter λ_c varies from 0.23 ns to 6.99 ns between the clusters of all executed MIMO measurements, and is equal to 1.52 ns on average. For comparison, measurements in [37] yielded an average λ_c of about 0.16 ns (estimation of MPC delay using the frequency domain maximum likelihood procedure), while measurements in [38] resulted in an average λ_c of 4 ns (estimation of MPC delay using the inverse discrete Fourier transform or IDFT procedure). These results correspond well with our average λ_c of 1.52 ns, despite that MPC delay is estimated differently using the ESPRIT procedure. These findings are as expected: the arrival rate of clusters is highly dependent on the sort of clustering algorithm that is used, the arrival rate of MPCs however is determined by environment geometry and should therefore not depend on the delay estimation procedure. It is also interesting to note that the average λ_c of 1.52 ns is of the same order as the mean waiting times between consecutive clusters of 2.30 ns for LOS and 1.21 ns for NLOS (see Section 5.5.2.2). This means that the waiting times between clus-

ters are not necessarily larger than the waiting times between MPCs in a cluster. This is because clustering is not done unidimensionally by only considering the delay domain, but multidimensionally by jointly considering the AOA/AOD/delay space.

5.5.3.3 Cluster standard deviation of power σ_c

For σ_c (in dB), a two-sample AD test decides there is no significant change in the statistical distribution of this parameter between LOS and NLOS measurements (p-value of 0.34). Normality for $\log(\sigma_c)$ is assessed with the AD, SW, and HZ hypothesis tests, all of which accepted normality at the 5% level (p-values of 0.61, 0.78, and 0.41, respectively). The sample mean and sample standard deviation of $\log(\sigma_c)$ are equal to 0.88 and 0.14, respectively. Fig. 5.12 shows a QQ plot of empirical quantiles of $\log(\sigma_c)$ versus theoretical quantiles of a normal distribution: good agreement between both can be seen.

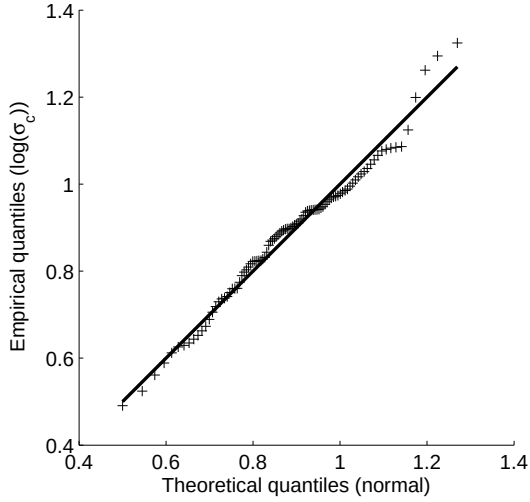

Figure 5.12: QQ plot of quantiles of $\log(\sigma_c)$ versus quantiles of a normal distribution

5.5.4 Number of clusters

In literature, the number of clusters n_C in geometry-based stochastic channel models is characterized in various ways. In [7], the probability density function of n_C follows from marginalizing a continuous multivariate distribution. A possible issue with this approach is that samples of n_C drawn from a continuous distribution have to be rounded to integer values, as n_C is a discrete variable. For other channel models the number of clusters is fixed. For example in [4], n_C is equal to 6,

while in [5], n_C in indoor office environments is assumed to be 12 in LOS conditions and 16 in NLOS conditions. In [16], the number of clusters is modeled by a discrete probability distribution, n_C is found to be a minimum value of 3 plus a Poisson distributed random variable. Herein, the mean number of clusters is found equal to 4.69. The number of clusters varies to some extent between reports in literature, this is however expected, as the number of cluster will greatly depend on the adopted definition of clusters and the sort of clustering algorithm used.

For our measurements, there is no significant difference in the statistical distribution of n_C between LOS and NLOS, as concluded by a two-sample AD test at the 5% level (p-value of 0.87). As in [16], the Poisson distribution is also adopted here for the number of clusters n_C, as it is a natural candidate distribution for the number of events occurring in a specified (time) interval. For example, the Poisson distribution has already been applied to the number of paths characterization problem in [40]. The minimum number of clusters for the K-power-means clustering algorithm in Section 5.2.3.2 is set to 2. Therefore, the number of clusters n_C is modelled as a minimum value of 2 plus a Poisson distributed random variable. The probability density function $p_{\text{poiss}}(n_C\,;\,\eta)$ of n_C is written as:

$$p_{\text{poiss}}(n_C\,;\,\eta) = \frac{(\eta-2)^{n_C-2}\,e^{-(\eta-2)}}{(n_C-2)!} \qquad (n_C \geq 2) \tag{5.27}$$

In (5.27), the distributional parameter η is the mean number of detected clusters. The MLE for η is the sample mean of n_C and equals 5.00 for our measurements. This value is comparable to a mean number of clusters equal to 4.69 found in [16]. Herein, clustering is also done with the K-power-means algorithm and by using the Kim-Parks index. A KS GOF test accepted the Poisson distribution for n_C in (5.27) at the 5% significance level with a p-value of 0.50.

5.6 Conclusions

In this chapter, directional MIMO measurements in an indoor office environment have been presented. Measurements were performed through frequency-domain channel sounding in the 3.5 GHz band. The spatial structure of the channel was captured by 10 by 4 URAs at both link ends. The antenna arrays were created using the virtual array technique. From these measurements, parameters associated with discrete propagation paths were extracted using a joint 5D ESPRIT estimation algorithm. The estimated path parameters included AOA, AOD, delay, and power. In agreement with the geometry-based stochastic type of MIMO channel models, the path parameters were grouped into clusters using the statistical K-power-means algorithm.

Statistical distributions of the propagation parameters within individual clus-

MPC parameter	Intra-cluster distribution	Inter-cluster and intra-cluster parameters	Statistical modelling
$\Phi_{c,k}^{A}$ [rad]	von Mises	(inter) ϕ_c^A [rad]	*uniformly distributed*
		(intra) κ_c^A [-]	*lognormally distributed*
			$\mathrm{E}\left[\log\left(\kappa_c^A\right)\right]$ = 0.50
			$\mathrm{Std}\left[\log\left(\kappa_c^A\right)\right]$ = 0.33
$\Phi_{c,k}^{D}$ [rad]	von Mises	(inter) ϕ_c^D [rad]	*uniformly distributed*
		(intra) κ_c^D [-]	*lognormally distributed*
			$\mathrm{E}\left[\log\left(\kappa_c^D\right)\right]$ = 0.36
			$\mathrm{Std}\left[\log\left(\kappa_c^D\right)\right]$ = 0.32
$T_{c,k}$ [ns]	exponential	(inter) τ_c [ns]	*exponentially distributed*
			$\mathrm{E}\left[\tau_c - \tau_{c-1}\right]$ = 2.30 ns (LOS)
			and 1.21 ns (NLOS)
		(intra) λ_c [ns]	*lognormally distributed*
			$\mathrm{E}\left[\log\left(\lambda_c\right)\right]$ = 0.03
			$\mathrm{Std}\left[\log\left(\lambda_c\right)\right]$ = 0.35
$P_{c,k}$ [-]	lognormal	(inter) p_c [dB]	$= -20.14 - 0.81 \cdot \tau_c$ [ns] $+ \epsilon_c$
			ϵ_c zero-mean normally distributed
			with standard deviation 4.72 dB
		(intra) σ_c [dB]	*lognormally distributed*
			$\mathrm{E}\left[\log\left(\sigma_c\right)\right]$ = 0.88
			$\mathrm{Std}\left[\log\left(\sigma_c\right)\right]$ = 0.14

Number parameter	Statistical modelling
n_C [-]	*Poisson distributed*
	η = 5.00

Table 5.2: Summary of statistical modelling of MPC parameters with clustering

ters were determined, and correlations between these parameters were assessed. Motivated choices for the statistical distributions were made, based on the propagation physics expected in office environments. The distributional location and scale parameters were subsequently used to characterize the intra-cluster and inter-cluster dynamics of the MPC parameters. This was done by in turn determining the statistical distributions of these location and scale parameters, and by considering their correlations. To validate the distributional choices made in this chapter, the GOF to the proposed distributions was verified using a number of statistical hypothesis tests with sufficient power. The most important results of the statistical

analysis are summarized in Table 5.2.

Additionally, a new notation for the MIMO channel matrix was given which more visibly shows the clustered nature of propagation paths. This notation is named FABLE. Future work includes the use of FABLE as the signal model in multipath estimation algorithms such as ESPRIT. The conventional signal model of these algorithms currently does not take clustering into account.

References

[1] L. Schumacher, K. I. Pedersen, and P. E. Mogensen. *From Antenna Spacings to Theoretical Capacities - Guidelines for Simulating MIMO Systems*. In Proceedings of the 13th IEEE International Symposium on Personal, Indoor, and Mobile Radio Communications, pages 314–319, Lisbon, PT, September 2002.

[2] C. Oestges and B. Clerckx. *MIMO Wireless Communications: From Real-World Propagation to Space-Time Code Design*. Academic Press, first edition, 2007.

[3] J. J. Blanz and P. Jung. *A Flexibly Configurable Spatial Model for Mobile Radio Channels*. IEEE Transactions on Communications, 46(3):367–371, March 1998.

[4] 3rd Generation Partnership Project. *Spatial Channel Model for MIMO Simulations*. Technical report, 3GPP Technical Specification Group Radio Access Network, 2008. ref.: 3GPP TR 25.996 v8.0.0, online: www.3gpp.org.

[5] P. Kyösti, J. Meinilä, L. Hentilä, X. Zhao, T. Jämsä, C. Schneider, M. Narandzić, M. Milojević, A. Hong, J. Ylitalo, V.-M. Holappa, M. Alatossava, R. Bultitude, Y. de Jong, and T. Rautiainen. *Winner II Channel Models*. Technical report, IST-WINNER, 2008. ref.: D1.1.2 v1.2, online: www.ist-winner.org.

[6] L. M. Correia. *Mobile Broadband Multimedia Networks - Techniques, Models, and Tools for 4G*. Elsevier Ltd., first edition, 2006.

[7] N. Czink. *The Random-Cluster Model - A Stochastic MIMO Channel Model for Broadband Wireless Communication Systems of the 3rd Generation and Beyond*. PhD thesis, Technische Universität Wien, Forschungszentrum Telekommunikation Wien, Wien, AT, 2007.

[8] A. J. Levy. *Fine Structures of the Urban Mobile Propagation Channel*. In Proceedings Commsphere, pages 5.1.1–5.1.6, Herzliya, IL, December 1991.

[9] V. I. Vasylyshyn. *Closed-Form DOA Estimation with Multiscale Unitary ESPRIT Algorithm*. In European Radar Conference (EURAD), pages 317–320, Amsterdam, NL, October 2004.

[10] M. Haardt. *Efficient One-, Two-, and Multidimensional High-Resolution Array Signal Processing*. PhD thesis, Technische Universität München, Shaker Verlag GmbH, Aachen, DE, 1996.

[11] M. Landmann and R. Thomä. *Common Pitfalls in Multidimensional High Resolution Channel Parameter Estimation*. In Proceedings of the 5th IEEE Signal Processing Education Workshop and 13th Digital Signal Processing Workshop (SPE/DSP), pages 314–319, Marco Island, FL, US, January 2009.

[12] J. Fuhl, J.-P. Rossi, and E. Bonek. *High-Resolution 3-D Direction-of-Arrival Determination for Urban Mobile Radio*. IEEE Transactions on Antennas and Propagation, 45(4):672–682, April 1997.

[13] M. Haardt and J. A. Nossek. *Simultaneous Schur Decomposition of Several Nonsymmetric Matrices to Achieve Automatic Pairing in Multidimensional Harmonic Retrieval Problems*. IEEE Transactions on Signal Processing, 46(1):161–169, January 1998.

[14] T. J. Shan, M. Wax, and T. Kailath. *On Spatial Smoothing for Direction-of-Arrival Estimation of Coherent Signals*. IEEE Transactions on Acoustics, Speech, and Signal Processing, 33(4):806–811, August 1985.

[15] X. Li and K. Pahlavan. *Super-Resolution TOA Estimation with Diversity for Indoor Geolocation*. IEEE Transactions on Wireless Communications, 3(1):224–234, January 2004.

[16] F. Quitin, C. Oestges, F. Horlin, and P. De Doncker. *Cluster Parametrisation for Indoor Polarized MIMO Channels*. In COST 2100 8th Management Committee Meeting, Valencia, ES, May 2009. ref.: TD(09) 818.

[17] N. Czink, P. Cera, J. Salo, E. Bonek, J.-P. Nuutinen, and J. Ylitalo. *A Framework for Automatic Clustering of Parametric MIMO Channel Data Including Path Powers*. In IEEE Vehicular Technology Conference, pages 1–5, Montréal, CA, September 2006.

[18] N. Czink, P. Cera, J. Salo, E. Bonek, J.-P. Nuutinen, and J. Ylitalo. *Improving Clustering Performance Using Multipath Component Distance*. IET Electronics Letters, 42(1):33–35, January 2006.

[19] D.-J. Kim, Y.-W. Park, and D.-J. Park. *A Novel Validity Index for Determination of the Optimal Number of Clusters*. IEICE Transactions on Information and Systems, E84-D(2):281–285, February 2001.

[20] L. Materum, J.-I. Takada, I. Ida, and Y. Oishi. *Mobile Station Spatio-Temporal Multipath Clustering of an Estimated Wideband MIMO Double-Directional Channel of a Small Urban 4.5 Ghz Macrocell*. EURASIP Journal on Wireless Communications and Networking, February 2009. online: http://dx.doi.org/10.1155/2009/804021.

[21] N. Czink, X. Yin, H. zcelik, M. Herdin, E. Bonek, and B. H. Fleury. *Cluster Characteristics in a MIMO Indoor Propagation Environment*. IEEE Transactions on Wireless Communications, 6(4):1465–1474, April 2007.

[22] M. Steinbauer, A. F. Molisch, and E. Bonek. *The Double-Directional Radio Channel*. IEEE Antennas and Propagation Magazine, 43(4):51–63, August 2001.

[23] A. Nasr, M. Lienard, and P. Degauque. *Extraction of Cluster Parameters from a Block-diagonal Form of the Channel Matrix*. In COST 2100 4th Management Committee Meeting, Wroclaw, PL, February 2008. ref.: TD(08) 448.

[24] E. Tanghe, W. Joseph, M. Lienard, A. Nasr, P. Stefanut, D. Gaillot, P. Degauque, and L. Martens. *Clustering of Channel Parameters by Block Diagonal Matrix Decomposition*. In COST 2100 7th Management Committee Meeting, Braunschweig, DE, February 2009. ref.: TD(09) 712.

[25] J. L. Myers and A. D. Well. *Research Design and Statistical Analysis*. Lawrence Erlbaum, second edition, 2002.

[26] A. A. M. Saleh and R. A. Valenzuela. *A Statistical Model for Indoor Multipath Propagation*. IEEE Journal on Selected Areas in Communications, 5(2):128–137, February 1987.

[27] Q. Spencer, M. Rice, B. Jeffs, and M. Jensen. *A Statistical Model for Angle of Arrival in Indoor Multipath Propagation*. In IEEE Vehicular Technology Conference, volume 3, pages 1415–1419, Phoenix, AZ, US, May 1997.

[28] A. Abdi, J. A. Barger, and M. Kaveh. *A Parametric Model for the Distribution of the Angle of Arrival and the Associated Correlation Function and Power Spectrum at the Mobile Station*. IEEE Transactions on Vehicular Technology, 51(3):425–434, May 2002.

[29] V. Erceg, L. Schumacher, P. Kyritsi, A. Molisch, D. S. Baum, A. Y. Gorokhov, C. Oestges, Q. Li, K. Yu, N. Tal, B. Dijkstra, A. Jagannatham, C. Lanzl, V. J. Rhodes, J. Medbo, D. Michelson, and M. Webster. *TGn Channel Models*. Technical report, IEEE P802.11 Wireless LANs, 2004. ref.: IEEE 802.11-03/940r4, online: www.ieee802.org/11.

[30] T. W. Anderson and D. A. Darling. *Asymptotic Theory of Certain "Goodness of Fit" Criteria Based on Stochastic Processes*. Annals of Mathematical Statistics, 23(2):193–212, 1952.

[31] S. R. Saunders. *Antennas and Propagation for Wireless Communication Systems*. Wiley and Sons, 1999.

[32] A. F. Molisch, J. R. Foerster, and M. Pendergrass. *Channel Models for Ultrawideband Personal Area Networks*. IEEE Wireless Communications, 10(6):14–21, December 2003.

[33] S. S. Shapiro and M. B. Wilk. *An Analysis of Variance Test for Normality (Complete Samples)*. Biometrika, 52(3/4):591–611, December 1965.

[34] N. Henze and B. Zirkler. *A Class of Invariant Consistent Tests for Multivariate Normality*. Communications in Statistics - Theory and Methods, 19(10):3595–3617, 1990.

[35] N. Czink, E. Bonek, L. Hentil, P. Kysti, J.-P. Nuutinen, and J. Ylitalo. *The Interdependence of Cluster Parameters in MIMO Channel Modeling*. In Proceedings of the first European Conference on Antennas and Propagation (EuCAP), pages 1–6, Nice, FR, November 2006.

[36] E. Batschelet. *Circular statistics for biology*. Academic Press, 1981.

[37] P. Pagani and P. Pajusco. *Experimental Analysis of the Ultra Wideband Propagation Channel over the 3.1 GHz-10.6 GHz Frequency Band*. In Proceedings of the IEEE International Symposium on Personal, Indoor, and Mobile Radio Communications, pages 1–5, Helsinki, FI, September 2006.

[38] I. Marinović, I. Zanchi, and Z. Blažević. *Estimation of Channel Parameters for "Saleh-Valenzuela" Model Simulation*. In Proceedings of the International Conference on Applied Electromagnetics and Communications, pages 1–4, Dubrovnik, HR, October 2005.

[39] M. H. Kutner, C. J. Nachtsheim, J. Neter, and W. Li. *Applied Linear Statistical Models*. McGraw-Hill/Irwin, fifth edition, 2005.

[40] X. Zhao, J. Kivinen, P. Vainikainen, and K. Skog. *Propagation Characteristics for Wideband Outdoor Mobile Communications at 5.3 GHz*. IEEE Journal on Selected Areas in Communications, 20(3):507–514, April 2002.

6 Penetration loss in a vehicular environment

6.1 Introduction

In spite of their importance in coverage predictions, measurements of the vehicle penetration loss are scarce in the literature [1–3]. This chapter presents vehicle penetration loss measurements and simulations performed at 600, 900, 1800, and 2400 MHz for two different in-vehicle antenna orientations. These frequency bands are often used in today's wireless networks: Digital Video Broadcasting - Terrestrial/Handheld (DVB-T/H) at 600 MHz, Global System for Mobile communication (GSM) at 900 MHz and 1800 MHz, and IEEE 802.11b/g/n at 2400 MHz. Measurement values presented here can be used in the design of wireless networks which aim to provide in-vehicle coverage. The outline of this chapter is as follows. In Section 6.2, a method for vehicle penetration loss measurements and simulations is described. In Section 6.3, measurement and simulation results are presented. Section 6.4 compares our penetration loss results to previous measurements from literature. Finally, conclusions are drawn in Section 6.5.

6.2 Method

6.2.1 Measurements

Vehicle Penetration Loss (VPL), expressed in dB, is defined as the ratio of the received power P_{out} immediately outside the vehicle to the received power P_{in} inside the vehicle [1]:

$$\mathrm{VPL} = 10 \cdot \log\left(\frac{P_{out}}{P_{in}}\right) \tag{6.1}$$

In the following, the experimental setup used to measure vehicle attenuation characteristics is described. Next, a motivation for using the proposed experimental setup is provided.

6.2.1.1 Experimental setup

VPL measurements were performed with a mini-van along several streets in a suburban environment located in Ghent, Belgium. Measurements were made by driving the mini-van in Line Of Sight (LOS) of a transmitting antenna (Tx). The drives started at approximately 3 m from the Tx and ended at about 75 m from the Tx. Fig. 6.1 presents a view of one of the streets in the suburban environment. Fig. 6.2 shows the measurement setup, consisting of a transmitter and a receiver part. The Tx was mounted vertically approximately 3 m above ground level on a telescopic mast. As Tx, vertically polarized omnidirectional dipole antennas were used. A signal generator was used to inject a continuous wave signal into the Tx antenna. The input power to the Tx antenna was about 24 dBm for the investigated frequencies.

As the receiving antenna (Rx), omnidirectional antennas of the same type as the Tx were used. For each frequency two identical Rx antennas were used. One Rx, noted as $\mathrm{Rx_{out}}$, was mounted vertically on a mast outside the mini-van at the same height as the Tx. $\mathrm{Rx_{out}}$ was raised 1.25 m above the metallic vehicle rooftop to minimize reflections. The second Rx, noted as $\mathrm{Rx_{in}}$, was installed in the vehicle once vertically and once horizontally oriented between the driver seat and the passenger seat, approximately 0.6 m above the vehicle's bottom plate. Both receiving antennas were connected to a spectrum analyzer with identical coaxial cables. The spectrum analyzer span was set to 100 kHz, and a resolution bandwidth of 3 kHz was chosen. These settings effectuated a noise floor of approximately -95 dBm. Power levels at the different frequencies were sampled at a rate of 14 samples per second for both $\mathrm{Rx_{out}}$ and $\mathrm{Rx_{in}}$, while the mini-van was driven at a fairly constant

Figure 6.1: Street in the suburban environment

speed of 1 to 2 km/h along a street in LOS of the Tx. Variations in the vehicle's speed were monitored with a Global Positioning System (GPS) device.

Following the measurements, the recorded power levels were linearly averaged over distances equal to 10 wavelengths in order to remove small-scale fading [4]. Averaged power data obtained from $\mathrm{Rx_{out}}$ ($\mathrm{Rx_{in}}$) was used as P_{out} (P_{in}) in formula (6.1) to calculate samples of the VPL. During the measurements, several factors were varied to investigate their effect on the vehicle penetration loss. First,

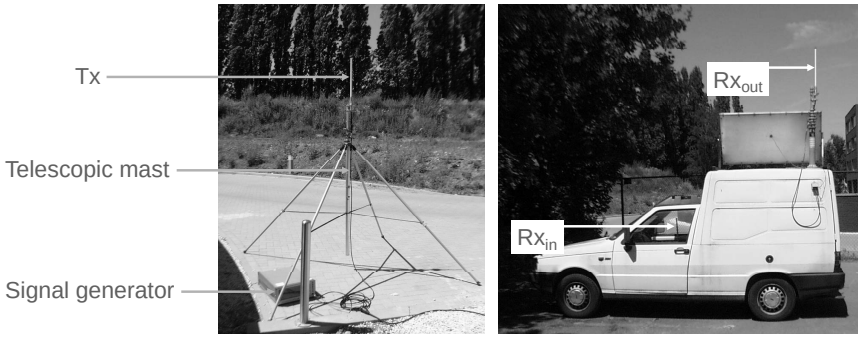

(a) Transmitter (b) Receiver

Figure 6.2: Measurement setup

a distinction has been made between situations where the propagating wave was incident to the rear or to the front of the vehicle. Secondly, $\mathrm{Rx_{in}}$ was mounted alternating vertically and horizontally in successive measurements, in order to determine the effect of antenna orientation on the VPL. Both antenna orientations are equally important in everyday use: vertical orientation represents e.g., a person holding a mobile to his or her head, while horizontal orientation may be a mobile phone lying on a seat [1]. For each center frequency, illuminated vehicle side (rear or front), and in-vehicle antenna orientation (vertical or horizontal), two drives of approximately 72 m length were executed in two different suburban streets.

6.2.1.2 Motivation for the experimental setup

VPL measurements in [2] and [3] were performed on an antenna pattern range, where the vehicle was rotated in LOS with the Tx in an open outdoor environment. We did not choose to perform measurements of the vehicle penetration loss on an antenna pattern range because we wanted to provide loss values which could be expected in a true multipath environment. In a true multipath environment, waves reflected off the buildings and off the ground impinge on all (or most) of the vehicle's windows simultaneously. This corresponds to a more realistic situation where waves enter the vehicle from various directions at once, instead of a single LOS component entering through one or two windows for measurements on an antenna pattern range. However, we want to note that, albeit measurements on an antenna pattern range do not account for the true multipath environment, they do allow to measure the directional attenuation characteristics of a vehicle. Directional attenuation models are valuable when combined with a model for the angular distribution of received power in a specific propagation environment.

The choice of LOS measurements was made to incorporate the effect of polarization mismatch into the measurement data. In LOS circumstances, vertical reception will be favored over horizontal reception because of the vertical orientation of the Tx. Therefore, it is possible to provide best-case (vertical reception) and worst-case (horizontal reception) values of the vehicle penetration loss. In Non Line Of Sight (NLOS) circumstances, waves incident to the in-vehicle antenna would have undergone enough interactions with the environment to cause signal depolarization. NLOS data would therefore not include the effect of polarization mismatch.

Furthermore, we discriminated between front and rear illumination of the vehicle because both sides have distinctly different constructional characteristics in case of a mini-van. These different constructional features again result in a best-case (illumination of the front) and a worst-case (illumination of the rear) signal reception. In a realistic situation when a vehicle is driving in a suburban street, the left and right side of the vehicle will usually be illuminated by secondary reflections off nearby buildings. Therefore, no measurements were performed for direct

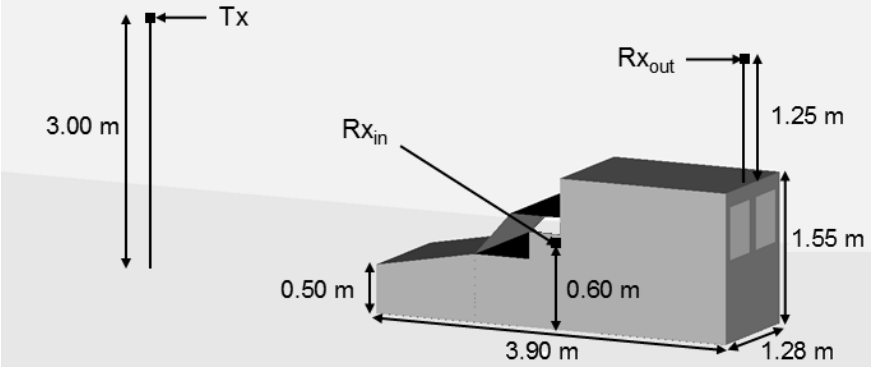

Figure 6.3: Mini-van model for ray-tracing with the vehicle's dimensions and the location of the Tx and Rx

illumination of the left and right vehicle side.

6.2.2 Simulations

A ray-tracing software package (Wireless Insite®) was used to simulate the VPL. The car body of the mini-van was modelled as a box-like structure built mainly from Perfectly Electrically Conducting (PEC) panels. Additional plastic and non-conducting glass faces were also incorporated in the model. The mini-van model used for simulations is shown in Fig. 6.3, along with the vehicle's dimensions and the location of the Tx and Rx. Ground and building reflection in the suburban environment were modelled using PEC planes.

Calculated ray paths were allowed to undergo a maximum of two reflections, one transmission, and one diffraction. The modelled box-like structure gives rise to multiple ray reflections inside the vehicle. Limiting the number of ray interactions takes only the most important contributions to the received power into account. Rays submitted to more interactions would be attenuated by persons and objects within the vehicle in realistic situations [5]. Simulations were performed for different separations between the Tx and the mini-van, to account for the change in Tx positioning relative to the vehicle when it is driven. Two simulated distances between the Tx and the van were spaced 3 cm, corresponding to the average covered distance between two consecutive measurement samples. The simulated received power inside and outside the vehicle was averaged over 10 wavelengths to calculate simulated samples of the VPL using formula (6.1).

6.3 Results

6.3.1 Vehicle penetration losses

6.3.1.1 Fading characteristics

Fig. 6.4 shows the recorded data at 600 MHz of one measurement run along a street in the suburban environment while the Tx illuminated the rear of the minivan and with vertical orientation of $\mathrm{Rx_{in}}$. Fig. 6.4 shows the measured and simulated received power in dBm outside and in-vehicle, prior to averaging over 10 wavelengths.

Outside versus in-vehicle fading characteristics: For the measurement and for the simulation, good tracking between the outside and the in-vehicle power levels is observed in Fig. 6.4: on average, both power levels degrade at approximately the same rate with distance. For the majority of the samples, the received in-vehicle signal level is smaller than the outside signal level, as expected. However, a relatively small number of in-vehicle power samples are larger than the outside level. As can be seen in Fig. 6.4 for both measurements and simulations, this is due to significant fading of the outside received power level, while similar deep fading is not found for the in-vehicle power. The vehicle penetration loss in dB can therefore be negative at some sampling instances. This is somewhat counterintuitive, as vehicle penetration loss in dB is expected to always be a positive value. Why the occurrence of deep fading is exclusive to the outer antenna $\mathrm{Rx_{out}}$ can be explained as follows. At a certain random sampling point, the phases of the dominant MultiPath Components (MPCs) incident to the outer antenna $\mathrm{Rx_{out}}$ could have such values that the MPCs interfere mostly destructive, causing a long, distinct deep fade of the outside received power level[1]. As dominant multipath waves for the outside received power, one can think of the LOS component and the specular reflections off the ground and off the buildings left and right of the vehicle. The in-vehicle received power does not follow the deep fades found in the outside power level because of the lack of dominant MPCs incident to the in-vehicle antenna: most MPCs result from random reflections and scattering inside the vehicle's body. Thus, because the long and deep fades of received power only occur for the outer antenna and not for the in-vehicle antenna, a negative value of the vehicle penetration loss can occasionally be expected.

[1] We do not consider the random MPCs to be part of the dominant incident waves. These random components cause the rapid fluctuations in Fig. 6.4, with local minima spaced half a wavelength to a wavelength apart (i.e., the small-scale fading). The power in these random components would not be large enough to cause the longer, deeper fades in the outside received power.

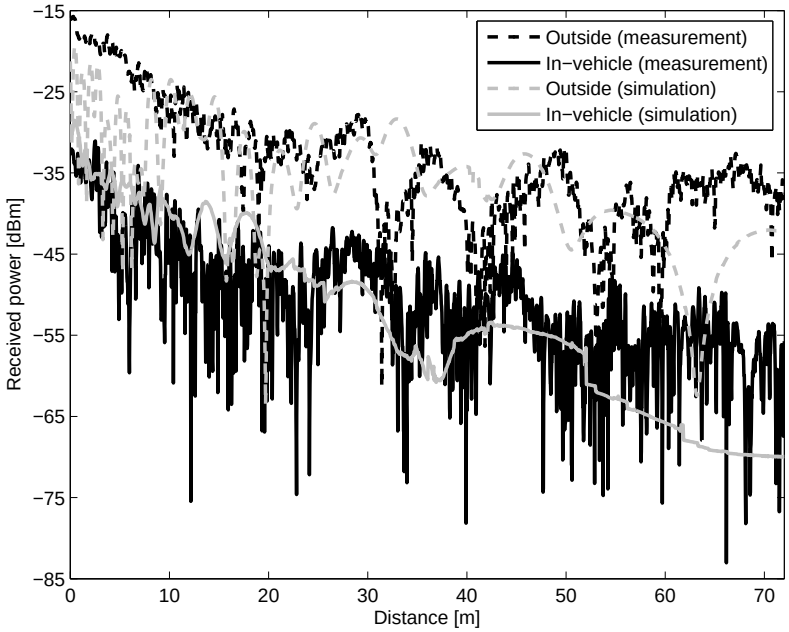

Figure 6.4: Measured and simulated received power outside and in-vehicle at 600 MHz along a track

Measured versus simulated fading characteristics: As can be seen in Fig. 6.4, true small-scale fading characteristics cannot be determined from the ray-tracing simulations. For the measurements, Fig. 6.4 shows (large) variations of the outside and in-vehicle received power level over short distance intervals with length half a wavelength to a wavelength. These small-scale variations are caused by random multipath and scattering. These specific propagation effects can not be modeled in the ray-tracing software. Therefore, Fig. 6.4 shows a much smoother change of simulated received power with distance in comparison with measurements. Also, Fig. 6.4 shows fairly good agreement between simulation and measurement. Deviations between simulation and measurement can be attributed to the inevitable simplification of the true propagation environment in the ray-tracing simulation. In the true measurement environment, additional physical structures not included in the ray-tracing model will affect propagation. Such physical structures can be for example nearby passing traffic and windows in building walls.

Importance of the LOS path: From the severe fading present in the outside power in Fig. 6.4, it can be concluded that the LOS path between the Tx and $\mathrm{Rx}_{\mathrm{out}}$ does not provide the largest contribution to the received power level. Ground and building reflections certainly have an effect on received power, which is a conse-

quence of our choice to perform measurements in a true multipath environment. To quantify the importance of ground and buildings reflections, we analyzed the ray-tracing simulations. For the outer antenna, we looked at the received power P_{LOS} [dBm] in the LOS component and the received power P_{refl} [dBm] of all ray paths combined without inclusion of the LOS path (i.e., only the ray paths which reflect off the ground and the surrounding buildings). For each center frequency, we calculated samples $A = P_{\mathrm{LOS}} - P_{\mathrm{refl}}$ [dB] along the receiver path of the outer antenna, for both cases where the Tx illuminates the front or the rear of the mini-van. It was found that, regardless of center frequency, the average difference A along the receiver path was approximately -10 dB. This means the power in the LOS path is on average 10 dB lower in comparison with the power in the reflected paths. This confirms that the LOS path is indeed not dominant, and that the ground and building reflections will contribute significantly to the power at the receiver.

6.3.1.2 Mean and standard deviation of VPL samples

Table 6.1 shows the mean value μ_{VPL} [dB] and standard deviation σ_{VPL} [dB] of the *measured* VPL samples calculated with formula (6.1). Distinction has been made between illumination of the rear and the front of the vehicle, and between vertical and horizontal orientation of $\mathrm{Rx_{in}}$. Additionally, for each center frequency separately, the mean μ_{VPL} and the standard deviation σ_{VPL} of all measured VPL samples for both illuminated vehicle sides and both in-vehicle antenna orientations were calculated. These results are listed in Table 6.1 under the "All" column. Similar to Table 6.1, Table 6.2 shows values μ_{sim} [dB] of the mean and σ_{sim} [dB] of the standard deviation of the *simulated* VPL samples.

Measurements versus simulations: When comparing Table 6.1 to Table 6.2, good agreement between measurements and simulations is observed in most cases. Measured μ_{VPL} (σ_{VPL}) and simulated μ_{sim} (σ_{sim}) values deviate on average only 1.5 dB (1.2 dB). Persons and objects within the vehicle, and objects such as parked cars in the suburban environment cause these (small) deviations between measurements and simulations. For the rear-illumination case, only the μ_{sim} values for horizontal in-vehicle antenna orientation at 900 and 2400 MHz are notably higher compared to experiments. This could be due to the measurement equipment in the van's cargo space. However, we note that VPL results for the front-illumination case would be more general useful, due to the constructional resemblance of a mini-van's front with a common passenger car front.

Dependence on in-vehicle antenna orientation, illuminated vehicle side, and frequency: Mean measured VPL values vary from 3.2 to 16.8 dB when $\mathrm{Rx_{in}}$

Frequency MHz	Tx illuminates the rear				Tx illuminates the front				All	
	Vertical $\mathrm{Rx_{in}}$		Horizontal $\mathrm{Rx_{in}}$		Vertical $\mathrm{Rx_{in}}$		Horizontal $\mathrm{Rx_{in}}$			
	μ_{VPL} [dB]	σ_{VPL} [dB]	μ_{VPL} [dB]	σ_{VPL} [dB]	μ_{VPL} [dB]	σ_{VPL} [dB]	μ_{VPL} [dB]	σ_{VPL} [dB]	μ_{VPL} [dB]	σ_{VPL} [dB]
600	16.80	3.24	23.75	3.92	4.89	4.68	13.26	4.06	14.68	7.89
900	7.54	3.00	16.03	3.16	3.20	3.28	17.56	4.17	12.40	6.40
1800	9.48	3.40	11.99	4.22	3.81	4.37	9.47	4.52	8.69	5.11
2400	13.79	4.09	19.86	4.21	5.25	4.06	15.88	4.24	13.68	6.76

Table 6.1: Measured VPL at 600, 900, 1800, and 2400 MHz for Tx illuminating the rear and front, and for vertical and horizontal in-vehicle antenna orientation

Frequency MHz	Tx illuminates the rear				Tx illuminates the front				All	
	Vertical $\mathrm{Rx_{in}}$		Horizontal $\mathrm{Rx_{in}}$		Vertical $\mathrm{Rx_{in}}$		Horizontal $\mathrm{Rx_{in}}$			
	μ_{sim} [dB]	σ_{sim} [dB]	μ_{sim} [dB]	σ_{sim} [dB]	μ_{sim} [dB]	σ_{sim} [dB]	μ_{sim} [dB]	σ_{sim} [dB]	μ_{sim} [dB]	σ_{sim} [dB]
600	15.44	5.86	22.54	3.73	3.16	3.09	12.89	3.88	13.90	8.27
900	8.17	5.82	23.14	5.59	4.35	4.75	18.45	4.07	13.53	9.12
1800	8.63	4.94	11.57	2.33	3.65	4.87	9.11	3.40	6.59	5.43
2400	12.44	4.34	25.30	4.00	5.51	4.60	12.94	3.11	14.25	8.55

Table 6.2: Simulated VPL at 600, 900, 1800, and 2400 MHz for Tx illuminating the rear and front, and for vertical and horizontal in-vehicle antenna orientation

is positioned vertically and from 9.5 to 23.8 dB when $\mathrm{Rx_{in}}$ is positioned horizontally. Tables 6.1 and 6.2 show consistently higher VPL values for horizontal orientation in comparison with vertical orientation for both measurements and simulations. Because during our measurements LOS between the Tx and the mini-van was maintained at all times, and because of the vertical polarization of the Tx, the composed wave at $\mathrm{Rx_{in}}$ will not deviate significantly from vertical polarization. In other words, signal depolarization is expected to be limited due to the LOS circumstances (even though the LOS path itself is not dominant as shown in Section 6.3.1.1). This explains why vertical reception at $\mathrm{Rx_{in}}$ is favored over horizontal reception. The difference in VPL between vertical and horizontal reception is higher for our measurements compared to [1], where NLOS measurements caused signal depolarization.

The mean VPL values in Table 6.1 are in general lower for illumination of the front than of the rear of the vehicle. This can be explained by considering the vehicle's construction. When the Tx illuminates the front of the vehicle, only the front window of the mini-van is in between the Tx and $\mathrm{Rx_{in}}$. In the case that the

Tx radiates to the rear of the mini-van, smaller rear windows and the rear loading space will obstruct the incident waves much more. Larger values of the VPL can therefore be expected in the latter case.

The mean VPL in Tables 6.1 and 6.2 show no monotonous linear decreasing dependence of the frequency. Previous work has shown that outdoor to indoor propagation is a fairly complex process: the entry loss through windows is not only determined by their dimensions, but also by the constitutive parameters of the glass and the materials surrounding the windows [6]. Because of this, the relationship between penetration loss and frequency rather follows a minimum-maximum pattern. In case of building penetration, this has been demonstrated in [6] through simulations of the penetration loss through a single window embedded in a brick wall. We have performed similar simulations of the penetration loss through a single window embedded in an infinite PEC plane, which is more applicable to the vehicle penetration case. These simulations also showed a minimum-maximum variation of the entry loss with frequency.

We note that the values in Table 6.1, excluding the 'All' column, should be interpreted as best-case and worst-case limits of the vehicle penetration loss. The actual penetration loss will be situated between these limits. The provided penetration loss values can be used by a wireless system designer to calculate a link budget for best-case (front-illumination, vertical reception) and worst-case (rear-illumination, horizontal reception) attenuations.

Influence of the averaging interval: As mentioned in Section 6.2.1.1, VPL samples were calculated by averaging received power levels over distances equal to 10 wavelengths. To investigate the effect of the averaging interval's length on the values of μ_{VPL} and σ_{VPL}, VPL samples were also determined by averaging over 5, 20, and 40 wavelength intervals. A maximum change in μ_{VPL} of only 0.8 dB was found when altering the averaging interval's length from 5 to 40 wavelengths. On average for all μ_{VPL} values reported in Table 6.1, a change in μ_{VPL} of merely 0.3 dB was found when changing the averaging interval. We therefore conclude that the mean μ_{VPL} does not change considerably with the choice of the averaging interval. For the σ_{VPL} parameter, a maximum change of 2.5 dB was found when adjusting the averaging interval. On average for all σ_{VPL} values in Table 6.1, σ_{VPL} changed 1.5 dB with the averaging interval's length. The dependence on the averaging interval's length of the σ_{VPL} parameter can not be considered negligible. Furthermore, it was found that σ_{VPL} is consistently lower for larger averaging intervals. This can be explained by the fact that shadow fade patterns are more smoothed out as the averaging interval is lengthened. To avoid this, we did not choose the length of the averaging interval too large, and chose a length of 10 wavelengths as proposed in [4].

6.3.2 Statistical properties of the VPL

In this section the statistical properties of the measured VPL samples calculated with formula (6.1) will be validated. The VPL tends to be lognormally distributed [1]. Table 6.1 shows 20 $(\mu_{\mathrm{VPL}}, \sigma_{\mathrm{VPL}})$ pairs. Each pair is associated with a specific VPL scenario, which is defined by its center frequency (600, 900, 1800, or 2400 MHz), illuminated vehicle side (rear, front, or both), and in-vehicle antenna orientation (vertical, horizontal, or both). Analogously, Table 6.2 shows $(\mu_{\mathrm{sim}}, \sigma_{\mathrm{sim}})$ pairs associated with the 20 VPL scenarios. For the statistical analysis we calculate the empirical Cumulative Distribution Function (CDF) of the measured and simulated VPL samples of each VPL scenario. Each empirical CDF is fitted to a lognormal distribution function using a least-squares fit. This results in estimates μ_{fit} [dB] of the mean value and σ_{fit} [dB] of the standard deviation of the fitted lognormal distribution function. The fitted estimates μ_{fit} and σ_{fit} are then compared to the mean values and standard deviations in Tables 6.1 and 6.2. It was found that μ_{fit} and σ_{fit} deviated less than 0.6 dB from the values in Tables 6.1 en 6.2. These low deviations for both mean value and standard deviation confirm that the measured and simulated VPL closely follow a lognormal distribution.

To further assess lognormality of the vehicle penetration loss, we also performed a statistical goodness-of-fit test on the VPL samples. A Kolmogorov-Smirnov (KS) test was conducted at significance level 5%, wherein the empirical CDF of each measured and simulated VPL scenario was compared to a lognormal CDF with corresponding mean and standard deviation from Table 6.1 or 6.2. For the measurements, this KS test passed for 19 out of 20 VPL scenarios listed in Table 6.1. For the simulation results in Table 6.2, the KS test passed for all 20 VPL scenarios. The high success rate of the KS test lead us to conclude that both measurements and simulations exhibit lognormal large-scale fading statistics.

Fig. 6.5 shows the empirical CDFs of VPL samples of two VPL scenarios at 2400 MHz, for both the measurements and the simulations. Fig. 6.5 exhibits good agreement between measured and simulated CDFs, showing that approximately the same dynamic range of VPL samples is obtained from the measurements and the simulations alike.

6.4 Comparison with previous measurements

In this section, a comparison of our penetration loss results with previous measurements from [1–3] will be made. We will first shortly describe the measurement procedures followed in [1–3], and point out similarities and differences in comparison with our measurement methodology. In [1], vehicle attenuation characteristics at 800 MHz were determined with an experimental setup that is highly similar to our setup. The key difference regarding the measurement procedure is that the

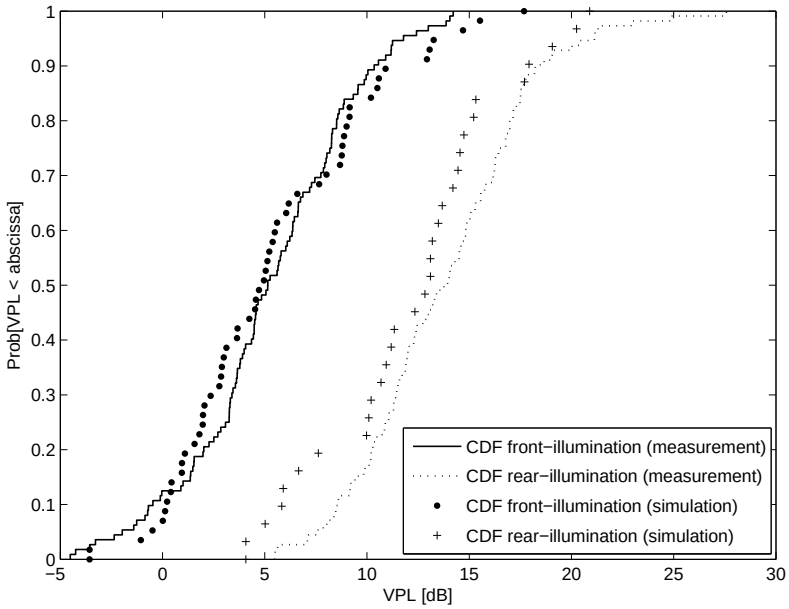

Figure 6.5: CDFs of measured and simulated penetration loss samples for vertical in-vehicle antenna orientation at 2400 MHz

drives in [1] included larger suburban areas where NLOS was encountered. These NLOS circumstances caused signal depolarization, resulting in highly reduced differences between vertical and horizontal reception compared to our measurements. In [2], directional vehicle attenuation characteristics were determined at center frequencies of 150, 450, 800, and 900 MHz on an antenna pattern range. The in-vehicle received power level was measured by rotating the vehicle in LOS with the Tx in an open, outside location. The outside received power level was measured with a person holding the mobile antenna while rotating in an anechoic chamber. In [3], measurements of the vehicle penetration loss for a satellite communication link at 1600 MHz were performed. For a satellite communication link, propagation paths are mostly vertical: vehicle-to-transmitter elevation angles between 8° and 90° were investigated. For our measurements however, vehicle penetration losses were determined specifically for terrestrial communication links with mostly horizontal propagation paths, which differs from the setup in [3]. Because of this, a comparison of our penetration loss results with [3] could not be made.

Reported values of the vehicle penetration loss in [1] and [2] do not include the direction of impinging waves or have a strong dependence on in-vehicle antenna orientation. We will therefore make a comparison with only the results in the 'All' column of Table 6.1. For a mini-van in a suburban environment, a mean vehicle penetration loss of approximately 9 dB with a standard deviation of about

3 dB is reported at 800 MHz in [1]. In [2], median vehicle losses between 3 dB and 10 dB are reported at 900 MHz, depending on whether the mobile antenna is placed at the head level or at the belt level. At 900 MHz, Table 6.1 shows a comparable but somewhat higher mean vehicle loss of approximately 12 dB. The standard deviation of 6 dB at 900 MHz in Table 6.1 is also higher compared to that of 3 dB in [1]. This is thought to be because of the inclusion of polarization mismatch in our measurement data, with a best-case and worst-case in-vehicle antenna orientation. The presence of these two extreme cases increases the spread of the VPL samples. A comparison of vehicle penetration loss results at 600, 1800, and 2400 MHz in Table 6.1 with references [1] and [2] could not be made because of the non-negligible differences in measured center frequencies.

6.5 Conclusions

In this chapter, measurements and simulations of the vehicle penetration loss at 600, 900, 1800, and 2400 MHz have been presented. The mean measured vehicle penetration loss varies from 3.2 to 23.8 dB, depending on frequency, illuminated vehicle side, and in-vehicle antenna orientation. Overall good agreement between measured and simulated VPL has been found. Vehicle penetration losses follow a lognormal distribution closely, with measured standard deviations ranging between 3.0 and 4.7 dB, depending on frequency, illuminated vehicle side, and in-vehicle antenna orientation. Reported penetration loss values at 900 MHz were compared to previous measurements from the literature. The vehicle penetration loss at 900 MHz was found to be somewhat higher for our measurements, but still comparable to values previously reported.

References

[1] I. Kostanic, C. Hall, and J. McCarthy. *Measurements of the vehicle penetration loss characteristics at 800 MHz*. In 48th IEEE Vehicular Technology Conference Proceedings, pages 1–4, Ottawa, CA, May 1998.

[2] C. Hill and T. Kneisel. *Portable radio antenna performance in the 150, 450, 800 and 900 MHz bands outside and in-vehicle*. IEEE Transactions on Vehicular Technology, 40(4):750–756, November 1991.

[3] W. J. Vogel, G. W. Torrence, and N. Kleiner. *Measurement of Propagation Loss into Cars on Satellite Paths at L-band*. In 2nd European Workshop on Mobile/Personal Satcoms Proceedings, pages 129–138, Rome, IT, October 1996.

[4] D. J. Cichon, and T. Kürner. *Propagation prediction models*. In COST 231 Final Report. COST Telecom Secretariat, Brussels, BE, 1999.

[5] F. Harrysson. *A simple directional path loss model for a terminal inside a car*. In 58th IEEE Vehicular Technology Conference Proceedings, pages 119–122, Orlando, FL, USA, October 2003.

[6] S. Stavrou and S. Saunders. *Factors influencing outdoor to indoor radio wave propagation*. In Twelfth International Conference on Antennas and Propagation (Conf. Publ. No. 491), pages 581–585, London, UK, March 2003.

7 Conclusions and future research

This chapter summarizes the conclusions obtained in the research chapters 2 to 6. Part of this chapter is also dedicated to an exposition of future research in the propagation topics presented in this work. These areas of future research encompass the characterization of additional multipath component parameters in industrial environments, the environment considered the most in this thesis.

7.1 Conclusions

Aspects of propagation were investigated for three types of indoor environments, namely industrial, office, and vehicular environments.

7.1.1 Industrial environments

In this work, measurements in factories were performed to reflect a specific kind of industrial communication, namely communication between an access point located at a considerable height of about 6 m and wireless terminals situated at smaller heights of about 2 m. This kind of communication has various important applications, such as access points which communicate with a large number of wireless sensor nodes in a production line to monitor and adjust parameters of the industrial processes, and access points which provide terminals on fork-lift trucks with information about the current stock in the warehouse.

Firstly in chapter 2, measurements of **large-scale fading** and **temporal fad-**

ing in industrial environments have been presented. Small-band measurements were performed at 900, 2400, and 5200 MHz. An effort was made to categorize measurement data into different industrial topographies. These topographies were defined to further subdivide the industrial environment into different surroundings for which significantly different large-scale and temporal fading behavior was expected.

Large-scale fading was found to be excellently described by a one-slope path loss model and to agree well with lognormal fading statistics. It was found that median path loss is most accurately expressed by a one-slope model with non-fixed intercept path loss, which was attributed to the choice of a transmitting antenna installed approximately at rooftop level. A physical model explaining the dependency on topography and frequency of the one-slope model's parameters was presented. Herein, a key finding was that the path loss exponent appears to decrease with increasing frequency. Measurements were performed in wood processing and metal processing facilities. Path loss variations between these two types of facilities were however found to be limited, mainly because of their similar constructional details: industrial inventory in all facilities consisted for the largest part of similar metal machinery. Overall, path loss was observed to be somewhat larger compared to industrial measurements reported in literature, which was attributed to the height difference between the transmitter and the receiver used in our measurements but not in literature.

Temporal fading was found to correspond excellently to Ricean statistical distributions. A physical model explaining the values of the Ricean K-factors across different temporal fading topographies was given. Temporal fading was found to be most significant in manual production lines and to be overall less important than in office environments. Temporal fading was found to be only weakly dependent on frequency. Measured Ricean K-factors are found to follow a lognormal distribution with mean 12.3 dB and standard deviation 5.4 dB.

Following in chapter 3, a **validation of the large-scale and temporal fading models** by a number of site survey measurements has been presented for an IEEE 802.11b/g wireless system. More specifically, it was investigated if the wireless range according to the industrial propagation models matches the range extracted from site survey measurements. The comparison between propagation models and site survey was made for three practically important 802.11b/g data rates of 2, 11, and 18 Mbps. Generally good statistical agreement was established between the theoretical range according to the propagation models and the empirical range according to the site survey measurements. However, the empirical range in production centers at lower data rates (2 and 11 Mbps) can at certain occasions be substantially lower than the calculated theoretical range. These statistical deviations can be explained from the physical layout of the environment: the lower

empirical range in some production centers can be attributed to severe signal attenuation by large obstacles, which are present in some production halls. These large obstacles consist of densely packed storage racks and gantries which have heights often exceeding that of the access point. It is therefore advised to install additional access point in areas shadowed by these obstacles, as these are often impenetrable to the 802.11b/g signal. Furthermore, to maximize the range of an industrial access point, it is recommended to keep the access point clear of these large obstacles as well as walls. Additionally, a result was that there appears to be very limited differences in empirical site survey ranges between receiving antenna heights of 0.5, 1.5, and 2 m.

Lastly in chapter 4, measurements of the **power delay profile** have been presented. These measurements were performed through frequency-domain channel sounding (from 800 MHz to 4 GHz) and by using the virtual antenna array method. Stationarity of the wireless channel during measurements, which is required for this type of channel sounding, was validated through a statistical correlation analysis. The power delay profiles, averaged over a small-scale fading area, were found to clearly exhibit clustering of received power as function of delay. Because of this, the well-known Saleh-Valenzuela model for the averaged power delay profile was fitted to the measurement data. For our delay resolution of 0.31 ns, a significant amount of multipath energy was present in each delay bin. The Saleh-Valenzuela model was therefore interpreted as a classical tapped delay line model with taps arriving at regular time intervals of 0.31 ns. For the parameters of the Saleh-Valenzuela model, results are summarized as follows:

- The ray power decay constant was found to be dependent on the delay of the corresponding cluster. A linear model between the logarithm of the ray power decay constant and the delay was proposed.
- The cluster power decay constant was determined at 21.87 ns. A model for the cluster peak power as a function of delay was presented.
- Cluster interarrival times were determined to be exponentially distributed with mean equal to 18.40 ns.
- Small-scale amplitude fading was found to be Rayleigh distributed for all delay bins except the first one. For the first delay bin, Nakagami-m fading provided a better fit.

Generally, the difference between line of sight and obstructed line of sight had only limited effect on the parameters of the Saleh-Valenzuela model. The parameter's values were in the same range of those in literature of other measurements of the industrial power delay profile, despite the different antenna heights used in this study. Additionally, the root mean square delay spread was investigated and found to range between 41.37 ns and 48.51 ns for line of sight scenarios and between 43.90 ns to 53.70 ns for obstructed line of sight scenarios.

7.1.2 Office environment

For measurements in office environments, parameters associated with discrete propagation paths were extracted using the ESPRIT algorithm. The estimated path parameters included **azimuth of arrival, azimuth of departure, delay, and power**. In agreement with the geometry-based stochastic type of channel models, the path parameters were grouped into clusters using the statistical K-power-means algorithm. Statistical distributions of the propagation parameters within individual clusters were determined, and correlations between these parameters were assessed. Motivated choices for the statistical distributions were made, based on the propagation physics expected in office environments. The distributional location and scale parameters were subsequently used to characterize the intra-cluster and inter-cluster dynamics of the multipath component parameters. This was done by in turn determining the statistical distributions of these location and scale parameters, and by considering their correlations. To validate the distributional choices, the goodness-of-fit to the proposed distributions was verified using a number of statistical hypothesis tests with sufficient power. The most important results of the statistical analysis are summarized in Table 5.2. Additionally, a new notation for the Multiple Input Multiple Output (MIMO) channel matrix was given which more visibly shows the clustered nature of propagation paths, i.e., FActorization into a BLock-diagonal Expression (FABLE).

7.1.3 Vehicular environment

Measurements and simulations of the **vehicle penetration loss** at 600, 900, 1800, and 2400 MHz have been presented. The mean measured vehicle penetration loss varies from 3.2 to 23.8 dB, depending on frequency, illuminated vehicle side, and in-vehicle antenna orientation. Overall good agreement between measured and simulated vehicle penetration loss has been found. Vehicle penetration losses follow a lognormal distribution closely, with measured standard deviations ranging between 3.0 and 4.7 dB, depending on frequency, illuminated vehicle side, and in-vehicle antenna orientation. Reported penetration loss values at 900 MHz were compared to previous measurements from literature. The vehicle penetration loss at 900 MHz was found to be somewhat higher for our measurements, but still comparable to values previously reported.

7.2 Future research

This section assembles a few thoughts on possible future research directions for the indoor industrial case. These are research topics that are deemed worthwhile to investigate in the author's own personal opinion, but could not be further digged into in the limited time span of the doctorate.

The last few years, research in MultiPath Component (MPC) estimation algorithms has started to move away from the paradigm of seeing the wireless channel solely as a collection of discrete specular MPCs. The idea of specular MPCs is taken from optical ray theory, and is only valid if the interacting objects are smooth and have dimensions much larger than the communication wavelength. For regular indoor environments, these requirements are usually satisfied for optical communications with wavelengths in the order of nanometer, but they are not readily satisfied for RF communications with wavelengths in the order of centimeter. In case the interacting objects are not smooth and electrically large, interactions will not result in specular paths with well-defined, discrete directions in space. Interactions will rather result in scattered or diffuse paths that are distributed over a certain range of directions. These scattered paths are also referred to as Diffuse Multipath Components (DMC). The recent paradigm shift in MPC parameter estimation is that the wireless channel is now seen as a collection of specular MPCs plus DMC which follow certain continuous power density distributions in the angular and delay domains [1, 2].

Measurements in office environments have already shown that the power of DMC can be a very considerable fraction of the total wireless power in the channel, e.g., 50 to 90% in [3]. In the author's opinion, a **characterization of DMC in industrial environments** could lead to some interesting results. As mentioned in Section 2.4.1.2 of Chapter 2, industrial inventory is usually made up of small, irregularly shaped machine parts. This type of inventory is expected to give rise to DMC rather than to specular MPCs. The generation of DMC will be even further stimulated by the fact that the small machine parts have highly reflective metallic surfaces. For this reason, I hypothesize that the fraction of the total wireless power found in DMC could be even greater in industrial environments than in office environments. It would be interesting to investigate this hypothesis and its implications on the achievable diversity order in MIMO industrial channels.

For industrial environments, the choice was made in this thesis to investigate propagation for a scenario where an access point near rooftop level (at about 6 m height) communicates with a wireless terminal near ground level (at about 2 m height). Because of this height difference, propagation paths can not considered to be horizontal but are instead sloped. An investigation in the **statistics of the angular azimuth and elevation MPC parameters in industrial environments** could therefore be worthwhile. The distribution of MPC power over the azimuthal and elevational angles is determinative for the correlations between the complex signals transmitted or received by different antennas in a multiple antenna array. These correlations in turn determine the order of diversity of the channel. In office environments, the elevational spread of MPC power is often neglected because of-

fice dimensions in elevation (i.e., ceiling heights) are usually small compared to office dimensions in azimuth (i.e., floor lengths and widths). In the measured industrial environments however, ceiling heights were around 7 to 8 m, leading us to suspect that the elevational properties of MPCs do matter in these environments. In office environments, diversity is commonly sought only in azimuth, i.e., antennas in an antenna array are spatially dislocated in a horizontal plane. In industrial environments, there is thus the opportunity to also seek diversity in elevation, if measurements of the elevational MPC parameters prove this is viable.

We conclude this section on future research with a short elaboration on the possible **use of the FABLE notation in MPC estimation algorithms**. From a computational point of view, the extraction of MPC parameters is often a daunting task. Each MPC parameter is seen as a dimension of the multidimensional channel, and extracting its properties becomes increasingly difficult as the number of dimensions grows (this phenomenon is also known as the *"curse of dimensionality"* in mathematics). To tackle this, the majority of MPC estimation algorithms break the multidimensional search problem down into iterations of one-dimensional searches, which are usually quite easy to perform. This is for example the strategy followed by the SAGE MPC estimation algorithm [4].

More recently, MPC estimation algorithms have again increased in complexity since the concept of DMC was introduced. In estimation algorithms that include DMC (e.g., RiMAX [1]), this complexity is alleviated by alternatively searching for and optimizing the specular MPCs and DMC separately. It is in this estimation process that we see a possible application for the FABLE notation, which as explained in Chapter 5, separates the specular MPCs into inter-cluster and intra-cluster parts. In cases where MPC clusters can be assumed, the FABLE notation could reduce the computational complexity of estimation algorithms by iteratively optimizing the specular paths' inter-cluster part, the specular paths' intra-cluster part, and the DMC. This is in contrast to going back and forth between optimizing the specular paths and the DMC as it happens now in for example RiMAX.

For this approach to succeed, it is first necessary to create a mathematical framework for the inclusion of the FABLE notation in estimation algorithms such as RiMAX. Next, the estimation accuracy of the adapted algorithm must be assessed, as much as possible through theoretical calculations but mainly through simulations.

References

[1] A. Richter. *Estimation of Radio Channel Parameters: Models and Algorithms*. PhD thesis, Technische Universität Ilmenau, Fakultät für Elektrotechnik und Informationstechnik, Ilmenau, DE, 2005.

[2] C. B. Ribeiro, A. Richter, and V. Koivunen. *Joint Angular- and Delay-Domain MIMO Propagation Parameter Estimation Using Approximate ML Method*. IEEE Transactions on Signal Processing, 55(10):4775–4790, October 2007.

[3] J. Salmi, J. Poutanen, K. Haneda, A. Richter, V.-M. Kolmonen, P. Vainikainen, and A. F. Molisch. *Incorporating Diffuse Scattering in Geometry-based Stochastic MIMO Channel Models*. In 4th European Conference on Antennas and Propagation, Barcelona, ES, April 2010.

[4] B. H. Fleury, M. Tschudin, R. Heddergott, D. Dahlhaus, and K. I. Pedersen. *Channel Parameter Estimation in Mobile Radio Environments Using the SAGE Algorithm*. IEEE Journal on Selected Areas in Communications, 17(3):434–450, March 1999.